A Multiscale-Multiphysics Framework for Modeling Organ-scale Liver Regrowth

A THESIS
SUBMITTED TO THE DEPARTMENT OF CIVIL AND ENVIRONMENTAL ENGINEERING
OF THE TECHNICAL UNIVERSITY OF DARMSTADT
BY

Adnan Ebrahem

IN FULFILLMENT OF THE REQUIREMENTS
FOR THE DEGREE OF
DOKTOR-INGENIEUR (DR.-ING.)

First referee: Prof. Dr.-Ing. Dominik Schillinger

Second referee: Prof. Dr.-Ing. Silvia Budday

TECHNISCHE
UNIVERSITÄT
DARMSTADT

Darmstadt, 2024

Adnan Ebrahem
A Multiscale-Multiphysics Framework for Modeling Organ-scale Liver Regrowth

First referee: Prof. Dr.-Ing. Dominik Schillinger
Second referee: Prof. Dr.-Ing. Silvia Budday

Darmstadt, Technical University of Darmstadt
Published year on TUprints: 2024
Date of thesis defense: December 11, 2024

URN: urn:nbn:de:tuda-tuprints-289153
URI: https://tuprints.ulb.tu-darmstadt.de/id/eprint/28915

A Multiscale-Multiphysics Framework for Modeling Organ-scale Liver Regrowth

Accepted doctoral thesis by Adnan Ebrahem

In fulfillment of the requirements for the degree of Doktor-Ingenieur (Dr.-Ing.)

Date of submission: October 09, 2024

Date of thesis defense: December 11, 2024

Primary advisor: Prof. Dr.-Ing. Dominik Schillinger

Committee members:

Prof. Dr.-Ing. Dominik Schillinger	Technical University of Darmstadt
Prof. Dr.-Ing. Silvia Budday	University of Erlangen-Nuremberg
Prof. Dr.-Ing. Andreas Eichhorn	Technical University of Darmstadt
Prof. Dr. rer. nat. Holger Lutze	Technical University of Darmstadt
Prof. Dr.-Ing. Hauke Zachert	Technical University of Darmstadt

Acknowledgements

This thesis was conducted during my time at the Institute of Mechanics and Computational Mechanics, Leibniz University Hanover, and at the Institute for Mechanics, Technical University of Darmstadt, throughout my PhD studies between 2019 and 2024. These years have been a period of significant growth in my scientific development, allowing me to acquire extensive knowledge in the development of numerical methods, particularly in the field of solid mechanics. The success of this thesis was made possible by the support and contributions of many individuals, to whom I owe my sincere gratitude.

First and foremost, I would like to express my deepest thanks to my supervisor and mentor, **Professor Dominik Schillinger**. His unwavering support, invaluable guidance, and constant encouragement have been fundamental to the completion of this work. His expertise and insight have greatly shaped my research, and for that, I am truly grateful.

My special thanks are also directed to **Professor Silvia Budday** from the Institute of Continuum Mechanics and Biomechanics at the University of Erlangen-Nuremberg for serving as the co-chair of my promotion committee. I would also like to thank **Professor Andreas Eichhorn**, head of the examination board, and **Professor Holger Lutze and Professor Hauke Zachert**, members of the examination board.

I would also like to extend my heartfelt appreciation to my colleagues and friends from Hannover and Darmstadt for their collaboration and contributions. Special thanks go to **Etienne Jessen, Jannes Hohl, Marco ten Eikelder, Michal Mika and Tarun Gangwar** for their scientific collaboration, insightful discussions, and shared expertise, which have greatly enriched my research experience.

I am equally thankful to **Thi Hoa Nguyen, Vahid Badhrkhani, Jonathan Stollberg, Stein Stoter, and René Hiemstra**, as well as the aforementioned colleagues, for the warmth and camaraderie beyond the academic setting. The coffee breaks, enjoyable dinners, and memorable trips we shared have made this journey all the more rewarding and unforgettable.

Finally, I dedicate this work to **my family**. My heartfelt thanks go to **my parents** for their unwavering support, limitless patience, and constant encouragement. They have been a source of strength throughout this journey, always standing by my side.

To all of you, thank you for your incredible support, making this journey both unforgettable and deeply fulfilling.

Adnan Ebrahem
Darmstadt, September, 2024

Abstract

The human liver is capable of regenerating after partial surgical resection. While driven by rapid cell division at the microscale, tissue growth associated with liver regeneration significantly affects the liver's meso- and macroscale perfusion capability, which liver functionality critically depends on. In this thesis, a computational framework is presented that integrates three models associated with physics at multiple spatial scales to simulate the effect of liver tissue regrowth on the perfusion capability of a full-scale liver. This includes (1) a discrete vascular tree approach representing blood supply and drainage at the organ scale, (2) a multi-compartment homogenized flow model representing perfusion at the lower levels of the hierarchical tree network and the liver lobules, and (3) an isotropic growth model of a poroelastic medium representing hyperplasia of liver lobules. Appropriate coupling mechanisms are provided and discussed to ensure physiological interaction between these components. Additionally, an empirical driving force is motivated, initiating compensatory growth of liver tissue until a physiological blood flow rate is achieved at each point of the liver domain. This driving force is calibrated based on available liver data. Using a patient-specific liver geometry, it is demonstrated that the multiscale-multiphysics model correctly predicts the typical perfusion outcome associated with common surgical cut patterns.

Zusammenfassung

Die menschliche Leber besitzt die Fähigkeit, sich nach einer chirurgischen Resektion zu regenerieren. Während dieses Wachstum auf mikroskopischer Ebene durch schnelle Zellteilung angetrieben wird, beeinflusst es auf meso- und makroskopischer Ebene die Perfusionsfähigkeit der Leber, von der ihre Funktionalität maßgeblich abhängt. In dieser Arbeit wird ein Berechnungsmodell vorgestellt, das drei Modelle aus unterschiedlichen physikalischen Skalen integriert, um den Einfluss des Lebergewebewachstums auf die Perfusionsfähigkeit einer vollständig skalierbaren Leber zu simulieren. Diese Modelle umfassen (1) einen diskreten Gefäßbaumansatz, der die Blutversorgung und -drainage auf Organebene darstellt, (2) ein homogenisiertes Multikompartment-Flussmodell, das die Perfusion auf den unteren Ebenen des hierarchischen Gefäßnetzes und der Leberläppchen repräsentiert, sowie (3) ein isotropes Wachstumsmodell eines poroelastischen Mediums, das die Hyperplasie der Leberläppchen beschreibt. Geeignete Kopplungsmechanismen werden bereitgestellt und diskutiert, um eine physiologische Interaktion zwischen diesen Komponenten zu gewährleisten. Darüber hinaus wird ein empirischer Wachstumsmechanismus motiviert, der das kompensatorische Wachstum des Lebergewebes initiiert, bis an jedem Punkt des Leberbereichs eine physiologische Blutflussrate erreicht wird. Dieser Wachstumsmechanismus wird anhand verfügbarer Leberdaten kalibriert. Anhand einer patientenspezifischen Lebergeometrie wird gezeigt, dass das Multiskalen-Multiphysik-Modell das typische mit gängigen chirurgischen Resektionsschnitten verbundene Perfusionsergebnis korrekt vorhersagt.

Contents

1 Introduction

1.1 Motivation

Liver cancer poses a significant global health challenge and is the seventh most commonly diagnosed cancer and the third leading cause of cancer mortality worldwide [1]. The burden of this disease and the incidence of liver cancer is increasing in aging societies, leading to an increasing demand for partial liver resection, or partial hepatectomy (PHx), a surgical procedure that involves the removal of diseased portions of the liver [2]. The liver's unique ability to regenerate, capable of restoring up to 70 % of its original mass, allows for such procedures to be performed without complete loss of liver function. However, the success of liver regeneration, and consequently the functionality of the remaining liver tissue, depends on a multitude of critical factors. This includes the remaining liver volume, the adequacy of blood supply and drainage, and the impairment of the micro- and macrocirculation due to the individual cut pattern [3].

The process of liver regeneration is intricately linked to the organ's vascular architecture. The liver is highly vascularized, with a complex network of blood vessels that serve vital physiological functions. The effectiveness of liver regeneration and thus, the long-term success of the surgical intervention depends on the ability of the remaining liver tissue to maintain sufficient blood perfusion. However, the growth of new tissue during regeneration can significantly alter perfusion dynamics, potentially compromising liver function [4]. Therefore, the patient-specific assessment of the postoperative success of partial liver resection prior to the operation remains a challenge for surgeons [4].

Computational models can help predict the impact on blood perfusion and determine the amount of liver tissue that can be removed safely while functionality is maintained. However, patient-specific modeling of surgical liver resection requires adequate modeling of the liver's hierarchical vasculature. Additionally, modeling of liver growth is strongly linked to modeling perfusion, and therefore requires an appropriate patient-specific representation of the hierarchical liver vasculature. While medical imaging technologies have advanced considerably, they still fall short of capturing the full complexity of the liver's vasculature, particularly at smaller scales. Given the limited resolution of in-vivo imaging, reconstruction from imaging data is generally only possible for the few largest vessels in the hierarchy. Consequently, it becomes necessary to generate these vascular structures synthetically using computer-based methods built on energy minimization principles [5]–[9].

While there are methods to create realistic vascular networks, which are largely based on optimization principles, these synthetic trees are often limited in their ability to interface directly with models of tissue mechanics and deformation. Blood perfusion within the liver is closely linked to the mechanical properties of the tissue, including

its ability to deform under physiological conditions. To enhance the predictive capabilities of computational liver models, it is essential to incorporate both vascular structure and tissue mechanics. This requires a coupling of discrete vascular tree models with continuum-based approaches. One solution is to resort to homogenization and the theory of poromechanics, replacing the complex heterogeneous medium by a fictitious homogeneous medium with equivalent macroscale behavior. In this work, it is demonstrated that the two modeling approaches, i.e., discrete synthetic vascular trees and continuum poroelasticity, can be synergistically combined to better visualize changes in perfusion at the organ scale, for example, due to partial resections.

Despite advances in these areas, the interplay between liver regrowth and perfusion, particularly at multiple scales, remains inadequately addressed in current models. This thesis aims to address this gap by developing a multiscale-multiphysics framework that integrates vascular tree generation, liver perfusion modeling, and simulation of liver tissue growth. By integrating these components, the proposed framework is intended to provide a more accurate and comprehensive analysis for predicting the outcomes of liver resection surgery, ultimately supporting surgeons in planning.

As the field of computational biomechanics advances, there is an increasing importance of developing models that can seamlessly integrate different scales of biological processes, ranging from the cellular levels to the tissue and organ scales. The liver's remarkable ability to regenerate, combined with its intricate vascular architecture, makes it a particularly challenging candidate for such multiscale modeling. Conventional models that target only one scale or specific aspect of liver physiology often fail to capture the full complexity of the organ's behavior, especially when it undergoes surgical procedures like liver resections. A multiscale-multiphysics approach, as presented in this thesis, is crucial to understanding the interplay between tissue regeneration, blood perfusion, and mechanical forces in the liver, thereby offering a more comprehensive analysis of postoperative liver function.

Moreover, accurately modeling liver regeneration and perfusion has crucial clinical significance. Liver surgeries, especially resections, pose a risk of postoperative liver failure, frequently due to insufficient tissue regeneration or impaired blood supply in the remaining liver tissue. A comprehensive whole-organ model, that connects liver regrowth and the associated change in perfusion capability across the relevant scales is still lacking. The development of a model that integrates vascular tree generation, tissue growth simulation, and perfusion analysis aims to offer surgeons critical insights for both preoperative planning and postoperative care. This framework could help in the identification of the most effective resection strategy for each patient, thereby reducing the risk of complications and enhancing overall surgical outcome. Ultimately, this study aims to integrate computational modeling with clinical practice.

1.2 Previous work in the field

1.2.1 Macroscopic scale

One commonly employed approach to generate hierarchical vascular trees is constrained constructive optimization (CCO), which builds on Murray's law [10] to optimize the relationship between vessel radii and flow [5], [6]. The CCO method constructs vascular trees by progressively adding segments and adjusting their geometry locally to enhance blood flow efficiency. Building on the CCO method, organ-specific vascular systems have been generated for various organs, including the liver [7], [11], heart [12], stomach and brain [13].

More advanced models, such as those developed by Jessen et al. [14]–[16], reformulate the generation of vascular trees as a nonlinear optimization problem, enabling the generation of an optimal global tree geometry. This approach allows for more flexibility in adjusting boundary conditions and constraints and generates trees that are optimal both in topology and geometry. Additionally, this approach produces synthetic trees that more closely match physiological data compared to traditional CCO methods [14].

Several models have been developed to simulate liver perfusion. Some models describe perfusion in the whole organ, either based on synthetically generated vascular trees [17] or experimentally determined trees [18], [19]. Other models have been developed to account for the vascular features across multiple spatial scales by partitioning the vasculature into spatially coexisting compartments and homogenizing them using Darcy's law [20]. This is also known as the multi-compartment Darcy approach, which models perfusion as a Darcy porous-media flow, using effective permeability obtained from anatomical vascular structures. Each compartment captures specific spatial scales and interactions between compartments are modeled through distributed sources and sinks that account for mass exchange. This model has been successfully applied to simulate perfusion in various organs, including the heart [21], [22] and the liver [17].

Various models based on continuum mechanics have been proposed to model the growth of biological tissues [23]–[31], including heart [32]–[34], brain [35], [36], tumor tissue [37], arterial wall growth [38], [39], cardiovascular modeling [40] or vein graft growth [41]. A major focus lies on specifying individual growth laws and identifying factors that drive growth for each specific application. These models can simulate the volumetric growth of tissue stimulated by mechanical forces without the necessity of resolving the underlying processes at the cell level [3]. To the best of our knowledge, there is currently no continuum mechanics model that addresses liver regrowth after partial hepatectomy.

Only a few models exist that represent liver regeneration at the organ scale. They are primarily phenomenological and mostly based on ordinary differential equations (ODE), and focus on the temporal evolution of the regeneration process, integrating risk factors for postoperative liver failure [3]. Phenomenological models predicting postoperative liver volume regeneration and assessing whether the liver will fully recover or suffer irreversible size reduction based on preoperative physiological factors and surgical parameters are published in [42]–[45].

1.2.2 Mesoscopic scale

On the mesoscopic scale, models exist that focus on the perfusion of idealized liver lobules. In [46], a model has been introduced that simulates blood distribution within lobules by depicting the liver's blood flow architecture as a combination of tree-shaped networks and porous systems. In [47], the authors developed a mathematical model to investigate blood flow dynamics within liver lobules, treating them as a porous medium. This approach examines the effects of pressure variations after liver resection, and the consequent impact on blood flow and tissue deformation. In [48], the authors developed a 3D image-based model of liver microcirculation to simulate blood flow through reconstructed human liver sinusoids. Their findings indicate that permeability in the liver lobules is directionally dependent, with higher permeability along the central vein compared to the radial and circumferential directions. This underscores the necessity of incorporating sinusoidal anisotropy into liver perfusion models. In [49], the authors extended existing liver lobule models by integrating vascular septa and anisotropic permeability, improving the representation of microcirculatory dynamics. Their results suggest that including vascular septa leads to more homogeneous perfusion patterns that more accurately represent physiological conditions.

Liver lobule models have also been extended to simulate the relationship between liver function and perfusion. For example, a two-scale continuum model was proposed to describe liver perfusion and cell metabolism, combining a porous medium approach for blood flow in lobules and a model for cell-level metabolism [50]. The framework integrates perfusion and metabolic processes through a coupled system of partial and ordinary differential equations (PDE–ODE), accounting for key components like glucose, lactate, and glycogen. In [51], [52], a computational model was introduced to study fat distribution within liver lobules, integrating microperfusion, oxygen gradients, and fat metabolism. The model simulates the interactions between perfusion and metabolic processes, predicting fat accumulation patterns based on various factors such as perfusion, oxygen levels, and free fatty acid concentrations. In [53], a multi-component, tri-phasic, bi-scale model was proposed to explore the coupled effects of perfusion, metabolism, and fat deposition.

A model for liver remodeling processes has been developed within the framework of continuum porous media theory, focusing on two-dimensional liver lobules. For example, in [54], a biphasic mechanical model was used to investigate how pressure gradients drive vascular remodeling after liver resection, particularly the formation of new sinusoidal canals to restore venous drainage.

In [55], an efficient reduced-order model was introduced for simulating blood perfusion in liver lobules, using Darcy's equation. This approach employs a mapping technique to avoid meshing for each lobule geometry, incorporates proper orthogonal decomposition and discrete empirical interpolation, which demonstrates high accuracy and computational efficiency.

1.2.3 Cell scale

At the cell scale, discrete models, e.g., based on cellular automata, have been developed to represent the proliferation of cells that occur during tissue growth [56].

In [57], the authors developed a cellular automaton-based model to simulate liver tissue damage and repair, focusing on the dynamics of hepatocyte proliferation, necrosis and injury propagation. The model predicts tissue outcomes based on key parameters such as cell proliferation and death rates, identifying critical thresholds that determine whether tissue will survive or undergo irreversible damage.

Additionally, agent-based models have gained traction for simulating mechanical and physiological phenomena in cells and tissues [58]. In this context, agent-based models have been used to explore tissue mechanics by capturing the behavior of individual cells and their interactions. These models range from lattice-based approaches (e.g. cellular automata) [59] to off-lattice models (e.g. deformable cell models) [59] and hybrid discrete-continuum models [60], [61], each offering different capabilities and limitations depending on the biological processes under study [58], [62].

A model that integrates cell-scale dynamics within a lobule-scale framework is published in [63]. The model operates primarily at the cell scale and focuses on individual hepatocytes and their behaviors during the regeneration process. Key parameters include cell division probability, coordinated cell orientation, cell cycle duration, migration activity, and cell polarity.

In another study [64], a single-cell-based biophysical model has been developed to investigate the spatio-temporal growth dynamics of two-dimensional tumor monolayers and three-dimensional tumor spheroids. The model allows for an analysis of how nutrient availability and biomechanical forces influence individual cell behavior and overall tumor properties.

In [65], the authors developed a mathematical model to predict the mechanism of hepatocyte-sinusoid alignment during liver regeneration. The model captures the regeneration process and demonstrates that the alignment of daughter hepatocytes along the orientation of the nearest sinusoids is essential for restoring tissue architecture.

A separate study [66] introduced a model that focuses on the overall kinetic processes of hepatic glucose metabolism, integrating multiple metabolic pathways (glycolysis, gluconeogenesis, glycogen metabolism) and their hormonal regulation in human hepatocytes.

Another approach at the cell scale is based on Monte Carlo simulations, which offer a stochastic framework for modeling the dynamics of tissue-cell populations and investigating complex processes such as pattern formation and tissue repair [67], [68].

1.3 Aims and outline

The primary aim of this thesis is to develop such a multiscale-multiphysics framework that integrates models associated with different physics at multiple spatial scales, enabling the simulation of the effect of liver tissue regrowth on the perfusion capability of a full-scale liver. The simulations will address several spatial scales, ranging from the lobular level to the organ level, providing a comprehensive view of liver regrowth.

This framework will integrate several key components, which are published in [14]–[16], [69]–[71]. My contributions as a first author are published in [69], [70]:

- **Synthetic vascular tree generation:** In [14], an alternative method to CCO for generating synthetic vascular trees was developed. This method is based on rigorous mathematical optimization. Unlike CCO, it enables the generation of a tree that optimizes both the tree geometry and its topology. The algorithmic complexity of this framework was improved, while complex physiological effects such as the non-Newtonian behavior of blood were investigated up to the microcirculation [15]. In [16], the approach to synthetic tree generation was extended to multiple non-intersecting vascular trees within non-convex organs, allowing for consistent representation of both supplying and draining vasculature simultaneously. The generation of vascular trees is crucial for accurately simulating blood flow in the liver after resection.

- **Poroelasticity-based perfusion modeling:** The core of the perfusion simulation is a continuum poromechanics-based approach that represents liver tissue as a deformable, poroelastic medium. A liver perfusion model will be extended by incorporating a poroelastic framework capable of simulating the coupled effects of blood flow and tissue deformation. This will allow for the consideration of changes in liver perfusion as the liver regenerates and grows. In [69], a first approach to a whole-organ perfusion model was presented, based on the coupling of a discrete synthetic vascular tree framework (macroscale vasculature) and poroelasticity (meso- and lobule-scale vasculature). This model will be extended using a multi-compartment approach to account for vascular features across various spatial scales [70].

- **Liver regrowth framework:** A continuum mechanics-based model for liver regrowth will be introduced and coupled with a multiscale perfusion model to predict changes in liver perfusion and deformation characteristics over time. Through this framework, the growth of liver tissue at the organ level will be modeled, incorporating interactions between regenerating tissues and their mechanical environment. The accuracy of the liver regrowth simulations will be ensured by calibrating and validating the model against experimental data. This process involves comparing synthetic vascular trees with data of real trees and calibrating the growth evolution equation using experimental data.

The structure of the thesis is as follows:

In **Section 2**, the multiscale mechanisms of hepatic vasculature and perfusion, perfusion-related factors that drive liver growth, different liver resection procedures and basic concepts for their modeling are explained.

In **Section 3**, the concepts of continuum poroelasticity at finite strains are introduced, and the kinematics, balance laws, and constitutive equations of the poroelastic model are provided in terms of a two-phase pressure-displacement formulation.

Section 4 reviews the method for synthetically generating vascular trees based on mathematical optimization. Existing approaches from the literature are first reviewed,

followed by the introduction of a new method published in [14]–[16]. The section includes explanations of the method's improvements and advantages over existing approaches, along with validation of its results against real data from human liver trees.

In **Section 5**, the continuum poroelastic and discrete vascular tree models are connected through suitable interface assumptions regarding geometry and boundary conditions. Additionally, the weak formulation of the poroelastic model is derived. The characteristic behavior of the poroelastic model is first discussed through a two-dimensional test problem, and subsequently applied to a three-dimensional liver resection. The approach is critically assessed, and improvements to be applied in the following sections are discussed.

In **Section 6**, the framework is developed by successively combining three model components. First is a discrete vascular tree approach, which represents blood supply and drainage at the organ scale. This is followed by a multi-compartment homogenized flow model for perfusion at lower levels of the hierarchical tree network and liver lobules, and an isotropic growth model of a poroelastic medium to represent hyperplasia of liver lobules. Coupling mechanisms and boundary conditions are also discussed, and the driving force that initiates compensatory liver tissue growth is motivated. The characteristics of each modeling step are briefly illustrated using a two-dimensional test problem.

In **Section 7**, the capabilities of the computational framework are demonstrated for a full-scale patient-specific liver example, with the typical perfusion outcome associated with a common surgical cut pattern. This also includes a statistical analysis to better assess the effects of liver resection on volumetric blood flow rates.

In **Section 8**, the thesis concludes with a discussion of the results, potential clinical impact, and directions for future research.

2 Liver regrowth: biological mechanisms, anatomy, and functional insights

We start by describing the general characteristics and the function of the human liver. We then dive into the multiscale anatomy of the liver, with a particular focus on its vasculature that determines liver perfusion. After, we explain different liver resection procedures. We then describe the perfusion-related factors that drive regrowth. We focus on the mechanisms from the lobule scale upwards, which are the ones relevant for the current modeling framework. We close this section by outlining the causes of liver failure.

2.1 General characteristics and liver function

The liver is the main site of metabolization and detoxification of xenobiotics in the human body and is the largest internal organ, located in the upper right quadrant of the abdomen (Fig. 2.1). It is located just below the diaphragm, with partial protection from the lower ribs. In adults, it typically weighs around 1.4 kg and measures about 15 cm in width [4].

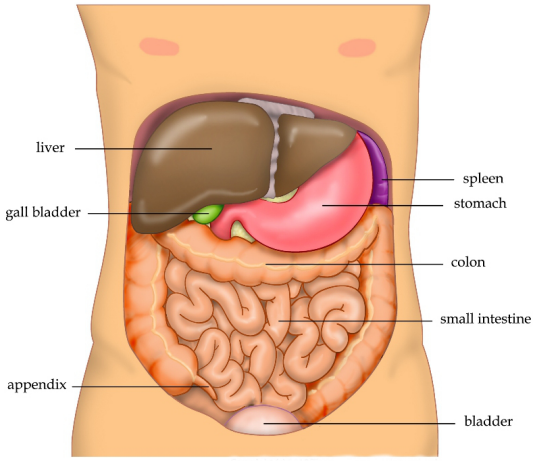

Figure 2.1: The human liver [1].

[1]Source: `https://en.wikipedia.org/wiki/Liver`

The liver consists of two primary lobes: the right lobe (lobus dexter) and the left lobe (lobus sinister) (see Fig. 2.2). The right lobe is significantly larger, being roughly six times the size of the left lobe. Additionally, two smaller lobes, the caudate lobe (lobus caudatus) and the quadrate lobe (lobus quadratus), are located on the underside of the liver. The liver is generally described as wedge-shaped, with a smooth and glossy surface.

The liver is encased in a thin, fibrous layer called Glisson's capsule, which serves as a protective covering. It is also secured in place by various ligaments, including the falciform ligament, which connects the liver to the abdominal wall and diaphragm. This ligament also separates the larger right lobe from the smaller left lobe.

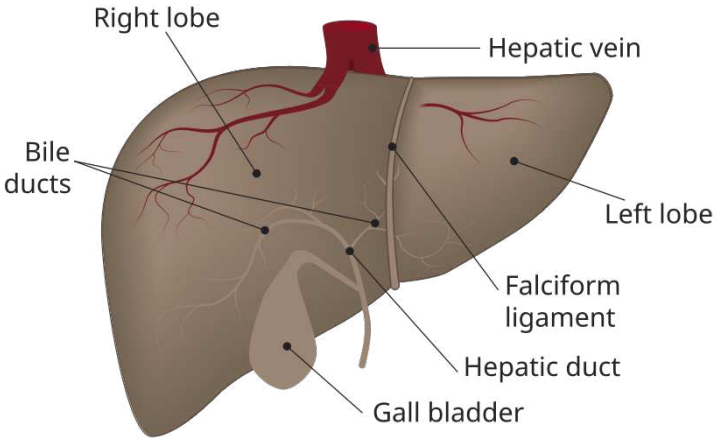

Figure 2.2: Human liver with its lobes [2].

The liver plays a crucial role in maintaining numerous physiological processes, with its functions broadly categorized into metabolic, storage, detoxification, synthetic and immunological roles [72].

- Metabolic functions: The liver is essential for the body's metabolic processes, significantly influencing carbohydrate, lipid, and protein metabolism. It maintains blood glucose homeostasis by transforming glucose into glycogen for storage (glycogenesis), breaking down glycogen into glucose (glycogenolysis), or synthesizing glucose from non-carbohydrate sources (gluconeogenesis). In lipid metabolism, the liver produces cholesterol and triglycerides, and it also transforms carbohydrates and proteins into fatty acids and triglycerides. Regarding protein metabolism, the liver deaminates amino acids and produces ammonia, which is subsequently converted into urea for excretion. Additionally, it synthesizes various plasma proteins and non-essential amino acids.

[2]Source: `https://commons.wikimedia.org/wiki/File:Liver_Diagram.svg`

- Storage functions: The liver serves as a storage for various vital substances. For example, it stores glycogen as a quick energy reserve to help regulate blood glucose levels during fasting. Additionally, the liver stores fat-soluble vitamins (A, D, E, and K), vitamin B12, and minerals such as iron, to meet the body's needs during periods of deficiency.

- Detoxification functions: The liver serves as the body's main detoxification organ, essential for processing drugs and toxins through various chemical reactions. These processes transform harmful substances into less toxic, water-soluble forms that can be more easily eliminated. It also detoxifies ammonia, a toxic byproduct of protein metabolism, by converting it into urea, which is then excreted by the kidneys.

- Synthetic functions: The liver synthesizes several vital substances necessary for the proper function of the body. It produces bile, stored in the gallbladder and released into the small intestine to aid in digestion. The liver also produces key plasma proteins, including albumin, which supports blood pressure regulation, and clotting factors essential for blood coagulation. Additionally, the liver produces and regulates hormones and growth factors, which are essential for growth and development.

- Immunological functions: The liver with its immunological functions is crucial in sustaining overall health. For instance, Kupffer cells can eliminate up to 99% of bacteria from portal vein blood. Additionally, the liver produces cytokines and other factors which help to maintain immune homeostasis.

The liver's diverse functions are crucial for sustaining overall health and balance in the body. Its involvement in metabolism, synthesis, storage, detoxification, and immune regulation underscores its significance as a vital organ of the body. Understanding these functions is key to recognizing how liver dysfunction can influence health and contribute to a range of diseases.

2.2 Multiscale vasculature and liver perfusion

Liver functions rely on its vasculature that enables the perfusion of the complete liver with blood [73]. Understanding this vascular architecture is crucial for comprehending the liver's role in nutrient processing, detoxification, and metabolic regulation. Figure 2.3 illustrates the multiscale nature of liver vasculature.

2.2.1 Macroscopic hepatic vasculature

At the organ (or macro-) scale, the liver receives a unique dual blood supply from the hepatic artery and the portal vein, each with diameters up to 1 cm, and blood exits through the hepatic veins. The hepatic artery originates from the heart and carries oxygen-rich blood, and the portal vein stems from the digestive tract and carries nutrient-rich blood.

The human liver has an overall blood flow supply of about 1.5 l/min, which translates to approximately 100-130 milliliters per minute per 100 grams of tissue [74].

The liver's arterial blood supply constitutes roughly 25% of its total blood flow but delivers about 50% to 80% of the organ's oxygen. This inflow is pulsatile, averaging 350-400 ml/min at a pressure of 100 mmHg. The hepatic artery divides into left and right branches, which further branch into smaller arterioles that enter the liver lobules, supplying oxygen to hepatocytes to sustain their high metabolic activity.

In contrast, venous blood makes up about 75% of the liver's blood flow. The portal vein provides a steady flow of around 1.1 l/min at a pressure of 7-10 mmHg. It branches extensively within the liver, initially splitting into left and right branches, and then further into segmental branches, which deliver blood into the hepatic sinusoids where nutrients and other substances are processed.

In the liver, the vessels of the hepatic artery and portal vein are generally arranged in parallel and run within structures known as portal triads. Alongside these vessels, the portal triads also include ducts from the biliary tree, which run parallel to both the hepatic artery and portal vein.

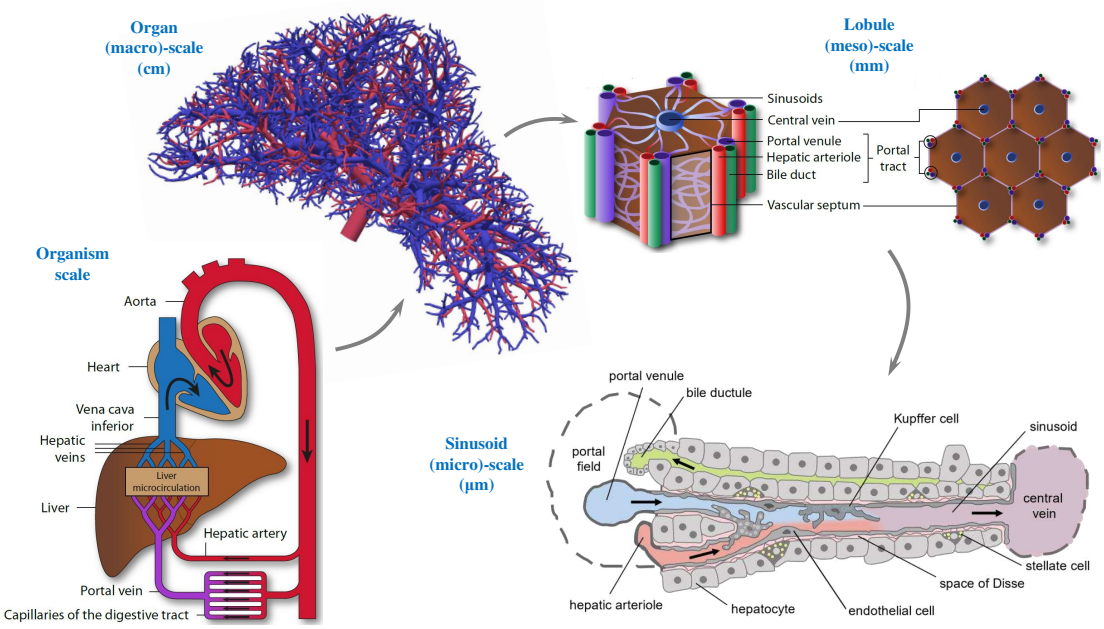

Figure 2.3: Multiscale liver vasculature (organism- and lobule-scale pictures from [4]) and sinusoid-scale picture from [75] (Licence: CC BY 2.5).

After circulating through the liver's intricate microvasculature, blood collects in the central veins of the lobules. These central veins converge to form the major hepatic veins (right, middle, and left hepatic veins) which drain deoxygenated blood from different liver regions into the inferior vena cava. From there, the blood returns to the heart. The liver maintains a steady outflow with an average rate of about 1.5 l/min and a pressure range of 3 to 5 mmHg [74].

2.2.2 Microscopic hepatic vasculature

At the lobule (or micro-) scale, the blood is driven through sinusoids, small capillaries with a diameter of approximately 10 μm. The organ-scale vessels and the sinusoid microcirculation are connected by a hierarchical vascular tree that consists of up to 20 levels of bifurcations [76]. The sinusoids are uniformly distributed throughout the entire liver volume, forming a three-dimensional network around rows of hepatocytes that are responsible for the metabolic liver functions. The sinusoids are arranged in lobules with a characteristic size of 1.5 mm, forming the fundamental building blocks of the liver. Each lobule is classically idealized as a prismatic volume of hexagonal cross section with a supplying triad made of a hepatic artery, a portal vein and a bile duct at each of the six hexagon corners, and a draining central vein along the axis of the lobule. Liver lobules are organized in a structure similar to hexagonal cells found in bee honeycombs.

Some blood from the portal triads enters the vascular septa, which are shared vascular boundaries between adjacent lobules, bordered by portal triads on either side [76]. These vascular septa deliver blood to the tissue between the portal triads via a network of small microvessels known as septal branches, which extend from the portal triads. The blood then moves from the portal triads and vascular septa into the intricate network of hepatic sinusoids. Blood flow through these sinusoids can originate from the portal vein, the hepatic artery, or a combination of both.

Sinusoids lie between rows of hepatocytes and are lined with endothelial cells that have thin extensions perforated with small pores called fenestrae. These fenestrations allow nutrients, toxins, and other solutes from the blood to pass into the space of Disse, a narrow region between the endothelial cells of the sinusoids and the hepatocytes. This space also permits the movement of proteins and plasma. The sinusoids maintain a low pressure of 2-5 mmHg and slow blood flow, allowing hepatocytes to process and interact with the circulating blood [76]. At the center of each lobule is a central vein, where blood from the sinusoids drains before eventually flowing into the hepatic vein and then the inferior vena cava.

The unique liver's dual blood supply, comprising oxygenated blood from the hepatic artery and nutrient-rich blood from the portal vein, ensures a continuous and ample flow to sustain its vital functions. This efficient blood circulation allows hepatocytes to process nutrients and detoxify harmful substances before they enter the systemic circulation.

A thorough understanding of the liver's vascular structure is essential in clinical practice, especially for procedures like liver surgery and transplantation, as well as in the management of conditions such as cirrhosis and portal hypertension.

2.2.3 Liver cells

The liver contains a variety of specialized cells, each contributing uniquely to its complex functions. Key cell types include hepatocytes, Kupffer cells, hepatic stellate cells and endothelial cells (see Fig. 2.3). Grasping the roles of these cells is essential for understanding liver physiology.

Hepatocytes are the liver's primary cells, making up roughly 70-80% of its cellular mass. These large, polygonal cells are crucial for various liver functions, including metabolism, detoxification, and the synthesis of vital substances.

Kupffer cells are unique macrophages located within the liver sinusoids, forming the body's largest group of stationary immune cells. They are essential for the liver's immune defense.

Hepatic stellate cells, or Ito cells, lie in the space of Disse, positioned between hepatocytes and the endothelial cells of sinusoids. They play crucial roles in both the normal functioning and pathological changes of the liver.

The hepatic sinusoids are lined by specialized endothelial cells with fenestrations, facilitating the exchange of nutrients and waste between the blood and liver cells. These unique cells are vital for the liver's filtration and metabolic processes.

The liver's diverse functions depend on the interplay between its various cell types. This coordination is essential for maintaining liver health and understanding its response to damage, highlighting the organ's critical role in overall physiological balance.

2.3 Liver resection

Liver resection, or hepatectomy, is a surgical procedure performed to remove a portion of the liver. This procedure is primarily performed to address liver malignancies, including primary tumors like hepatocellular carcinoma (HCC) and metastatic tumors from cancers such as colorectal cancer [77]. It is also performed for the removal of symptomatic benign liver tumors like hemangiomas, hepatic adenomas, and focal nodular hyperplasia, particularly when they lead to complications [78]. Liver resection might also be required for substantial or problematic liver cysts and abscesses that fail to improve with alternative therapies.

The liver possesses the remarkable ability to regenerate itself after resection or following injuries [79], [80], which enables the removal of a large portion of its tissue while still permitting full recovery and restoration of function. The liver's remarkable ability to regenerate itself after resection or injury has been a subject of fascination for centuries. This regenerative capacity is not only a critical aspect of liver physiology but also a cornerstone of various medical treatments, including liver surgery and transplantation. This unique characteristic of the liver is famously depicted in Greek mythology, where Prometheus's liver would regrow overnight after being eaten by an eagle daily, signifying the organ's extraordinary regenerative ability (Fig. 2.4).

Figure 2.4: Prometheus with the eagle[3].

This regenerative capacity supports the effectiveness of liver resection as a viable treatment option. Various surgical approaches are used for liver resection, chosen according to the tumor's size, its position, and the patient's general condition.

2.3.1 Surgical approaches

Traditional open liver resection involves a large abdominal incision (laparotomy) to access the liver directly, providing a thorough view of the liver and nearby organs, which is particularly advantageous for complex cases [81]. However, this approach typically results in longer recovery periods, and a higher risk of complications like infections and significant blood loss and increased postoperative pain.

On the other hand, laparoscopic liver resection is a minimally invasive procedure that uses small abdominal incisions to insert a laparoscope (a slender tube with a camera) and specialized tools [78]. This technique offers benefits such as reduced postoperative pain, shorter hospital stays, quicker recovery, and less visible scarring. Nevertheless, laparoscopic resection requires advanced surgical skills and may not be feasible for larger or challenging tumors, limiting its applicability for some patients.

Robotic-assisted liver resection is an advanced surgical approach that utilizes robotic technology to improve precision, control, and visualization during minimally invasive procedures [82]. This technique enhances the advantages of laparoscopic surgery by offering greater maneuverability and potentially superior results. However, the use of robotic systems comes with higher costs, extended surgical durations, and the necessity for specialized training and expertise.

Beyond traditional surgical methods, ablation therapies like radiofrequency ablation (RFA), microwave ablation, and cryoablation provide non-invasive options for treating liver tumors by targeting and destroying cancerous cells without the need for tissue removal [83]. These techniques can be applied either through the skin or via laparoscopic approaches, making them viable for patients who may not qualify for conventional

[3]Source: `https://de.wikipedia.org/wiki/Prometheus`

surgery. Despite their advantages, these methods are typically effective only for smaller tumors and may present challenges such as incomplete treatment and the possibility of tumor regrowth.

2.3.2 Preoperative planning and postoperative recovery

Effective and successful liver resection requires thorough preoperative preparation [84]. Comprehensive imaging techniques like computed tomography (CT), magnetic resonance imaging (MRI), and ultrasound are vital for assessing the tumor's size, location, and its proximity to critical blood vessels. Assessing liver function through blood tests and other diagnostics is crucial to ensure adequate liver performance after surgery. Furthermore, evaluating the patient's overall health and any existing comorbidities is essential for selecting the optimal surgical method and mitigating potential complications.

Postoperative management and recovery play critical roles in the liver resection process [85]. Close monitoring in the initial recovery phase is essential to identify and address complications like bleeding, infection, or liver dysfunction. Pain control is important for recovery and reducing the risk of complications, while nutritional support helps foster liver regeneration and overall healing. Ongoing follow-up is necessary to track liver function, check for potential cancer recurrence, and handle any long-term issues that may arise.

2.3.3 Anatomical versus non-anatomical resection

Resections of the liver can involve various cutting planes depending on the location and extent of the tumor, as well as the patient's overall health. Besides the size of the pathology, the choice of cutting plane is also determined by the goal of preserving as much liver tissue as possible. These factors are carefully considered by surgeons in order to preserve sufficient liver function while achieving the best possible outcome [3].

In practice, there exist two ways of carrying out a resection [86]. One is anatomical resection, which involves removing portions of the liver along anatomical boundaries. The liver is partitioned into eight functionally independent segments, where each segment is supplied by its own larger branch of the supplying tree, which splits into smaller vessels within the segment, and is connected to a larger branch of the draining tree (see Fig. 2.5). This is also known as the Couinaud classification, which enables segmental resections without affecting other segments [87]. Examples include left hepatectomy, right hepatectomy, and segmental resections. The second option is a non-anatomical cut which involves removing a part of the liver that does not strictly follow the anatomical boundaries, for instance, when the tumor is distributed over multiple segments. In this case, the surgeon is faced with the decision between the risk of tumor recurrence and the risk of liver failure [3].

In this context, assessing changes in perfusion, flow redistribution and the mechanical response of the resected liver has clinical relevance [79]. An insufficient blood supply can result in ischemia, where the tissue does not receive enough oxygen and nutrients. Prolonged ischemia can cause tissue damage and death. Therefore, the liver's regenerative

capacity can be impaired if a significant part of the tissue does not receive prolonged sufficient blood supply. The parts of the associated isolated vasculature which are cut off and no longer supplied with blood, are often denoted as *orphans*.

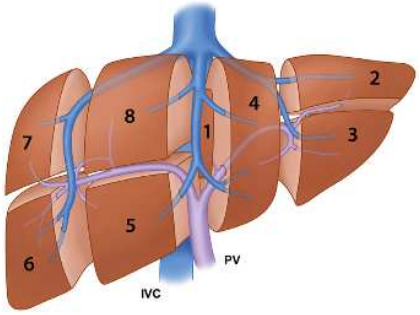

Figure 2.5: Division of the human liver into eight segments corresponding to the portal vein and inferior vena cava (anterior view). From [88] (Licence: CC BY).

2.4 Liver regeneration and driving mechanisms at the microscale

Since blood from the portal vein cannot easily bypass the liver to return to the heart, almost the same volume of blood needs to flow through the smaller liver remnant after PHx. As a consequence, massive hemodynamic changes occur immediately after PHx. To enable the same blood flow through a reduced cross section, the portal pressure needs to increase (portal hypertension). In contrast to the portal vein, blood from the hepatic artery can continue to flow through the aorta to other parts of the gastrointestinal tract and legs. Therefore, the hepatic artery contracts when the portal pressure increases (hepatic arterial buffer response). As a result of hypertension, a larger difference in pressure occurs between the portal venules on the one hand and the central veins on the other hand. Therefore, the flow increases in the remaining vasculature, leading to a larger blood velocity and therefore increased shear stresses within the sinusoids [89], as illustrated in Fig. 2.6. This state is called *hyperperfusion*.

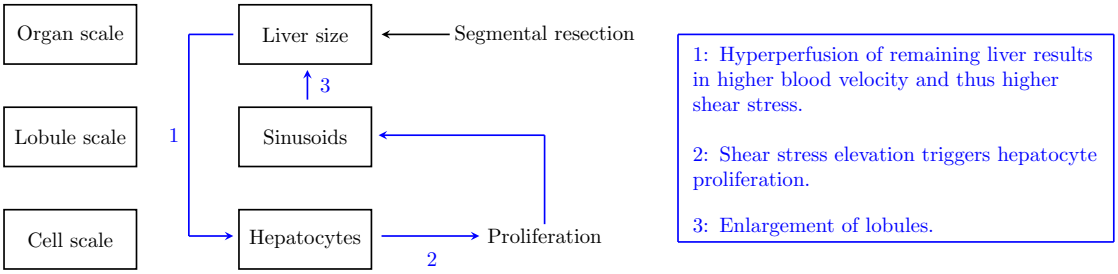

Figure 2.6: Influence of segmental resection on blood flow.

The liver can reach its original size within a few weeks. The restoration of liver mass primarily occurs through the rapid cell division of hepatocytes (proliferation) [89]. There is consensus that *hyperperfusion* is the central stimulus that triggers liver regeneration. Within the biomedical literature, there are different models that connect hyperperfusion and hepatocyte proliferation at the cell level, see e.g. [90], [91]. In order to provide the interested reader with a flavor of the underlying complexity, we briefly outline the model by [92], [93], illustrated in Fig. 2.7.

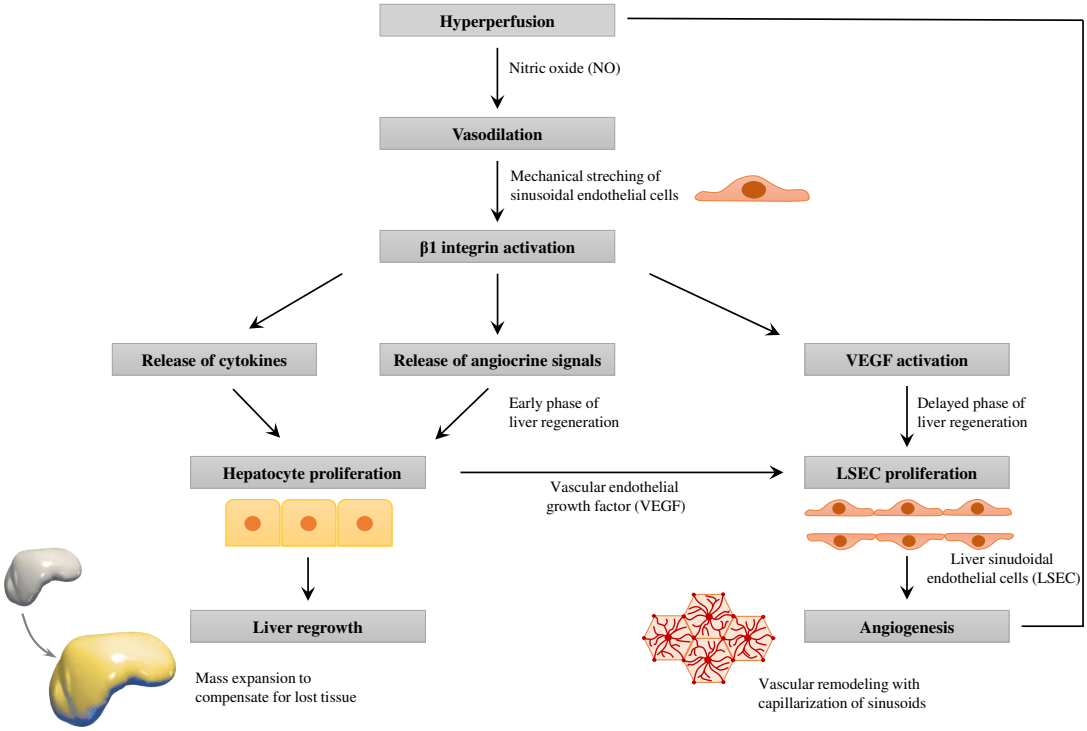

Figure 2.7: Liver size regulation after surgical resection (picture adapted from [93]).

Immediately after PHx, the increase in blood flow through the remaining sinusoids and the associated increase in shear stress at the vessel walls stimulates sinusoidal endothelial cells to release vasodilators such as nitric oxide (NO). The dilation of the sinusoids enables a larger flow of blood at a given pressure level and therefore limits portal hypertension, blood velocity and wall shear stress. Vasodilation requires the mechanical stretching of the endothelial cell layer, resulting in the release of growth-promoting angiocrine signals and mechanoresponsive $\beta 1$ integrin. Angiocrine signals constitute the main stimulus for hepatocyte proliferation, and hence are essential for liver regrowth. Integrin activation results in the reorganization of the components of the extracellular matrix, triggering the release of cytokines. Both integrin and cytokines contribute to the release of further growth factors to support hepatocyte proliferation.

The proliferation of hepatocytes increases the volume of the remaining lobules (hy-

perplasia), where the hepatocyte plates are up to twice as thick as they initially are [79]. Thus, the remaining liver expands in mass to compensate for the lost tissue (compensatory growth), but does not restore its original shape and the excised parts do not grow back [94]. To guarantee liver function, the added hepatocyte cells need to be supplied with blood in the same way as before, which requires the formation of new vessels (angiogenesis), primarily at the level of microcirculation. Angiogenesis is primarily based on the proliferation of sinusoidal endothelial cells. It is driven by endothelial growth factor (VEGF) released by proliferating hepatocytes and the mechanically stretched endothelial cells themselves. The resulting vascular expansion process leads to the formation of an extended vascular network of sinusoids (lobular remodeling).

The rate of regeneration depends on several factors, including the extent of the resection, the general physical condition and health of the patient, and any pre-existing liver diseases [89], [95]–[97]. In general, hepatocyte proliferation starts immediately and heavily after partial liver resection (early phase of liver regeneration). Angiogenesis and lobular remodeling starts after a few days (delayed phase of liver regeneration). For instance, following a two-thirds removal, the normal liver weight is restored within 8 to 15 days in humans, followed by several weeks of slow lobular remodeling [79].

Once the lost tissue mass and the vascular network is restored, hyperperfusion ceases, as enhanced blood flow and pressure is not required in the hepatic vasculature to guarantee the required volume of blood to pass through the liver. Therefore, all cell proliferation processes stop and liver regeneration is complete.

2.5 Liver failure

Postoperative liver failure is a critical risk following liver resection, influenced by factors such as the extent of the surgery, pre-existing liver conditions, and potential surgical mistakes [98]. Addressing these elements is therefore essential for mitigating the risk of liver failure and achieving the best possible outcomes for patients.

Posthepatectomy liver failure (PHLF) arises when the liver's residual tissue cannot adequately perform vital metabolic, synthetic, and detoxification roles [99]. The likelihood of PHLF rises with more extensive resections, particularly in individuals with pre-existing liver conditions like cirrhosis or fatty liver disease. If the remaining liver mass falls below critical thresholds—approximately 20-35% in healthy livers and 40% in compromised livers—the liver may fail to maintain necessary functions [100]. Additionally, accidental injury to the hepatic artery, portal vein, or hepatic veins can result in significant blood loss and compromised liver blood flow, potentially triggering liver failure.

The success of liver regeneration and function following resection heavily depends on the integrity of the hepatic vasculature and perfusion. Disruptions in hepatic blood flow can lead to PHLF, a serious and potentially fatal condition.

For preoperative evaluation, advanced imaging techniques like CT or MRI angiography are employed to examine the liver's vascular network and strategize the resection. However, these images may not always clearly reveal all blood vessels due to resolu-

tion limitations. A thorough understanding of the liver's vascular anatomy is crucial to prevent unnecessary injury to vital blood vessels during surgery.

Effective postoperative care requires close monitoring of liver hemodynamics and function to detect any abnormalities. Maintaining a careful fluid balance is crucial to preserving proper liver perfusion. In this context, ischemia also plays an important role, as inadequate blood flow can severely impact liver recovery.

3 Continuum poroelasticity

In order to study the mechanical properties of the liver, we treat it as a porous medium, which reflects its highly vascularized and structurally complex nature. The liver's sponge-like structure, characterized by a dense network of blood vessels and sinusoids, supports efficient fluid flow and substance exchange. The porous structure of the liver is crucial for the liver's function and has a significant impact on its mechanical properties. Using continuum poroelasticity principles enables us to understand the liver's response to different physiological conditions and its notable regenerative capacity.

Therefore, in this section, we review poroelasticity at large strains and provide the balance laws and the constitutive laws of the poroelastic model that we will use in the following.

3.1 Introduction to poromechanics

Poromechanics is a field that involves studying how the mechanical behavior of materials with internal pores is influenced by the fluids that saturate these spaces. Since poromechanics has potential applications in a variety of engineering fields ranging from civil [101], chemical [102] and geotechnical [103] engineering to biological [104] or medical [105] sciences it has been subject of many theoretical and numerical studies over the last few decades [106]–[111].

The theory originated in the pioneering work of Terzaghi in soil mechanics [112]. Later, Biot extended the work by applying the elasticity theory to describe the mechanical behavior of the solid phase and Darcy's law for fluid flow through porous media [113], [114].

The key characteristic explored in poromechanics is the interaction between their solid components and the fluids that occupy their pore spaces. This interaction leads to coupled processes such as hydro-diffusion, swelling, shrinkage, drying, heating, as well as cracking. The main objective of poromechanics is to provide a framework for analyzing the interconnected processes occurring in porous materials. This requires integrating continuum mechanics principles with the microscopic discontinuities inherent in porous materials. For that, the porous medium is treated as a superposition of several continua, each having different kinematic characteristics but interacting with one another.

3.1.1 The porous medium

A fluid-saturated porous medium is a material containing a solid skeleton and pores which are filled with fluid. Examples include substances that can be found in both nature, e.g. hard or soft biological tissues [115]–[120], and engineering [121], e.g. soil

[103], concrete [101] and wood [104]. In Biomechanics, hard and soft tissues can be considered as deformable, permeable and porous media [115]–[120].

In poromechanics, the porous medium is viewed as the superposition of two continuous phases: the solid skeleton and the fluid. Within the porous medium, an infinitesimal portion of the porous medium can be considered as comprising both a solid skeleton particle and a fluid particle. The skeleton particle includes the solid matrix and the interconnected empty pore spaces, whereas the fluid particle includes the fluid filling these pores along with the space not occupied by the solid matrix. The so-called porosity denotes the ratio of interconnected pore volume to the entire volume of the porous medium.

To accurately model a medium with microscopic heterogeneity, a macroscopic scale is selected. This approach averages out the microscopic heterogeneity, allowing for the examination of larger-scale physical phenomena. Porosity is therefore related to a volume element that is adequately large to represent the filtration process comprehensively. Therefore, a representative volume element is key to preserving the continuity of physical properties within the porous medium.

The continuity assumption in a porous medium considers that its properties change smoothly across the domain. This also means that the deformation of the skeleton is continuous, ensuring that nearby particles remain in their relative positions over time. This continuity is essential for understanding how porous media behave under different physical conditions.

3.1.2 Homogenization and Representative Volume Element

In porous media theory, the principles of homogenization and the Representative Volume Element (RVE) are used to calculate effective properties that capture the medium's behavior across a range of physical processes [122]–[125]. Homogenization is a conceptual and mathematical approach to bridge the gap between microscale and macroscale properties of heterogeneous materials. The primary idea behind homogenization is to replace the complex, detailed microscopic structure with a simplified homogeneous medium that effectively represents the macroscopic behavior of the initially heterogeneous material. In porous media, it helps in determining effective macroscopic properties by averaging the complex behavior at the microscopic level over a sufficiently large volume. Therefore, it simplifies the material's analysis by treating it as a uniform continuum, regardless of its underlying heterogeneous characteristics. The effective properties obtained through homogenization, including permeability, porosity, and stiffness, can then be incorporated into macroscopic models and simulations for analysis.

In the context of homogenization, the RVE plays a crucial role. An RVE is a small volume of material that statistically captures the characteristics of the entire medium. It includes enough microscopic heterogeneities, like pores, ensuring that the averaged properties of this volume accurately reflect those of the entire material and that the material's porosity and permeability are accurately represented.

The RVE size needs to be precisely determined: it should be large enough to capture a representative range of the material's microstructural details, yet small enough to be

effectively treated as a point in macroscopic terms. A RVE that is too small may fail to capture the complete range and intricacy of the microstructure, resulting in inaccurate homogenized properties. On the other hand, an excessively large RVE can make analysis computationally burdensome.

3.2 Kinematics

Classical poromechanics is rooted in continuum mixture theory [126]. Continuum mixture theory is a general mathematical theory that provides a framework for deriving (simplified) continuum mechanics models for a large number of multi-physics problems. For an extensive review on poromechanics we refer to [127]–[129], and note a number of important theoretical and numerical studies in the field of poromechanics [115], [130]–[135].

3.2.1 Deformation of porous medium and deformation gradient

The core principle in poromechanics is that the porous material is composed of multiple constituent bodies that simultaneously occupy a common region in space. In this work, we rely on the common assumption that the Lagrangian configuration of the constituent bodies coincides. This means that we work with a single Lagrangian description.

At the initial time $t = 0$, the mixture is considered to be in the reference configuration Ω_0. In this configuration, a particle is identified by its Lagrangian position vector $\boldsymbol{X} \in \Omega_0$. The spatial position (motion) of a particle is given by the (invertible) deformation map:

$$\boldsymbol{x} = \boldsymbol{\chi}(\boldsymbol{X}, t), \tag{3.1}$$

where $\boldsymbol{x} \in \Omega$ denotes the spatial position and Ω is current domain of the mixture.

The relationship between these positions can be described by the displacement vector $\boldsymbol{u}$. We use the standard notation for the displacement of the mixture, given by

$$\boldsymbol{u} = \boldsymbol{x} - \boldsymbol{X}. \tag{3.2}$$

Furthermore, we denote the Lagrangian velocity as $\boldsymbol{v} = \dot{\boldsymbol{u}}$, where the dot represents the material derivative.

We define the deformation gradient $\boldsymbol{F}$ which relates the initial and current configurations through the displacement field:

$$\boldsymbol{F} = \frac{\partial \boldsymbol{x}}{\partial \boldsymbol{X}} = \boldsymbol{I} + \nabla \boldsymbol{u}, \tag{3.3}$$

where $\boldsymbol{I}$ represents the identity matrix and $\nabla \boldsymbol{u}$ denotes the spatial gradient of the displacement vector.

Any infinitesimal volume element $d\mathcal{V}$ in the deformed configuration is related to the

corresponding infinitesimal initial volume element $d\mathcal{V}_0$ by the expression

$$d\mathcal{V} = J d\mathcal{V}_0, \tag{3.4}$$

with $J = \det(\boldsymbol{F})$ representing the Jacobian of the deformation gradient.

The transformation of any infinitesimal material surface element dA in the undeformed state into the deformed surface element da is given by Nanson's formula [136]

$$\boldsymbol{n} da = J \boldsymbol{F}^{-T} \cdot \boldsymbol{N} dA, \tag{3.5}$$

where $\boldsymbol{N}$ and $\boldsymbol{n}$ are the unit normal vectors in the undeformed and deformed configuration, respectively.

Given any vector $\boldsymbol{z}$ in the deformed configuration, its corresponding vector $\boldsymbol{Z}$ in the reference configuration can be determined such that the flux of $\boldsymbol{z}$ through the current surface element da is equal to the flux of $\boldsymbol{Z}$ through the initial surface element dA. This can be expressed as

$$\boldsymbol{z} \cdot \boldsymbol{n} da = \boldsymbol{Z} \cdot \boldsymbol{N} dA. \tag{3.6}$$

This then results in the following relationship:

$$\boldsymbol{Z} = J \boldsymbol{F}^{-1} \cdot \boldsymbol{z}. \tag{3.7}$$

3.2.2 Mixture constituents and porosity

In this work, we consider a heterogeneous mixture composed of a single fluid and a single solid constituent, where superscripts f and s refer to quantities associated with the fluid and the skeleton phase, respectively. We denote the volume fraction of the fluid and solid (skeleton) constituents respectively as ϕ^f and ϕ^s. Since the skeleton is a deformable macroscopic structure, its deformation changes the structure of its pores. As a consequence, the volume fractions are time-dependent (and obviously space-dependent), i.e. $\phi^f = \phi^f(\boldsymbol{x}, t)$ and $\phi^s = \phi^s(\boldsymbol{x}, t)$. We assume that void spaces are absent, i.e.

$$\phi^f(\boldsymbol{x}, t) + \phi^s(\boldsymbol{x}, t) = 1, \tag{3.8}$$

for all $\boldsymbol{x} \in \Omega$ and $t \geq 0$. As a consequence, the composition can be described by the porosity $\phi = \phi(\boldsymbol{x}, t)$:

$$\phi^f = \phi, \tag{3.9a}$$
$$\phi^s = 1 - \phi. \tag{3.9b}$$

The porosity is a key characteristic of porous materials, defined as the ratio of the volume of the pore space to the overall volume of the material. This property quantifies the material's ability to contain fluids and is essential in understanding the behavior of porous structures across various applications.

The porosity ϕ can be mathematically expressed as

$$\phi = \frac{d\Omega^f}{d\Omega}, \tag{3.10}$$

where $d\Omega^f$ is the volume of the pore spaces and $d\Omega$ is the total volume of the mixture.

The role of porosity in porous materials is critical as it directly influences various properties of the material. For example, it directly controls the volume of fluid that can be stored within a mixture, therefore impacting its overall storage capacity. Additionally, the porosity is crucial for determining the effective properties of the material, such as its permeability or mechanical behavior. For example, increased porosity typically leads to higher permeability, allowing fluids to move more "freely" through the medium.

Furthermore, porosity directly affects various mechanical properties of a porous medium, including its strength, elasticity, and deformation behavior. Typically, as porosity increases, mechanical strength tends to decrease. Additionally, porosity also affects the efficiency of heat and mass transfer within the material, which is important for various practical applications.

At the macroscopic level, the solid-fluid mixture is typically considered a homogenized medium. We visualize our model in Fig. 3.1.

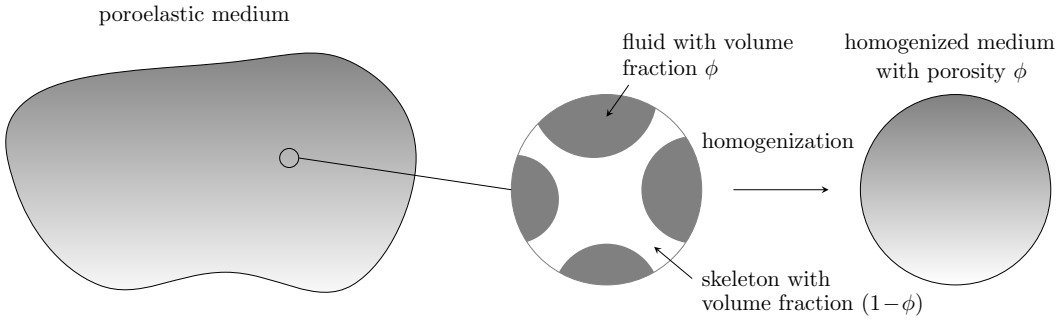

Figure 3.1: Continuum (homogenized) poroelastic mixture consisting of a skeleton and fluid constituent.

The partial mass densities of the fluid and solid constituents denote $\tilde{\rho}^f = \tilde{\rho}^f(\boldsymbol{x}, t)$ and $\tilde{\rho}^s = \tilde{\rho}^s(\boldsymbol{x}, t)$, respectively. These densities represent the mass of the associated constituents per infinitesimal mixture volume. The partial mass densities may be decomposed as:

$$\tilde{\rho}^f = \rho^f \phi, \tag{3.11a}$$
$$\tilde{\rho}^s = \rho^s (1 - \phi). \tag{3.11b}$$

In this paper, we assume that both constituents are incompressible, i.e.

$$\rho^f = \text{const}, \tag{3.12a}$$
$$\rho^s = \text{const}. \tag{3.12b}$$

The assumption of incompressible constituents is common in biomechanics, since the fluid pressure and solid stresses are typically negligible in comparison to the bulk modulus of the material [133].

3.2.3 Strain tensor

In the field of continuum mechanics, strain tensors are essential for capturing how materials deform under stress and provide a quantitative measure of the amount by which a material is stretched or compressed. In this section, we introduce various strain tensors, including their definitions and practical applications.

First, we introduce the right Cauchy-Green deformation tensor, defined as

$$\boldsymbol{C} = \boldsymbol{F}^T \boldsymbol{F}. \tag{3.13}$$

The right Cauchy-Green tensor $\boldsymbol{C}$ is a symmetric and positive-definite tensor, with non-negative eigenvalues.

The Green-Lagrange strain tensor, also known as Lagrangian finite strain tensor or Green–St-Venant strain tensor, is Lagrangian based and measures the strain relative to the undeformed configuration. It is directly defined as a function of the right Cauchy-Green tensor $\boldsymbol{C}$ and given by

$$\boldsymbol{E} = \frac{1}{2}(\boldsymbol{F}^T \boldsymbol{F} - \boldsymbol{I}). \tag{3.14}$$

The Green-Lagrange strain tensor is a quadratic measure of strain. It is particularly useful in the context of finite deformation problems, especially those that involve large strains (geometrically nonlinear) and hyperelastic material models.

The Almansi strain tensor, also known as the Eulerian strain tensor, is used to describe the deformation in the current configuration. It is defined as

$$\boldsymbol{e} = \frac{1}{2}(\boldsymbol{I} - \boldsymbol{b}^{-1}), \tag{3.15}$$

where $\boldsymbol{b} = \boldsymbol{F}\boldsymbol{F}^T$ describes the left Cauchy-Green deformation tensor. The Almansi strain tensor evaluates the strain of a material in its deformed state, proving particularly useful in fluid mechanics and other scenarios where the current deformation is more relevant than the initial condition.

In the context of small deformations, the linearized version of the strain tensor can be used, which is given by

$$\boldsymbol{\epsilon} = \frac{1}{2}(\nabla \boldsymbol{u} + (\nabla \boldsymbol{u})^T). \tag{3.16}$$

The linearized strain tensor provides a simplified approximation for small deformations by ignoring higher-order terms. It is extensively utilized in elasticity and structural analysis, where the deformations are small, and the linearity assumption is valid.

In certain applications that require strain to be additive across a series of deformations,

the Hencky strain tensor, or logarithmic strain tensor, is utilized. It is expressed as

$$\boldsymbol{H} = \frac{1}{2}\ln(\boldsymbol{C}) = \ln(\boldsymbol{U}). \tag{3.17}$$

Here, the tensor $\boldsymbol{U}$ denotes the right stretch tensor, which is obtained through the polar decomposition $\boldsymbol{F} = \boldsymbol{V}\boldsymbol{R}$. The Hencky strain tensor is particularly suited when dealing with materials that demonstrate a logarithmic strain response, such as metal forming processes.

3.3 Balance laws

In agreement with the continuum theory of mixtures, each constituent may be considered in isolation and its motion involves terms that model the interaction with the other constituents. The motion of the mixture is then a consequence of the individual evolution equations. In the scope of this work, we focus directly on the evolution equations relevant for the final poroelastic model, assuming quasi-static conditions.

3.3.1 Mass balance

The balance of fluid mass takes the form:

$$\partial_t(\rho^f \phi) + \nabla \cdot \left(\rho^f \phi \boldsymbol{v}^f\right) = \rho^f \theta, \tag{3.18}$$

where $\boldsymbol{v}^f$ denotes the velocity of the fluid and θ describes a mass source term ($\theta \geq 0$) or a sink term otherwise [115].

Next, we introduce the added mass quantity m and the perfusion velocity $\boldsymbol{w}$ as:

$$m = \tilde{\rho}^f J - \tilde{\rho}_0^f, \tag{3.19a}$$

$$\tilde{\rho}_0^f = \rho^f \phi_0, \tag{3.19b}$$

$$\boldsymbol{w} = \phi(\boldsymbol{v}^f - \boldsymbol{v}), \tag{3.19c}$$

where $\phi_0 = \phi_0(\boldsymbol{X}) = \phi(\boldsymbol{\chi}^{-1}(\boldsymbol{X}, 0), 0)$ represents the porosity in the reference configuration. The added mass m represents the variation in fluid mass content per unit volume of the undeformed skeleton. A straightforward calculation reveals that the evolution of the added mass is given by:

$$\frac{1}{J}\dot{m} + \nabla \cdot \left(\rho^f \boldsymbol{w}\right) = \rho^f \theta. \tag{3.20}$$

We relate the perfusion velocity $\boldsymbol{w}$ to the fluid pressure p in the pores using Darcy's law:

$$\boldsymbol{w} = -\frac{\boldsymbol{k}}{\eta}\nabla p, \tag{3.21}$$

where the quantity $\boldsymbol{k}$ describes the symmetric second order permeability tensor of the

mixture and η is the dynamic viscosity. We restrict ourselves to the isotropic case, i.e $\boldsymbol{k} = k\boldsymbol{I}$ with $k = \text{const}$ and rewrite $K = \frac{k}{\eta}$. We note that Darcy's law as constitutive relation is a standard choice in the literature. Considering the steady-state case and substitution of (3.21) into (3.20) provides

$$-K\nabla^2 p = \theta \quad \text{in } \Omega, \tag{3.22a}$$

$$-K\left(\boldsymbol{F}^{-T}\nabla_0\right)\boldsymbol{F}^{-T}\nabla_0 p = \theta \quad \text{in } \Omega_0, \tag{3.22b}$$

where we have used the pull-back operation $\nabla = \boldsymbol{F}^{-T}\nabla_0$ for the mapping of (3.22a) to the reference configuration Ω_0 with ∇_0 denoting the material gradient.

3.3.2 Momentum balance

We conclude this section with the balance of momentum written in the spatial form as

$$\nabla \cdot \boldsymbol{\sigma} + \rho^s(1-\phi)\left(\hat{\boldsymbol{b}} - \boldsymbol{a}^s\right) + \rho^f\phi\left(\hat{\boldsymbol{b}} - \boldsymbol{a}^f\right) = \boldsymbol{0}, \tag{3.23}$$

where $\boldsymbol{\sigma} = J^{-1}\boldsymbol{F}\boldsymbol{S}\boldsymbol{F}^T$ denotes the Cauchy stress tensor for the mixture, $\hat{\boldsymbol{b}}$ describes the body force per unit volume, $\boldsymbol{a}^s$ and $\boldsymbol{a}^f$ represent the accelerations of the skeleton and fluid phase and $\boldsymbol{S}$ is the second Piola-Kirchhoff stress tensor. A pull-back operation to the reference configuration provides

$$\nabla_0 \cdot (\boldsymbol{F}\cdot\boldsymbol{S}) + J\rho^s(1-\phi)\left(\hat{\boldsymbol{b}} - \boldsymbol{a}^s\right) + J\rho^f\phi\left(\hat{\boldsymbol{b}} - \boldsymbol{a}^f\right) = \boldsymbol{0}. \tag{3.24}$$

The balance of linear momentum in the reference configuration may also be written as

$$\nabla_0 \cdot (\boldsymbol{F}\boldsymbol{S}) = \boldsymbol{0} \quad \text{in } \Omega_0, \tag{3.25}$$

where we have considered a quasi-static setting with no internal forces, i.e. $\boldsymbol{a}^s = \boldsymbol{0}$ and $\boldsymbol{a}^f = \boldsymbol{0}$ and neglected body forces, i.e. $\hat{\boldsymbol{b}} = \boldsymbol{0}$.

3.4 Constitutive equations

Before defining the constitutive equations, we begin by introducing various stress measures and explaining their relevance.

3.4.1 Stress measures

The symmetric Cauchy stress tensor $\boldsymbol{\sigma}$ is a fundamental measure in stress analysis, representing the force applied per unit area on an infinitesimal element within the current configuration of the material. Therefore, when examining forces in the material's current state, the Cauchy stress tensor is particularly useful as it provides a direct depiction of physical forces applied per unit area. This makes it the most intuitive measure of stress.

The first Piola-Kirchhoff stress tensor $\boldsymbol{P}$ links forces in the deformed configuration and the corresponding areas in the undeformed reference state. It is in general not symmetric and is particularly advantageous for studying large deformation problems that involve both reference and current configurations. The first Piola-Kirchhoff stress tensor is defined as

$$\boldsymbol{P} = J\boldsymbol{\sigma}\boldsymbol{F}^{-T}. \tag{3.26}$$

The second Piola-Kirchhoff stress tensor $\boldsymbol{S}$ is another important stress measure. It is a symmetric tensor that relates forces and areas within the reference configuration, providing a consistent stress description in the reference configuration. It is defined as

$$\boldsymbol{S} = \boldsymbol{F}^{-1}\boldsymbol{P}. \tag{3.27}$$

The second Piola-Kirchhoff stress is particularly useful in constitutive models of hyperelastic materials with a strain energy density function defined in the undeformed reference state.

Another key stress measure is the Kirchhoff stress tensor $\boldsymbol{\tau}$, which is connected to the Cauchy stress tensor through the Jacobian of the deformation gradient and is given by

$$\boldsymbol{\tau} = J\boldsymbol{\sigma}. \tag{3.28}$$

The Kirchhoff stress tensor is particularly relevant in plasticity and especially in scenarios where significant volume changes occur.

3.4.2 Terzaghi decomposition

In porous media theory, the interstitial fluid within the pores significantly influences the mechanical behavior of the material. To account for this, we introduce the concept of effective stress, often referred to as Terzaghi decomposition. Effective stress separates the total stress into contributions from the solid skeleton and the pore fluid pressure. The relationship is expressed as follows:

$$\boldsymbol{\sigma} = \boldsymbol{\sigma}' - p\boldsymbol{I}, \tag{3.29}$$

where $\boldsymbol{\sigma}'$ denotes the effective stress. The deformation of the skeleton is now determined by the effective stress $\boldsymbol{\sigma}'$.

To model the mechanical behavior of the porous skeleton under the influence of effective stress, we define the following constitutive relations

$$\boldsymbol{S} = \boldsymbol{S}' - pJ\boldsymbol{C}^{-1}, \tag{3.30a}$$

$$\boldsymbol{S}' = \frac{\partial \Psi^s(\boldsymbol{E}, J^s)}{\partial \boldsymbol{E}}, \tag{3.30b}$$

$$p = -\frac{\partial \Psi^s(\boldsymbol{E}, J^s)}{\partial J^s}, \tag{3.30c}$$

where $\Psi^s = \Psi^s(\boldsymbol{E}, J^s)$ is the Helmholtz free energy density and $J^s = J(1-\phi)$ the Jacobian weighted by the volume fraction of the skeleton phase [134]. The first constitutive equation defines the second Piola-Kirchhoff stress tensor $\boldsymbol{S}$ as a function of the strain energy potential Ψ^s and incorporates the influence of pore fluid pressure. The last equation relates the pore pressure p to the derivative of the strain energy potential with respect to the weighted Jacobian J^s.

These constitutive relations are derived from thermodynamic principles, ensuring that the mechanical behavior of the porous medium is consistent with the laws of thermodynamics. They provide a macroscopic description of poroelasticity, linking the stress and deformation of the solid skeleton with the fluid pressure within the pores.

For a more detailed examination of poroelasticity from a microscopic perspective, including the derivation of constitutive relations through a micro-macro approach, we refer to [135]. This approach provides insight into how the microscopic interactions and properties of the porous medium influence its macroscopic mechanical behavior.

3.4.3 Helmholtz free energy

To complete the system of equations governing the behavior of the porous medium, it is essential to specify the Helmholtz free energy function. We choose to work with a free energy that decomposes as

$$\Psi^s(\boldsymbol{E}, J^s) = \Psi^{\text{skel}}(\boldsymbol{E}) + \Psi^{\text{vol}}(J^s), \tag{3.31}$$

where $\Psi^{\text{skel}}(\boldsymbol{E})$ is the hyperelastic potential of the skeleton and $\Psi^{\text{vol}}(\boldsymbol{E})$ accounts for macroscopic volume change due to interstitial fluid pressure. For the skeleton's hyperelastic potential, a Neo-Hookean material model is employed. This model is expressed in terms of the first and third invariants of the right Cauchy-Green tensor:

$$\Psi^{\text{skel}} = \frac{1}{8}\lambda \ln^2(I_3) + \frac{1}{2}\mu[I_1 - 3 - \ln(I_3)], \tag{3.32}$$

where $I_1 = \text{tr}\,\boldsymbol{C}$ and $I_3 = \det \boldsymbol{C}$ are the first and third invariants, respectively. The coefficients λ and μ describe the Lamé parameters. For the volumetric contribution of the free energy function, we choose

$$\Psi^{\text{vol}} = \kappa\left(\frac{J^s}{1-\phi_0} - 1 - \ln\left(\frac{J^s}{1-\phi_0}\right)\right), \tag{3.33}$$

where $\kappa = E/(3(1-2\nu))$ is the bulk modulus of the skeleton, E is the Young's modulus, ν is the Poisson's ratio, and ϕ_0 is the initial porosity [134]. With that choice, the constitutive equations can be rewritten as

$$\boldsymbol{S} = 2\frac{\partial \Psi^{\text{skel}}}{\partial \boldsymbol{C}} - pJ\boldsymbol{C}^{-1}, \tag{3.34}$$

$$p = -\frac{\partial \Psi^{\text{vol}}}{\partial J^s}. \tag{3.35}$$

Equation (3.35) relates J^s to p, and thus the porosity ϕ to the fluid pressure p. Inserting (3.33) into (3.35) we obtain

By substituting the expression for Ψ^{vol} (3.33) into the constitutive relation for the fluid pressure (3.35), we obtain

$$p = \kappa \left(-\frac{1}{1-\phi_0} + \frac{1}{J^s} \right). \tag{3.36}$$

This equation links the fluid pressure p to the Jacobian of the solid phase J^s, highlighting the dependency of fluid pressure on the porosity and volume change of the skeleton.

3.5 System of equations

In summary, the poroelastic model is given by the following system of equations in the reference configuration Ω_0:

$$\nabla_0 \cdot (\boldsymbol{F}\boldsymbol{S}) = \boldsymbol{0} \qquad \text{in } \Omega_0, \tag{3.37a}$$

$$-K \left(\boldsymbol{F}^{-T} \nabla_0 \right) \boldsymbol{F}^{-T} \nabla_0 p = \theta \qquad \text{in } \Omega_0, \tag{3.37b}$$

$$\boldsymbol{S} = 2 \frac{\partial \Psi^{\text{skel}}}{\partial \boldsymbol{C}} - pJ\boldsymbol{C}^{-1}, \tag{3.37c}$$

$$p = -\frac{\partial \Psi^{\text{vol}}}{\partial J^s}, \tag{3.37d}$$

where the displacement $\boldsymbol{u}$ and the fluid pressure p are the two primary variables. The system needs to be complemented with suitable boundary conditions. We will specify these in Section 5.

4 Discrete vascular tree model

Modeling the poroelastic response of liver tissue with its corresponding perfusion model necessitates a detailed description of the vascular trees inside the liver. Since in-vivo imaging methods are limited in resolution, we generate these trees synthetically. The tree generation framework is published in the work of Jessen et al. [14]–[16]. In this thesis, the tree framework is used and integrated into the overall model. Therefore, in this section, we will provide a summary of the tree framework and describe the model assumptions and generation of vascular trees based on a set of physiological constraints.

4.1 Constrained constructive optimization

The best-known generation method for discrete vascular trees is constrained constructive optimization (CCO) [5], [6]. Therefore, we first describe CCO in more detail and illustrate its key properties. Its core is a local optimization approach, directly based on Murray's minimization principles [10]. The key principle of CCO lies in constructing a vascular tree by progressively adding segments, one at a time. Each segment is attached at the optimal location in the tree, with its bifurcation geometry adjusted to maximize the efficiency of blood flow and distribution. Once a new segment is added, the entire tree undergoes a rescaling process to ensure that boundary conditions, including terminal pressure and flow, are consistent. The generation of vascular trees consists of three key steps (see Fig. 4.1):

1. Terminal point sampling: The method begins by generating a new terminal point within the perfusion region, making sure it is adequately spaced from the existing tree segments according to a predetermined threshold, thus maintaining compatibility with the tree's structure and ensuring a balanced distribution of terminal points. As more segments are added, the threshold is decreased to adapt to the growing complexity of the tree.

2. Connection to existing tree: The sampled terminal point is attached to an existing segment, resulting in the formation of a new bifurcation. To reduce computational complexity, the process evaluates only a limited selection of nearby segments.

3. Optimization and rescaling: To minimize the overall volume of the tree, the newly created bifurcation point undergoes geometric optimization. The tree's segments are rescaled after each connection to compensate for changes in hydrodynamic resistance, ensuring that boundary conditions remain consistent. The rescaling involves a recursive process that fine-tunes the radii from the new terminal segment back to the tree's root.

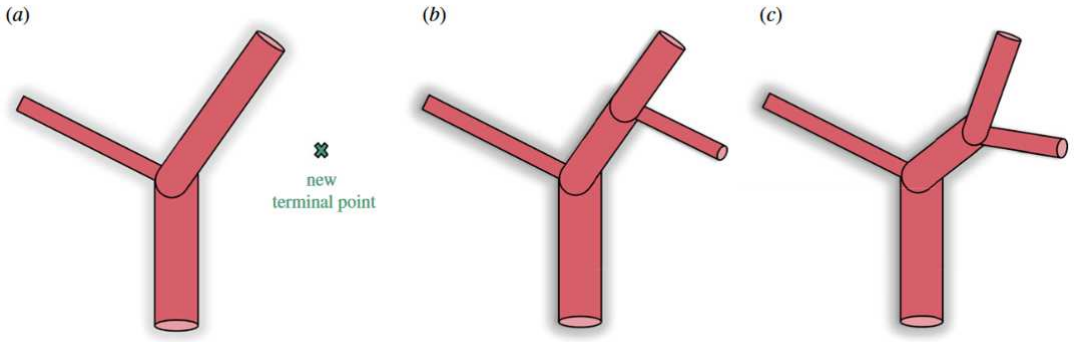

Figure 4.1: Key steps of tree generation with CCO [14]. (a) Terminal point sampling, (b) Connection to existing tree, (c) Optimization of new bifurcation.

CCO, while effective in generating vascular trees, has several limitations that impact its overall performance and applicability:

1. Local optimization: CCO aims to optimize segment connections locally which may result in tree structures that are not globally optimal. Therefore, this localized approach may not always result in the most effective overall tree arrangement.

2. Limited flexibility: The inability to produce asymmetric bifurcations, often seen in natural vascular systems, poses a challenge for the method, restricting CCO's ability to faithfully reproduce the complexity and variety of real vascular networks. Another major drawback of CCO is its limited ability to integrate specific geometric boundary conditions into the optimization process. For example, when creating multiple vascular trees, it is essential to prevent vessel intersections.

3. Sample dependence: The final tree's structure is heavily influenced by the sequence of terminal point sampling and connection. This dependence on the sampling sequence introduces variability in the tree structure results, making them sensitive to initial conditions and random seeds.

4. Computational complexity: The iterative optimization and rescaling processes become more computationally demanding as the vascular tree grows. Consequently, the method may prove impractical for modeling more extensive and complex vascular structures.

In the following section, we present our approach to addressing and overcoming the limitations of CCO.

4.2 Discrete non-intersecting vascular trees for blood supply and drainage

The generation framework is based on previous work of Jessen et al. [14], [15], which recently was extended to generate multiple non-intersecting trees inside the same perfusion domain [16]. In the following, we review and summarize the mathematical formulation and algorithmic framework.

4.2.1 Mathematical formulation

A discrete vascular tree is represented as a directed graph $\mathbb{T} = (\mathbb{V}, \mathbb{A})$ with nodes $u \in \mathbb{V}$ and segments $a \in \mathbb{A}$. Each segment $a = uv$ of $\mathbb{A}$ is defined by the geometric locations of its proximal and distal node x_u and x_v, its length $\ell_a = \|x_u - x_v\|$, volumetric flow $\hat{Q}_a$ and radius r_a. Thus, a *vessel* is simplified to a rigid and straight cylindrical tube. A tree has a single *root* node 0 and (multiple) *leaves* $v \in \mathbb{L}$, which are the distal nodes of terminal segments. The blood flow through the tree is assumed to be laminar with blood simplified to an incompressible, homogeneous Newtonian fluid. The pressure drop over a segment is described by Poiseuille's law with

$$\Delta p_a = R_a \hat{Q}_a \quad \forall a \in \mathbb{A}, \tag{4.1}$$

where the hydrodynamic resistance R_a of each segment a is

$$R_a = \frac{8\eta}{\pi} \frac{\ell_a}{r_a^4} \quad \forall a \in \mathbb{A}. \tag{4.2}$$

We set the dynamic blood viscosity η to a (constant) value of 3.6 cP and further assume a homogeneous flow distribution of our (given) root flow $\hat{Q}_{\text{perf}}$ to all N leaves, leading to the terminal flow $\hat{Q}_{\text{term}} = \hat{Q}_{\text{perf}}/N$. At intermediate branching nodes, the flow can be computed using Kirchhoff's law with

$$\hat{Q}_{uv} = \sum_{vw \in \mathbb{A}} \hat{Q}_{vw} \quad \forall v \in \mathbb{V} \setminus (0 \cup \mathbb{L}). \tag{4.3}$$

We note that complex viscosity laws and different flow distributions can also be incorporated into the framework, see [15].

The tree can be generated to obey various goal functions and constraints, as described in [15]. Here, we choose to minimize the total power of the tree, which consists of the power to maintain blood inside the vessels P_{vol} and the (viscous) power to move blood through vessels P_{vis}. The cost function for the vascular tree thus becomes

$$f_{\mathbb{T}} = P_{\text{vol}} + P_{\text{vis}} = \sum_{a \in \mathbb{A}} m_b \pi \ell_a r_a^2 + \frac{8\eta}{\pi} \frac{\ell_a}{r_a^4} \hat{Q}_a^2, \tag{4.4}$$

where m_b is the metabolic demand factor of blood, which we set to $0.6\,\mu\text{W}\,\text{mm}^{-3}$. Since

we pre-compute all flow values using (4.3), we can rewrite (4.4) to

$$f_{\mathbb{T}} = \sum_{a \in \mathbb{A}} w_a \ell_a, \tag{4.5}$$

where weight w_a is defined for each segment a with

$$w_a = m_b \pi r_a^2 + \frac{8\eta}{\pi r_a^4} \hat{Q}_a^2. \tag{4.6}$$

Our formulation does not include global constraints between nodes and each summand in (4.5) is decoupled. As shown in [16], the (optimal) radius of each segment a can then be independently computed with

$$r_a = \sqrt[6]{\frac{16\eta}{m_b \pi^2}} \sqrt[3]{\hat{Q}_a}. \tag{4.7}$$

The problem of finding the optimal geometry of a tree now only consists of finding the optimal nodal positions x and corresponding lengths ℓ.

For the liver, we combine the hepatic artery and portal vein into a single supplying tree, as their vessels are mostly aligned after a few generations, see [49]. Our goal is to generate one supplying tree (hepatic artery and portal vein) and one draining tree (hepatic vein), which do not intersect and are optimal both in topology and geometry regarding (4.5). We achieve the optimality requirement for the geometry of a single tree by optimizing the global geometry (position of all branch nodes) using a nonlinear optimization problem (NLP) [137], [138]. We include the nodal positions x and the lengths ℓ of all segments inside the vector of optimization variables $y = (x, \ell)$. With physical lower bounds ℓ^- and numerical upper bounds ℓ^+, the best geometry is found in

$$Y = \mathbb{R}^{3|\mathbb{V}|} \times [\ell^-, \ell^+]^{\mathbb{A}}, \tag{4.8}$$

and our NLP reads:

$$\min_{y \in Y} \quad \sum_{a \in \mathbb{A}} w_a \ell_a, \tag{4.9}$$

$$\text{s.t.} \quad 0 = x_u - \bar{x}_u, \qquad u \in \mathbb{V}_0 \cup \mathbb{L}, \tag{4.10}$$

$$0 = \ell_{uv}^2 - ||x_u - x_v||^2, \qquad uv \in \mathbb{A}. \tag{4.11}$$

where (4.10) fixes the position of terminal nodes and (4.11) ensures consistency between nodal positions and segment lengths.

To ensure that our supplying tree $\mathbb{T}^1$ and draining tree $\mathbb{T}^2$ do not intersect, we need to introduce coupling constraints between both trees. As described in [16], this involves two main steps. The first step is to introduce a set of (virtual) connections $\mathbb{A}^{12}$ between

neighboring nodes of both trees, defined by

$$\mathbb{A}^{12} = \{(v_1, v_2) |\ \ v_1 \in \mathbb{V}^1,\ v_2 \in \mathbb{V}^2,\ \|x_{v_1} - x_{v_2}\| < 1.25(r_{u_1 v_1} + r_{u_2 v_2})\}. \tag{4.12}$$

The second step is to introduce a set of *excursion nodes* $\mathbb{E}$, which includes all nodes with exactly one proximal and one distal node. These nodes are added to each set of intersecting vessels, which is described in more detail in [16]. Consequently, the set of optimization variables $y^{12} = (y^1, y^2)$ now consists of both trees and the best geometry is found in

$$Y^{12} = Y^1 \times Y^2 \times \mathbb{A}^{12}. \tag{4.13}$$

Our extended NLP then reads

$$\min_{y^{12} \in Y^{12}} \quad \sum_{i=1}^{2} \sum_{a_i \in \mathbb{A}^i} \ell_{a_i} w_{a_i} \tag{4.14}$$

$$\text{s.t.} \quad 0 = x_{u_1} - \_x_{u_1}, \qquad u_1 \in \mathbb{V}_0^1 \cup \mathbb{L}^1 \tag{4.15}$$

$$0 = x_{u_2} - \_x_{u_2}, \qquad u_2 \in \mathbb{V}_0^2 \cup \mathbb{L}^2 \tag{4.16}$$

$$0 = \ell_{u_1 v_1}^2 - \|x_{u_1} - x_{v_1}\|^2, \qquad u_1 v_1 \in \mathbb{A}^1 \tag{4.17}$$

$$0 = \ell_{u_2 v_2}^2 - \|x_{u_2} - x_{v_2}\|^2, \qquad u_2 v_2 \in \mathbb{A}^2 \tag{4.18}$$

$$0 = \ell_{v_1 v_2}^2 - \|x_{v_1} - x_{v_2}\|^2, \qquad v_1 v_2 \in \mathbb{A}^{12} \tag{4.19}$$

$$\ell_{v_1 v_2} > (r_{u_1 v_1} + r_{u_2 v_2}) + \epsilon, \qquad v_1 v_2 \in \mathbb{A}^{12} \tag{4.20}$$

$$\ell_{u_1 v_1} > \_\ell_{u_1 v_1}, \qquad v_1 \in \mathbb{E}^1 \tag{4.21}$$

$$\ell_{v_1 w_1} > \_\ell_{v_1 w_1}, \qquad v_1 \in \mathbb{E}^1 \tag{4.22}$$

$$\ell_{u_2 v_2} > \_\ell_{u_2 v_2}, \qquad v_2 \in \mathbb{E}^2 \tag{4.23}$$

$$\ell_{v_2 w_2} > \_\ell_{v_2 w_2}, \qquad v_2 \in \mathbb{E}^2. \tag{4.24}$$

Here, (4.19) and (4.20) ensure that the distance between two nodes (of trees 1 and 2) is at least their vessel radii plus a threshold ϵ. By using (4.21)-(4.24), we prohibit excursion nodes from moving along the path between their proximal and distal nodes. After the extended NLP is solved, both trees are checked for intersections. New excursion nodes are subsequently created at newly identified intersections. The process of adding excursions and solving the extended NLP is repeated until no further intersections are found.

4.2.2 Algorithmic framework and computer implementation

We use the framework described in [14], [16] to generate each tree with a (locally) optimal topology. First, we sample N terminal nodes $\bar{x}$ for each tree inside the (non-convex) perfusion volume (liver) and connect them to the manually set root positions. From these initial (fan) shapes, new topologies are explored by swapping segments. Each

swap changes the parent nodes between a sampled pair of nodes. The new topology is accepted based on a Simulated Annealing approach with probability

$$P = \exp\left\{\left(\frac{-\Delta f_{\mathbb{T}}}{T}\right)\right\}. \tag{4.25}$$

$\Delta f_{\mathbb{T}}$ is the change in cost induced by the swap and T is the SA temperature, which is decreased ('cooled down') after each iteration. After a fixed number of swaps, the global geometry is optimized and intersections are resolved as previously explained.

With both trees generated, we fix all nodal positions and prescribe a constant pressure drop Δp between all terminal nodes and the root node for each tree, respectively. For each segment a, we can now retrieve the length ℓ_a, the radius r_a, and the volumetric flow $\hat{Q}_a$. Further parameters such as the mean blood velocity $\bar{v}_a = \frac{\hat{Q}_a}{\pi r_a^2}$ can now be computed for each segment.

For illustration purposes, we consider a simple two-dimensional circular domain with a radius of 10 mm, where we specify one root and randomly distributed terminal points for the supplying and draining trees. The specific numbers and parameters are listed in Table 4.1. Figure 4.2 illustrates the resulting supplying and draining tree in the circular domain. We observe that although both sets of terminal points are located within the plane of the circular domain, the two trees are not intersecting each other, using the third dimension to let their vessels move around each other.

Table 4.1: Characteristic numbers and parameters of the discrete vessel network based on Poiseuille flow for the simple example of a 2D circular domain.

	N_{vessel}	N_{term}	p_{root} $[\frac{\text{kg}}{\text{mm s}}]$	$\hat{Q}_{\text{perf}}$ $[\frac{\text{mm}^3}{\text{s}}]$
Supplying tree	43,981	21,991	0.4	80.0
Draining tree	43,857	21,929	0.0	80.0

4.2.3 Validation

To determine if synthetically generated vascular trees accurately represent real biological structures, it is essential to validate them against real data. Non-invasive imaging techniques, particularly CT and MRI, are essential tools for obtaining in vivo (within a living organism) patient-specific vascular data. Despite significant technological advancements in the past decades, the resolution of these imaging techniques remains insufficient for visualizing the tree structures down to the smallest blood vessels, such as arterioles and venules.

For a more thorough examination of vascular structures down to the smallest vessels, ex vivo (outside a living organism) methods are necessary. These techniques, though highly effective, are often labor-intensive, require specialized equipment, and can be costly. For instance, examining an ex vivo liver tree structure requires connecting it to

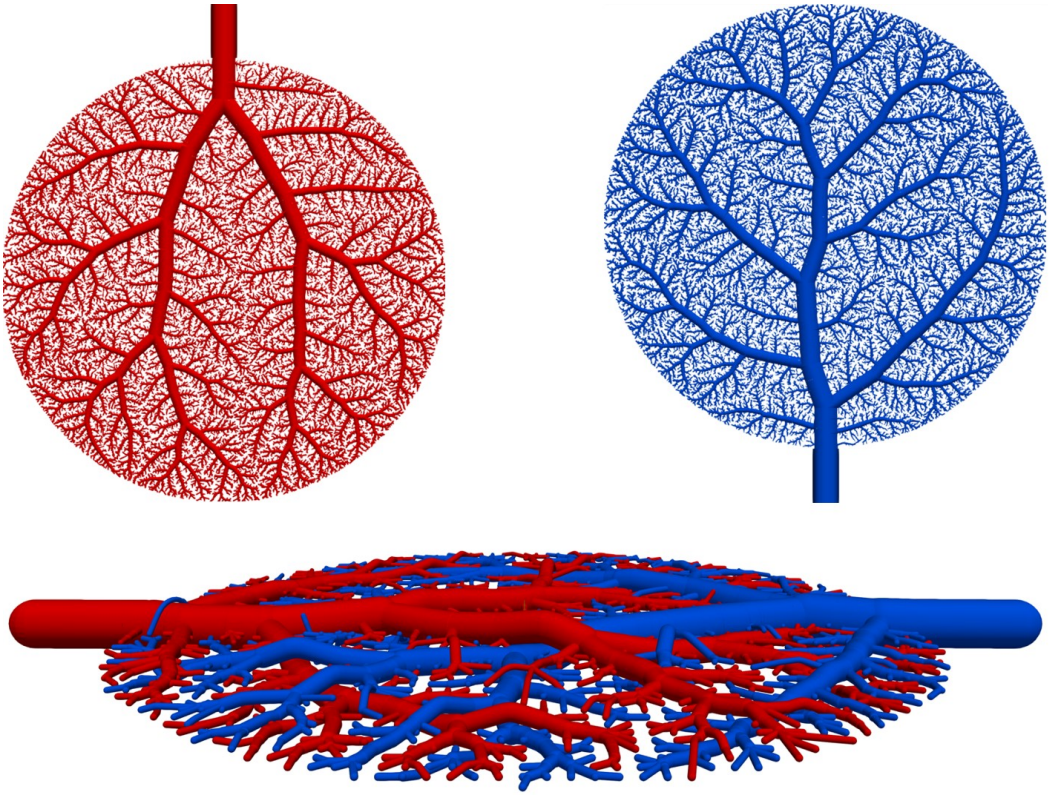

Figure 4.2: Synthetic vascular trees for the two-dimensional benchmark problem. Supplying vascular tree on the left and draining vascular tree on the right. The bottom figure highlights how both trees are not intersecting each other.

a machine perfusion system to maintain the vascular network.

One notable ex vivo technique for obtaining vascular data is vascular corrosion casting (see Fig. 4.3). This approach involves filling the blood vessels with resin, which solidifies to create a cast of the vascular network [76]. Initially, blood is drained from the vessels to prevent clotting-related blockages. Once the vessels are empty, the vessels are filled with resin, and clamps are applied to the inlet and outlet vessels to prevent leakage. The resin then cures for approximately two hours, creating a solid plastic replica of the vascular system.

The next step involves dissolving the surrounding tissue with a corrosive chemical bath, which usually takes approximately two days. The corrosion process is designed to affect only the tissue, while preserving the resin. Additionally, incorporating contrast agents into the resin allows for differentiation between arterial and venous vessels. The final cast provides a three-dimensional representation of the blood vessels down to 0.5 mm, which can subsequently be scanned using a high-resolution micro-CT scanner.

In Fig. 4.4, we present the synthetically generated full portal and hepatic vein trees with the generation method presented in 4.2, while Fig. 4.5 and Fig. 4.6 display the pruned versions of these trees alongside the corresponding ones obtained from the corro-

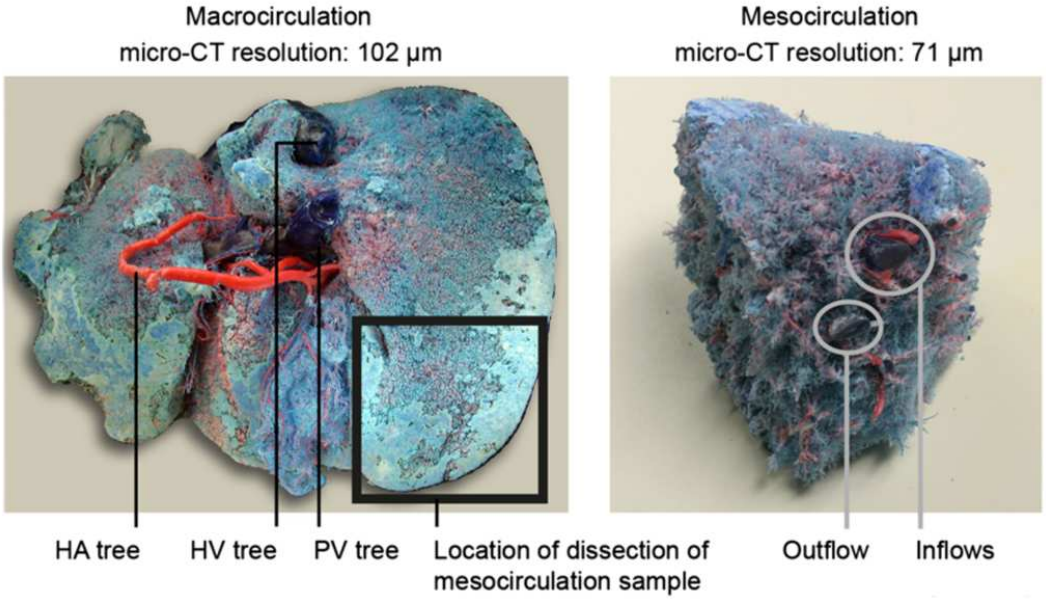

Figure 4.3: Vascular corrosion cast of the full human liver and a mesocirculation sample [76].

sion cast. When comparing the results from generated vascular trees with those obtained experimentally, one can see that both types of trees exhibit not only bifurcations but also trifurcations. Qualitatively, the synthetic trees are in good agreement with the experimental data, confirming their realistic representation.

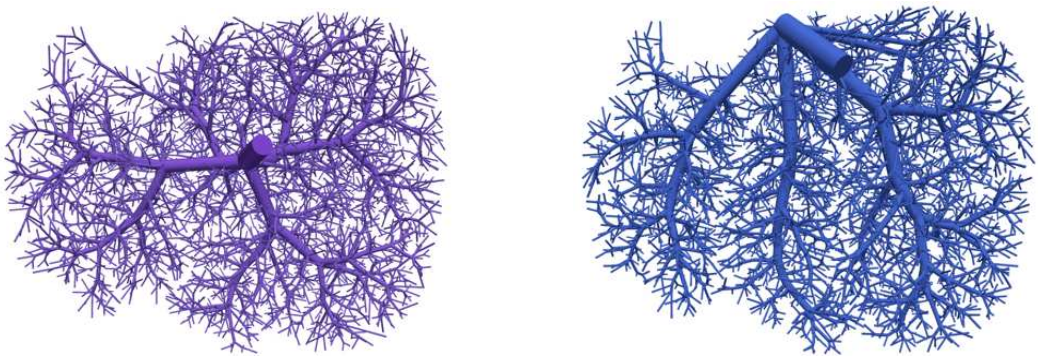

(a) Portal vein

(b) Hepatic vein

Figure 4.4: Synthetically generated trees (full).

4.2.4 Improved framework for generating synthetic vasculature

Compared to existing methods like CCO, the improved framework for generating synthetic vascular trees offers several advantages:

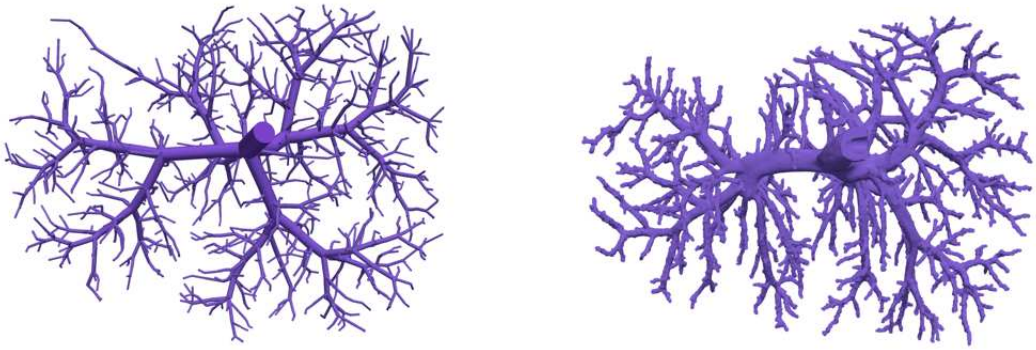

(a) Synthetic tree (b) Corrosion cast

Figure 4.5: Synthetically generated portal vein (pruned) versus corrosion cast tree as obtained in [76].

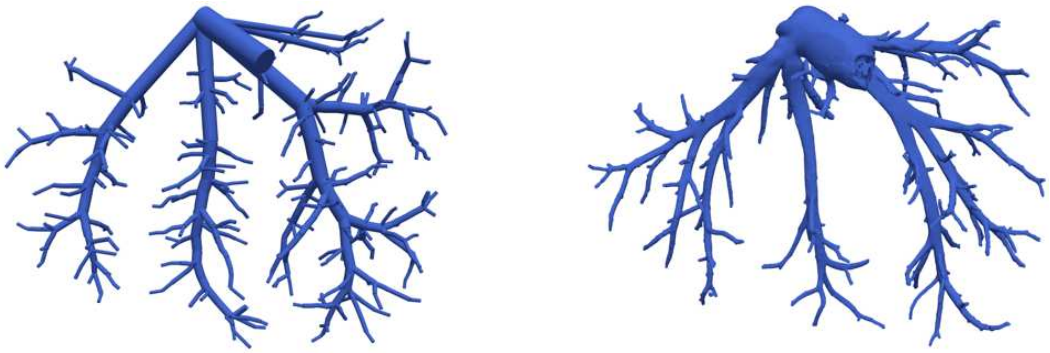

(a) Synthetic tree (b) Corrosion cast

Figure 4.6: Synthetically generated hepatic vein (pruned) versus corrosion cast tree as obtained in [76].

- Global geometry and topology optimization: Unlike CCO, which primarily focuses on local optimization, this improved framework optimizes the entire vascular tree's geometry and topology on a global scale. This leads to more efficient and realistic tree structures.
- Repeatable results: By reducing variability linked to different random seeds or sampling orders, the new framework produces more consistent and repeatable results, overcoming a significant limitation of CCO.
- Enhanced computational efficiency: The refined computational approach of the new framework decreases the time and complexity of vascular tree generation, improving its feasibility for modeling larger and more sophisticated structures.
- Multiple trees in non-convex volumes: The method allows for the generation of multiple vascular trees in non-convex volumes, accommodating complex anatomical features and enhancing the precision of modeling interconnected vascular net-

works.

- Investigation of complex phenomena: The framework enables the investigation of more complex physiological and pathological phenomena, offering deeper insights into the development and functioning of vascular systems across different scenarios.
- Incorporation of physiological constraints: The framework integrates physiological constraints effectively and can account for the varying properties of blood flow through vessels, such as changing viscosity, which is critical for accurate simulations.
- Scalability for large-scale simulations: The framework is suitable for the generation of large and complex vascular networks without significant loss of accuracy or computational feasibility. This scalability is particularly important for simulations that require modeling the entire circulatory system, making it useful for a wide range of research and clinical applications.
- Versatility across different biological systems: The framework's flexibility supports its application to a wide range of vascular systems across different organs or species. Initially developed for human vascular networks, it can be modified to simulate the blood vessels of other animals or organs.
- Integration with imaging data: The framework can be seamlessly integrated with imaging data, such as MRI or CT scans, to create patient-specific vascular models, where it is also possible to incorporate patient-specific vessel data if and up to the resolution available. Such integration is crucial for patient-specific modeling, as it provides a detailed view of an individual's vascular structure, which enhances diagnostic and treatment strategies.

In summary, the improved framework for generating synthetic vasculatures represents a considerable advancement, offering greater accuracy, scalability, and flexibility for a broad spectrum of biomedical applications.

5 Connecting continuum poroelasticity with discrete synthetic vascular trees

In this section, we describe the coupling of the vessel trees to the poroelastic model derived in the previous sections. First, we describe the interaction of the poroelastic domain with surrounding tissues by nonlinear displacement boundary conditions. After, we introduce modeling assumptions in terms of source terms for the inlets and boundary conditions for the outlets to enable the perfusion of the poroelastic domain. We study numerical examples in 2D to demonstrate the behavior of our modeling framework based on the connection of the poroelastic model and the synthetic vascular trees. We close this section by providing results for the simulation of three-dimensional liver resection scenarios. The results shown in this section are published in [69].

5.1 Modeling the interaction with surrounding tissues

To arrive at a closed boundary value problem, we need to complement the system (3.37) by appropriate boundary conditions. In our case of application, we would like to take into account the interaction of the liver with surrounding organs, with which the liver is continuously in contact. Motivated by a penalty approach known from contact mechanics,

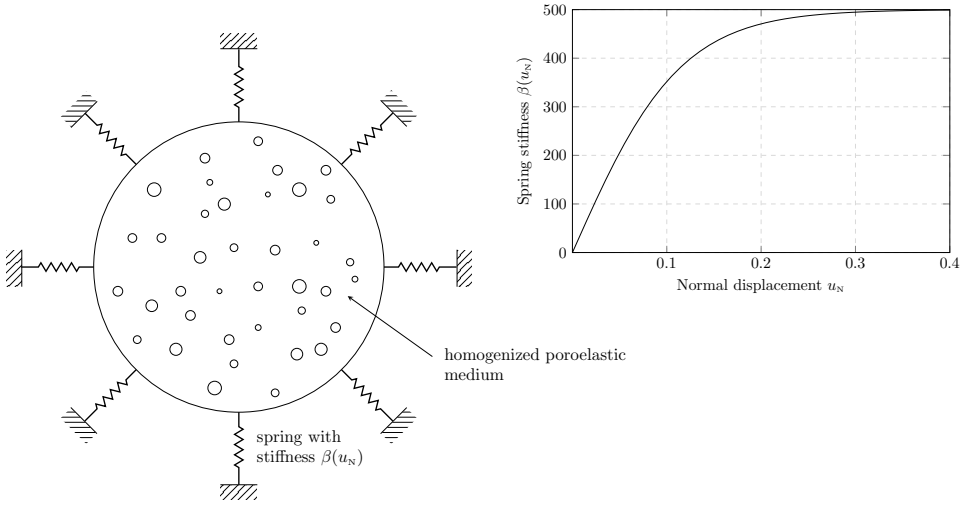

Figure 5.1: Modeling the resistance of surrounding tissues. The spring stiffness β is a function of the normal displacement u_N.

we model the resistance of the surrounding organs by adding the following contribution:

$$W_{\mathrm{c}}(u_{\mathrm{N}}) = \beta u_{\mathrm{N}}, \tag{5.1}$$

supported on Γ_{outer} to the left-hand side the balance of momentum. This term can be interpreted to mimic the effect of nonlinear springs at the outer boundary as illustrated in Fig. 5.1, where β corresponds to the spring stiffness. In hyperelastic tissue-like materials, the stiffness changes with the deformation. We therefore model β as a function of the boundary displacement u_{N} in the normal direction:

$$\beta(u_{\mathrm{N}}) = \frac{2\alpha}{1 + e^{-c\,u_{\mathrm{N}}/u_0}} - \alpha, \tag{5.2}$$

in which α corresponds to the maximum value of the spring stiffness and c is the steepness of the curve. The parameter $u_0 = 1$ mm is a non-dimensional reference displacement. We choose $c = 15$ for all computations. Analogous to nonlinear springs, the stiffness saturates towards a constant value with increasing displacement.

5.2 Augmenting the poroelastic model with discrete tree feature

The poroelastic domain, representing the tissue, is supplied with fluid from the vessels of a supplying tree and returns fluid through the vessels of a draining tree (see Fig. 5.2). Therefore, the poroelastic domain can be interpreted as a connector between the supplying and draining trees. We now address the question of how to connect the poroelastic model to the vessel trees by specifying appropriate boundary conditions to induce flow from the inlets to the outlets.

To bridge the gap between the macroscopic (homogenized) medium and the discretely resolved levels of the vascular tree, we assume circular areas (or spherical areas in 3D), whose radii are of the same order as the radii of the vessels at the terminal vessel points (see Fig. 5.2). We cannot model the physiological mechanisms in these areas directly, and therefore depict them as void. In the following, we describe corresponding modeling assumptions in terms of source terms for the inlets and boundary conditions for the outlets.

5.2.1 Bell-shaped source terms to model flow from the supplying tree

We induce flow from the discrete supplying tree into the poroelastic domain through the source quantity θ in the mass conservation equation (3.37b) by a summation over all n terminal vessels of the supplying tree:

$$\theta = \sum_{i=1}^{n} \theta_i, \tag{5.3}$$

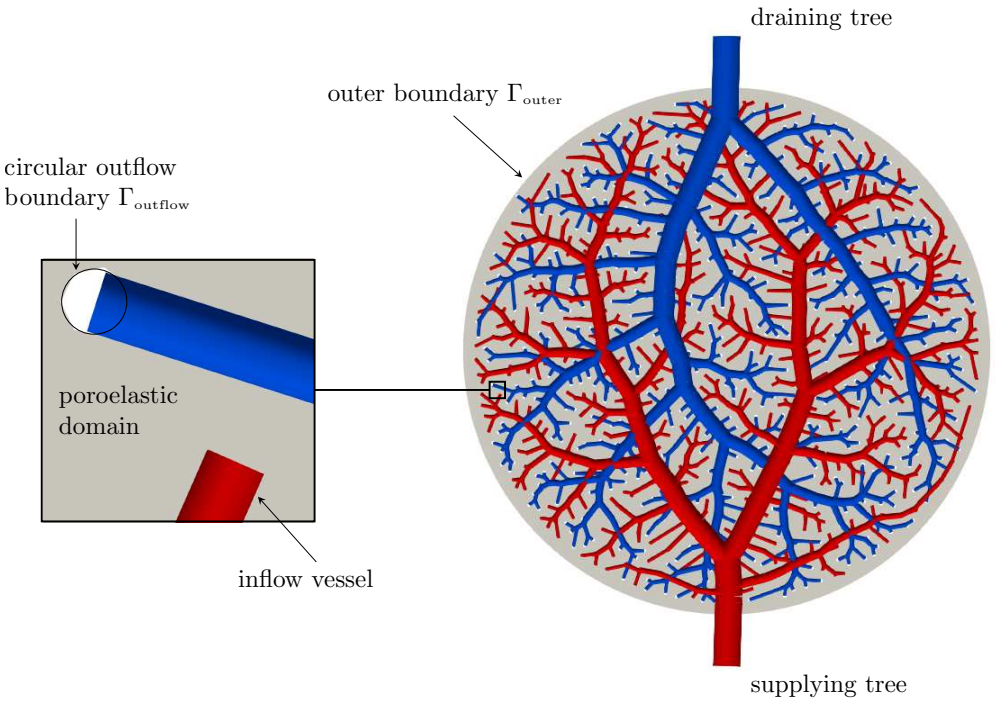

Figure 5.2: Coupling of the vascular trees with the porous medium. The red tree represents the vessels of the supplying tree while the blue ones are the vessels of the draining tree. Circular voids represent the interface area between the continuum model and the discrete draining tree.

where θ_i refers to the source term of the i-th terminal vessel of the supplying tree. We transfer the volumetric flow from each terminal vessel i of the supplying tree into the source term in the mass conservation equation (3.37b) in the form of a bell-shaped distribution:

$$\theta_i(\boldsymbol{x}) = \gamma_i \exp\left(\frac{-\|(\boldsymbol{x} - \boldsymbol{x}_i)\|_2^2}{(br_i)^2}\right), \tag{5.4}$$

where γ_i is the amplitude of the i-th function, $\|\cdot\|_2$ is the Euclidean norm, $\boldsymbol{x}_i$ is the position vector of the i-th inlet terminal point, r_i is the radius of the corresponding i-th inlet terminal vessel and b is a scaling factor of the radius. The radii r_i, the locations $\boldsymbol{x}_i$, and the volumetric flow $\hat{Q}_i = \int \theta_i \mathrm{d}\mathbf{x}$ are extracted from the supplying vascular tree data described in section 4.2. The assumption of a incompressible, steady-state setting implies that the inflow must match the outflow. Furthermore, drainage occurs exclusively through the terminal outlet vessels, and we have set an impermeable boundary condition along the outer boundary. Under these circumstances, we require that the total flow that enters the domain, $\sum_i \hat{Q}_i$, matches the total flow that leaves the draining tree.

The bell-shaped function possesses several advantages that justify this choice. The symmetric, smooth and continuous nature of the bell-shaped function distributes the

inflow, modeling the effect of the interface area that is not represented in the discrete and continuum models. It allows for a simple and effective control of the overall shape and magnitude of the inflow profile. The bell-shaped function also has a well-defined peak that represents the highest flow rate. Moreover, the bell-shaped function can be employed to simulate the spread of the fluid as it enters the domain. By adjusting the amplitude of the bell-shaped function, the magnitude of the inflow can be controlled. The bell-shaped function has a simple mathematical form and an analytical solution that allows for efficient and accurate computation in numerical simulations. In particular, the amplitude γ_i is determined from the known i-th volumetric flow $\hat{Q}_i$ via $\gamma_i = \hat{Q}_i/(\pi b^2 r_i^2)$ (two dimensions) and $\gamma_i = \hat{Q}_i/((\pi b^2 r_i^2)^{\frac{3}{2}})$ (three dimensions).

5.2.2 Boundary conditions to model flow into the draining tree

We induce flow from the poroelastic domain into the discrete draining tree by imposing Dirichlet boundary conditions for the pressure at the circular boundaries of these void areas (denoted by Γ_{outflow}). The radii and locations of the terminal outlet points are extracted from the draining vascular tree data described in section 4.2. It is convenient to set a reference pressure level of $p = 0$ here. To guarantee the conservation of mass, we model the outer boundary (denoted by Γ_{outer}) of the domain as impermeable by inducing the Neumann boundary condition

$$\nabla p \cdot \mathbf{n} = 0, \tag{5.5}$$

which guarantees that no fluid is leaving the poroelastic domain through its outer boundary.

5.3 Numerical examples in 2D

To illustrate the functionality of our modeling framework, we start with two-dimensional numerical examples. This framework combines the poroelastic model with synthetic vascular trees, allowing us to observe and analyze how they interact and influence each other.

5.3.1 Weak formulation and discretization

We utilize the standard finite element method [139] for the discretization of the poroelastic model in the Lagrangian description (3.37) augmented with the interaction term presented in section 5.1. Multiplication of the momentum equation (3.37a) with discrete test function $\boldsymbol{v}_h$ and the pressure equation (3.37b) with discrete test function q_h, and subsequently integrating over the reference domain Ω_0, and applying integration by parts leads to the weak statement: Find $\boldsymbol{u} \in \mathcal{V}_h$ and $p \in \mathcal{W}_{h,0}$ such that for all $\boldsymbol{v}_h \in \mathcal{V}_h$

and $q_h \in \mathcal{W}_{h,0}$:

$$\int_{\Omega_0} (\boldsymbol{F}\boldsymbol{S}) : \nabla_0 \boldsymbol{v}_h \, \mathrm{d}\Omega_0 + \int_{\Gamma_{\text{outer}}} \beta \, (\boldsymbol{u} \cdot \mathbf{N}) \, (\boldsymbol{v}_h \cdot \mathbf{N}) \, \mathrm{d}\Gamma_{\text{outer}} = \mathbf{0}, \tag{5.6}$$

$$\int_{\Omega_0} \left(K \mathbf{F}^{-T} \nabla_0 p\right) \cdot \left(\mathbf{F}^{-T} \nabla_0 q_h\right) \mathrm{d}\Omega_0 + \int_{\Gamma_{\text{outer}}} (K \nabla_0 p \cdot \mathbf{N}) \, q_h \, \mathrm{d}\Gamma_{\text{outer}} = \int_{\Omega_0} \theta q_h \, \mathrm{d}\Omega_0, \tag{5.7}$$

where $\mathbf{N}$ is the normal vector in the reference configuration. The discrete function spaces $\mathcal{V}_h$ and $\mathcal{W}_{h,0}$ consist of linear and quadratic Lagrange basis functions of degree $P = 1$ and $P = 2$, and are applied to discretize the displacements and the pressure, respectively [22]. Homogeneous Dirichlet boundary conditions on Γ_{outflow} are strongly enforced in $\mathcal{W}_{h,0}$:

$$\mathcal{W}_{h,0} = \{q_h \in \mathcal{W}_h : q_h = 0 \text{ on } \Gamma_{\text{outflow}}\}, \tag{5.8}$$

with $\mathcal{W}_h$ being the unrestricted function space for the pressure. We implemented the framework in FEniCS, where we utilized a standard Newton-Raphson method, the iterative solver GMRES and the preconditioner Hypre_Euclid [140].

Equation (3.37b), also referred to as the reduced Darcy formulation [22], is solely written in terms of pressure, as we have eliminated the velocity upon substituting (3.21) into (3.20). Not substituting (3.21) into (3.20) leads to a two-field formulation (velocity and pressure), also referred to as the full Darcy system in literature [22]. In that case, the poroelastic equations have a saddle point structure and the discrete pressure and velocity spaces must therefore satisfy the inf-sup condition [141], [142]. One stable combination of mixed finite element pairs is, for example, a Taylor-Hood element with a pressure approximation that is one order lower than the one for the velocity. Disadvantages of the full Darcy formulation are the increased number of degrees of freedom or the imposition of a condition on the normal velocity component of the boundary (impermeable domain). For a comparison of the full and reduced Darcy model in terms of solution time, memory requirements and accuracy we refer the interested reader to [22].

5.3.2 Poroelastic circular disk coupled to planar trees

We first consider a poroelastic circular domain that is perfused by a fluid provided by a planar supplying tree and returned into a planar draining tree (see also Fig. 5.2). Both trees consist of 1,000 terminal vessels. We emphasize that the objective of the two-dimensional simulations is to study the model behavior and its sensitivity with respect to model parameters. It is not intended to represent the liver tissue itself. The simplified geometry, with a limited number of terminal branches, serves as a computationally inexpensive starting point and permits examination of key aspects (inflow parameters, vessel tree depths, contact boundary conditions) without introducing further complexity. For the poroelastic disk, we choose the parameters in SI units summarized in Tab. 5.1. We have chosen standard values for the material parameters $E = 1 \text{ kg}/(\text{m}\,\text{s}^2)$ and $K = k/\nu = 1 \text{ kg}\,\text{m}/\text{s}$ and a simple geometry for the proof of concept. The purpose is

Table 5.1: Model parameters for the poroelastic disk.

Skeleton-related parameters	Flow-related parameters
Disk radius $r = 0.01$ m	Initial porosity $\phi_0 = 0.5$
Young's modulus $E = 1 \frac{\text{kg}}{\text{m s}^2}$	Permeability $k = 3.6 \cdot 10^{-3}\text{m}^2$
Poisson's ratio $\nu = 0.3$	Dynamic viscosity $\eta = 3.6 \cdot 10^{-3} \frac{\text{kg}}{\text{m s}}$
	Perfusion flow (at root) $\hat{Q}_{\text{perf}} = 80 \cdot 10^{-9} \frac{\text{m}^3}{\text{s}}$

to study the influence of the model parameters (inflow parameters, vessel tree depths and contact boundary condition) qualitatively. Modifying E and K changes the solution fields only quantitatively, no qualitatively. Instead of a spring-type condition, we fix the outer boundary for the moment, so that $\boldsymbol{u} = \mathbf{0}$ at the outer circular boundary. Each tree consists of 50 terminal vessels. For the bell-shaped source terms in (5.4), we choose $b = 3$.

We discretize the circular domain with a mesh of 36,826 triangular elements. We first obtain the solutions for the primary field variables $\boldsymbol{u}$ and p. With the pressure p known, we can compute the porosity field ϕ from (3.36) and the velocity from Darcy's law (3.21). The solution of the pressure p is depicted in Fig. 5.3. The white streamlines indicate the flow direction. One can observe higher pressure levels close to the inlet vessels. We also observe large pressure values in the area on the top near the boundary. These drive the fluid to an outlet further away. We note that these high pressure values are the result of an accumulation of inlet and the non-existence of outlet vessels in the area. The influence of the boundary effects is negligible in this regard. Increasing the number of outlet points would eliminate the high pressure values. The displacement solution $\boldsymbol{u}$ and the porosity field ϕ are plotted in Figs. 5.4a and 5.4b. Higher displacement values can be observed in the areas of high pressure values. The porosity field ϕ fluctuates around the initial porosity value of 0.5.

5.3.3 Model sensitivity with respect to bell-shaped source term

Figure 5.5 depicts the pressure field p for two different values of the scaling factor b of the bell-shaped function (5.4). In the case of $b = 1$ (see Fig. 5.5a), the resulting pressure values are centered on a smaller area. Therefore, the maximum values also exceed the ones obtained with $b = 3$ (see Fig. 5.5b). Nevertheless, global behavior is in both cases equivalent. For all further computations, we proceed with $b = 3$.

5.3.4 Model sensitivity with respect to stiffness of surrounding tissue

Figure 5.6 plots the displacement solution for a stiffer ($\alpha = 5 \cdot 10^2$) and softer resistance ($\alpha = 1 \cdot 10^1$) in equation (5.2). In the stiff case (see Fig. 5.6a), the displacement field is virtually indistinguishable from the solution with a fixed boundary depicted in Fig. 5.4a. In the soft case, the boundary can deform, leading to a significantly different displacement pattern, plotted in Fig. 5.6b. Due to the weakening of the constraint in

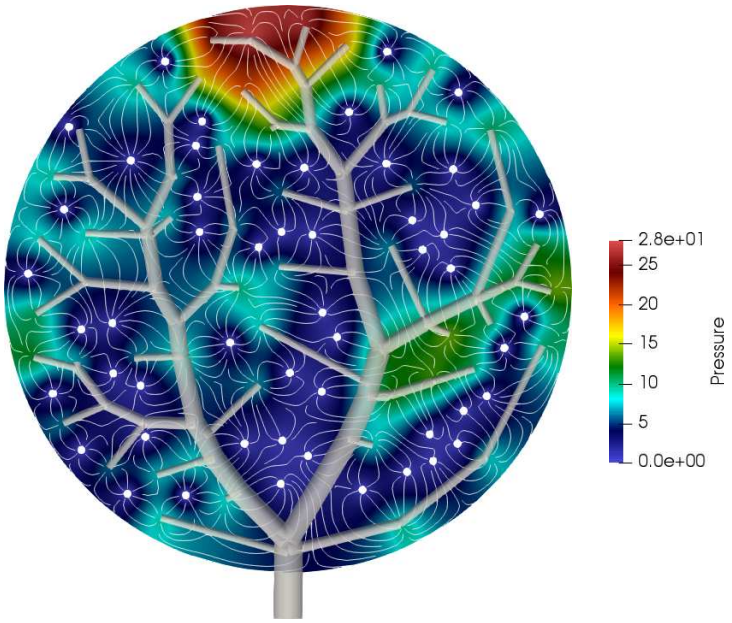

Figure 5.3: Solution for the pressure field p $[\frac{\mathrm{kg}}{\mathrm{m\,s^2}}]$. The depicted tree is the supplying tree. The streamlines illustrate the flow from the inlets to the outlets.

the soft case, the maximum displacement value decreases compared to the one in the stiff case.

5.3.5 Model sensitivity with respect to hierarchical tree depth

We finally investigate the model behavior at two different tree depths with 250 and 1,500 terminal vessels for both trees. In order to resolve the circular voids adequately, we refine the mesh with 114,320 elements in the former case to a mesh with 353,344 triangular elements in the latter case. The results of the pressure field p are presented in Fig. 5.7. It is evident that the pressure drop between inlets and outlets is smaller in the case of a finer tree hierarchy (see Fig. 5.7a and 5.7b). When the trees are resolved to a larger depth, the outlet and inlet points seem to be more homogeneously distributed from a global perspective, resulting in shorter distances between the inlet and outlet. Thus, global behavior leads to a pressure solution that shows a more fine-grained distribution. If we characterize a certain number of inlets or outlets with a representative volume element (RVE), we observe that the relative pattern of the solution with respect to such an RVE does not change. It is easy to verify from the plots that one can find similar patterns of the pressure field of the coarser tree in the pressure field of the finer tree.

The velocity field in Fig. 5.8 shows similar behavior as that of the pressure field. For the finer trees, the maximum flow resulting from the pressure fields decreases. Additionally, the relative pattern of the solution does not change when representing a certain number of inlets or outlets with an RVE. Both plots show similar patterns of flow fields with respect to such an RVE.

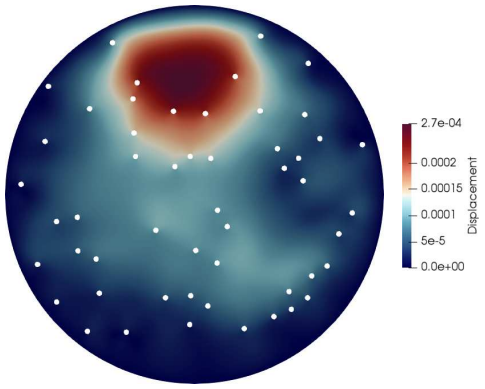

(a) Displacement u

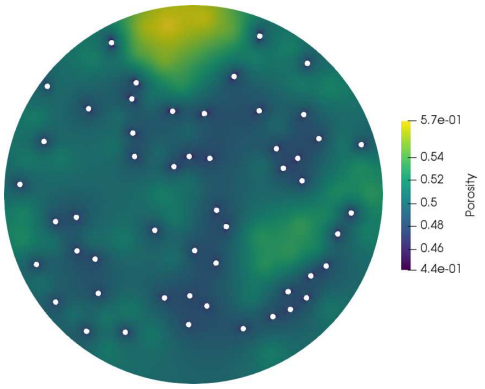

(b) Porosity ϕ

Figure 5.4: Solution for displacement field $\boldsymbol{u}$ [m] with a fixed outer boundary and solution for porosity field ϕ.

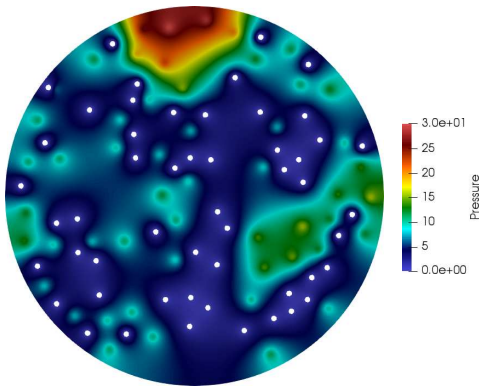

(a) Solution for $b = 1$

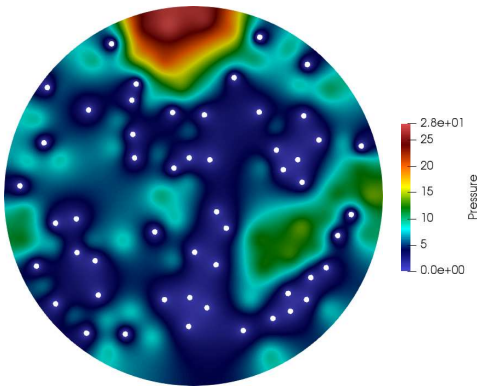

(b) Solution for $b = 3$

Figure 5.5: Solution for pressure field p $[\frac{\text{kg}}{\text{m s}^2}]$ with different scaling factors b of bell-shaped function.

5.4 Towards simulation based assessment of liver resection

Since the liver is characterized by a high degree of vascularization, the regeneration process of the liver is dependent on the perfusion and redistributed flow after resection, which affects important functions such as blood supply or metabolism [79]. In the following, we will employ our modeling framework to evaluate cut patterns and investigate blood flow redistribution after surgical resection.

5.4.1 Patient-specific liver geometry and discretely resolved vascularization

We generate a patient-specific liver model based on imaging data obtained from CT scans [143]. For the segmentation of the liver, we use the open source software package

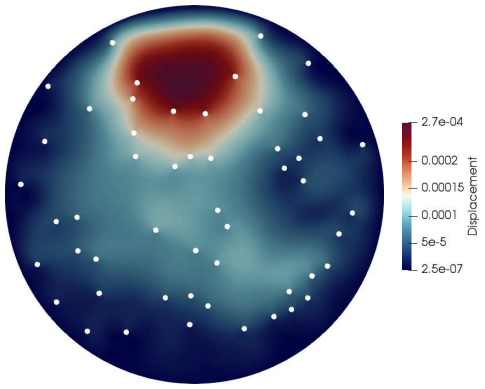

(a) Stiff contact with $\alpha = 5 \cdot 10^2$

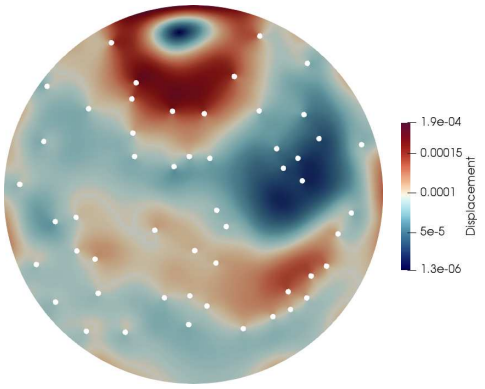

(b) Soft contact with $\alpha = 1 \cdot 10^1$

Figure 5.6: Solution for displacement field $\boldsymbol{u}$ [m] for different stiffness values in the contact boundary conditions.

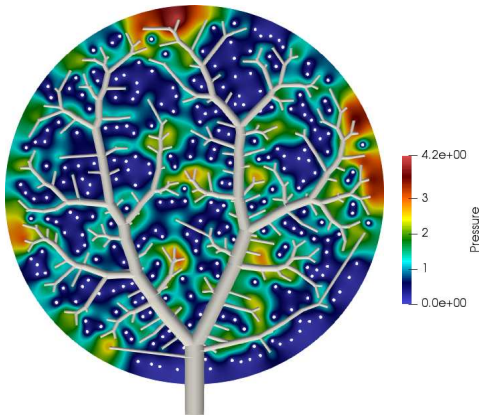

(a) Pressure p for 250 inlets/outlets

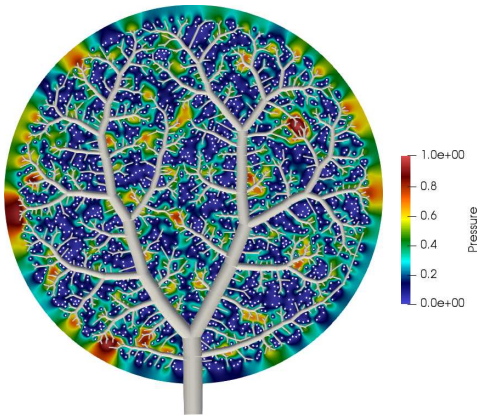

(b) Pressure p for 1500 inlets/outlets

Figure 5.7: Solution for pressure field p $[\frac{\text{kg}}{\text{m s}^2}]$ obtained with two different tree resolutions.

3D Slicer[4] and the free software Autodesk Meshmixer[5]. A 2D slice of the 3D voxel model and the segmentation mask of the liver domain (green colour) are shown in Figs. 5.9a. and 5.9b, respectively. The resolution of the CT scan is 0.977 x 0.977 mm within each image, with a spacing of 2.5 mm between the slices.

Figure 5.10 illustrates the segmented liver with the synthetic supplying tree (hepatic artery and portal vein) and the synthetic draining tree (hepatic vein). For both trees we choose 1,000 terminal vessels to model the flow of blood into the poroelastic domain in an accurate manner, while still maintaining computational efficiency. We note that we recently improved the efficiency of the vascular generation algorithm described in section 4.2, which allows us to generate full scale vascular trees with around 1,000,000

[4]https://www.slicer.org/
[5]https://meshmixer.com/

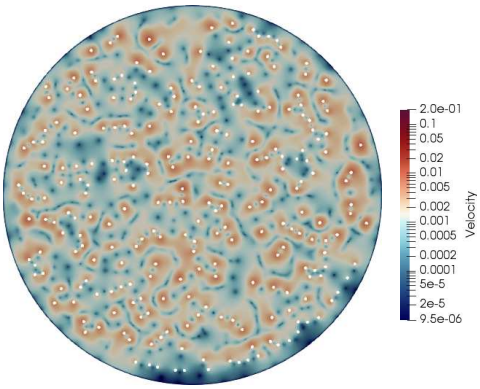

(a) Velocity w for 250 inlets/outlets

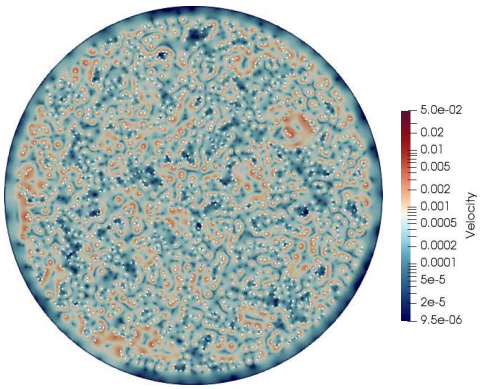

(b) Velocity w for 1500 inlets/outlets

Figure 5.8: Solution for velocity field w $[\frac{\mathrm{m}}{\mathrm{s}}]$ obtained with two different tree resolutions.

(a) 2D slice

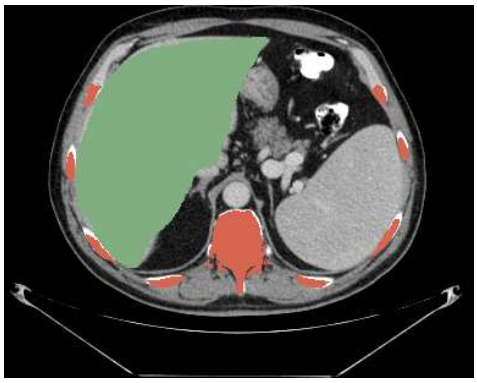

(b) Segmentation mask with liver in green

Figure 5.9: Abdominal CT scan containing the liver with a resolution of 0.977 x 0.977 mm and a slice thickness of 2.5 mm.

terminal vessels [15].

After creating the liver geometry, we assume spherical voids at the terminal points of the outlets where we impose zero pressure as a reference level. We then generate a mesh which contains 7,385,996 tetrahedral elements.

5.4.2 Anatomical vs. non-anatomical resection

Detecting areas with insufficient blood supply and locally quantifying the perfusion efficiency is helpful for the assessment of the post-operative outcome. We first show the results of the liver model before resection. The physiological parameters that have been used for all liver computations are listed in Tab. 5.2. The stiffness value $\alpha = 5 \cdot 10^3$ has been chosen based on the elastic properties of the surrounding organs [145]. The results for the velocity and pressure are depicted in Fig. 5.11 and Fig. 5.12. We will later see that the full liver model shows a more homogeneous blood supply to the liver

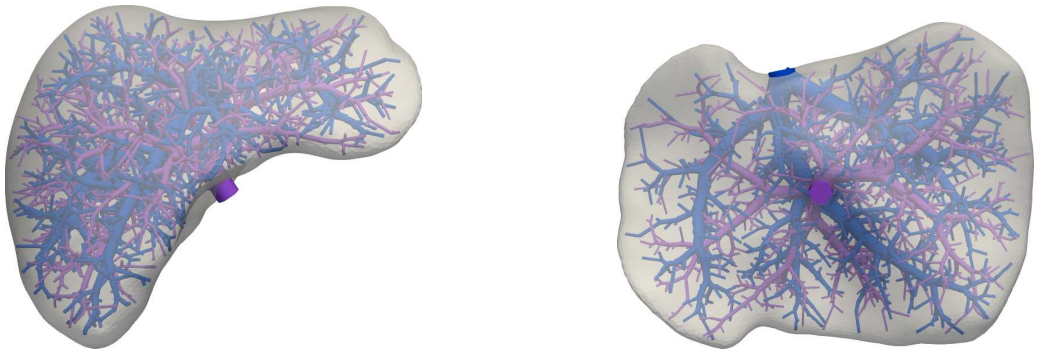

(a) Anterior view

(b) Inferior view

Figure 5.10: Patient-specific 3D liver model with the supplying (purple) and draining (blue) vascular tree structures.

Table 5.2: Simulation parameters for the liver problem [17], [49], [144].

Tissue deformation-related parameters	Perfusion-related parameters
Young's modulus $E = 5000\ \frac{\text{kg}}{\text{m s}^2}$	Initial porosity $\phi_0 = 0.15$
Poisson's ratio $\nu = 0.35$	Permeability $k = 2 \cdot 10^{-14}\ \text{m}^2$
	Dynamic viscosity $\eta = 3.6 \cdot 10^{-3}\ \frac{\text{kg}}{\text{m s}}$
	Inflow (at root) $\hat{Q}_{\text{perf}} = 20 \cdot 10^{-6}\ \frac{\text{m}^3}{\text{s}}$

tissue than the resected livers. We observe low disparities of the pressure field (see Fig. 5.12) on a global scale, and an area of pressure accumulation in the upper right part of the unresected liver. This is the consequence of (i) the modeling choices of the inflow and outflow, and (ii) the homogenization over a wide range of length scales of vessels [22]. Later in this section we will observe a significant change of these disparities when performing a resection.

We now assume that the left lateral section of the liver is affected by a tumor. We use our framework for modeling perfusion to investigate the behavior of the liver after resection. In particular, we consider two options for potential cuts that are illustrated in Fig. 5.13. Figure 5.14 illustrates the remaining domain of the liver and the remaining vascular tree after resection for both cut options in the inferior view. The first cut option in Fig. 5.14a corresponds to an anatomical resection of the left lateral section in which the liver segments 2 and 3 are removed (see Fig. 2.5). The discretization of the remaining liver domain after anatomical resection consists of a mesh with 5,882,171 tetrahedral elements. The second cut option in Fig. 5.14b corresponds to a non-anatomical resection with a diagonal cut. The discretization of the remaining liver domain consists of a mesh with 6,107,676 tetrahedral elements.

We note that vessels resolved in the vascular tree structure which are cut must be closed during surgery to prevent blood loss. In our simulations, we therefore do not allow blood flow through any vessel that is cut, and the blood flow of all cut vessels is

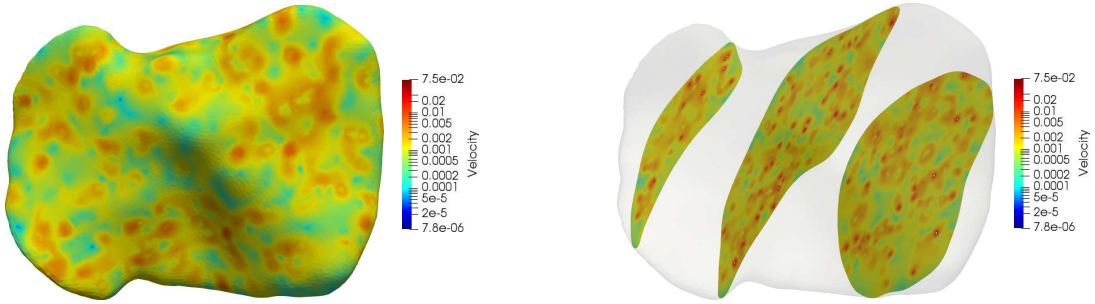

(a) Outer boundary

(b) Interior slices

Figure 5.11: Solution for velocity $\boldsymbol{w}$ $[\frac{\mathrm{m}}{\mathrm{s}}]$ of full liver model (inferior view).

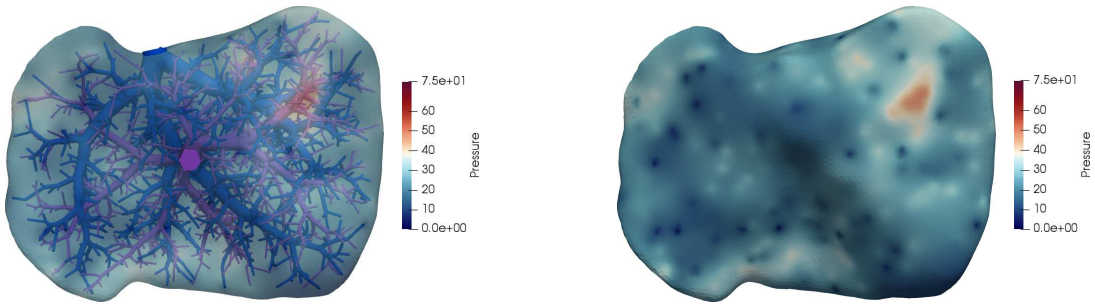

(a) Visualization with vessel trees

(b) Visualization without vessel trees

Figure 5.12: Solution for pressure field p $[\frac{\mathrm{kg}}{\mathrm{m\,s^2}}]$ of full liver model (inferior view).

redistributed over the remaining portion of the intact tree.

The simulation results, shown in Fig. 5.15, clearly outline the difference in blood supply for the two cuts. While the anatomical resection in Fig. 5.15a causes a homogeneously distributed perfusion of the domain, the non-anatomical resection in Fig. 5.15b leads to a part of liver tissue with insufficient blood supply and a part of tissue with lower blood supply compared to the same region in the unresected liver shown in Fig. 5.11. We hence conclude that the diagonal cut would suffer from uneven blood supply in the post-operative regenerative process.

In Fig. 5.16 and 5.17, we compare the corresponding pressure fields. We observe that both cut options lead to higher pressure levels in the liver after resection compared to the unresected liver shown in Fig. 5.12. This phenomenon is physiological and known as hyperperfusion. It occurs because the same amount of blood must now pass through a smaller remaining liver domain. Moreover, the non-anatomical resection in Fig. 5.17 exhibits more areas with pressure accumulation (plotted in red) and higher disparities in the pressure distribution than the anatomical resection in Fig. 5.16.

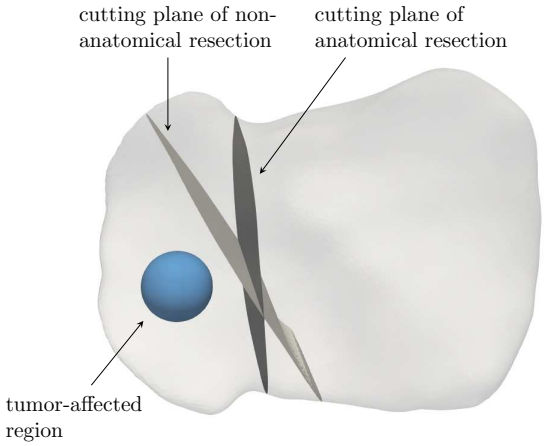

Figure 5.13: Two cutting planes for the resection of liver tissue. The blue sphere represents the tumor-affected region.

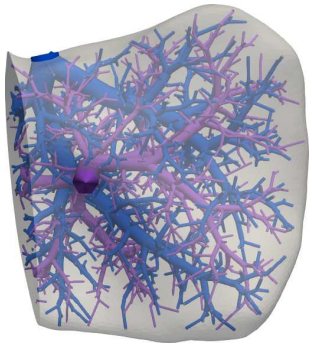

(a) Anatomical resection of the left lateral section (segments 2 and 3)

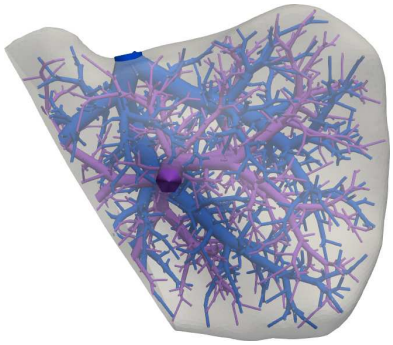

(b) Non-anatomical resection

Figure 5.14: Model representation of the resected liver.

5.4.3 Statistical analysis

In order to further compare the different results, it is useful to work with statistical quantities. For this purpose, we use the standard deviation (SD), variance (V) and coefficient of variation (CV). The latter, which is defined as the ratio of the SD to the mean. Tab. 5.3 and 5.4 show the statistical quantities based on nodal values of the pressure and velocity field of both the full and resected liver models. We observe that for both resections the mean and maximum values of pressure and velocity significantly increase. Additionally, the SD, V and CV of the resected livers are higher. This indicates that the distribution of the pressure and velocity is less homogeneous. Comparing those values of the anatomical and the non-anatomical resection shows that the non-anatomical resection causes a less homogeneous distribution. In Fig. 5.18 we plot the histogram for the nodal values of the pressure. The zero values for the pressure correspond to the

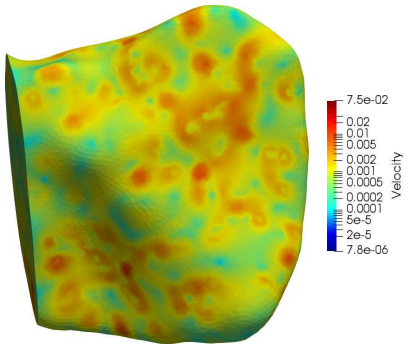

(a) Anatomical resection

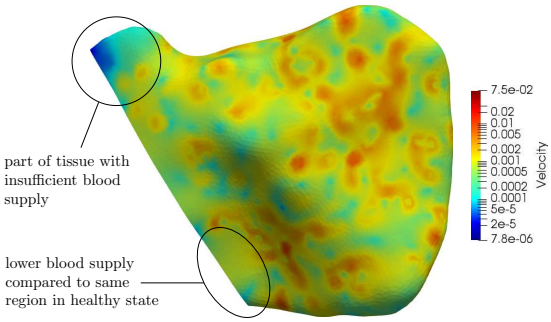

(b) Non-anatomical resection

Figure 5.15: Solution for velocity $\boldsymbol{w}$ $[\frac{\mathrm{m}}{\mathrm{s}}]$ after resection.

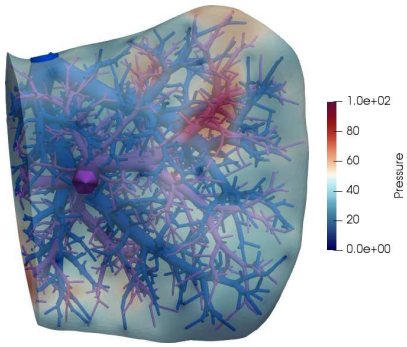

(a) Visualization with vessel trees

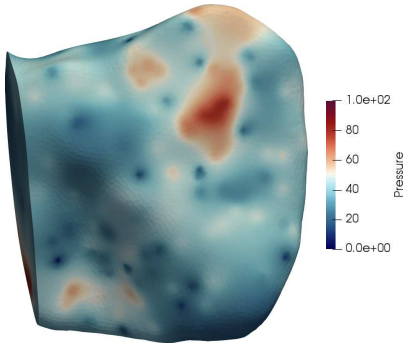

(b) Visualization without vessel trees

Figure 5.16: Solution for pressure field p $[\frac{\mathrm{kg}}{\mathrm{m\,s^2}}]$ after anatomical resection.

boundary condition at the outlet vessels. Comparing the histogram for all three models shows the same phenomena as described before. Namely, the mean value shifts, which indicate hyperperfusion, and the deviation from the mean values for the resected models is higher, which indicates a less homogeneous distribution.

Table 5.3: Statistical quantities for the velocity field (nodal values)

	Max. $[\frac{\mathrm{m}}{\mathrm{s}}]$	Mean $[\frac{\mathrm{m}}{\mathrm{s}}]$	Min. $[\frac{\mathrm{m}}{\mathrm{s}}]$	SD $[\frac{\mathrm{m}}{\mathrm{s}}]$	V $[\frac{\mathrm{m}^2}{\mathrm{s}^2}]$	CV
Full liver	$7.87 \cdot 10^{-2}$	$0.33 \cdot 10^{-2}$	$1.7 \cdot 10^{-6}$	$0.59 \cdot 10^{-2}$	$0.35 \cdot 10^{-2}$	1.79
Anatomical resection	$10.96 \cdot 10^{-2}$	$0.45 \cdot 10^{-2}$	$1.2 \cdot 10^{-5}$	$0.85 \cdot 10^{-2}$	$0.73 \cdot 10^{-2}$	1.89
Non-anatomical resection	$11.62 \cdot 10^{-2}$	$0.48 \cdot 10^{-2}$	$7.8 \cdot 10^{-7}$	$0.95 \cdot 10^{-2}$	$0.9 \cdot 10^{-2}$	1.98

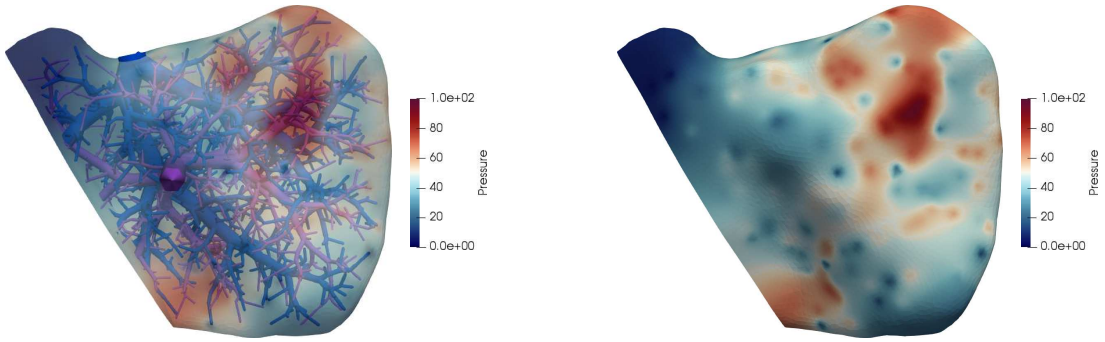

(a) Visualization with vessel trees

(b) Visualization without vessel trees

Figure 5.17: Solution for pressure field p $[\frac{\mathrm{kg}}{\mathrm{m\,s^2}}]$ after non-anatomical resection.

Table 5.4: Statistical quantities for the pressure field (nodal values).

	Max. $[\frac{\mathrm{kg}}{\mathrm{m\,s^2}}]$	Mean $[\frac{\mathrm{kg}}{\mathrm{m\,s^2}}]$	Min. $[\frac{\mathrm{kg}}{\mathrm{m\,s^2}}]$	SD $[\frac{\mathrm{kg}}{\mathrm{m\,s^2}}]$	V $[\frac{\mathrm{kg^2}}{\mathrm{m^2\,s^4}}]$	CV
Full liver	48.98	18.56	0	6.41	41.1	0.345
Anatomical resection	76.85	27.2	0	10.42	108.64	0.38
Non-anatomical resection	84.35	30.39	0	12.52	116.66	0.41

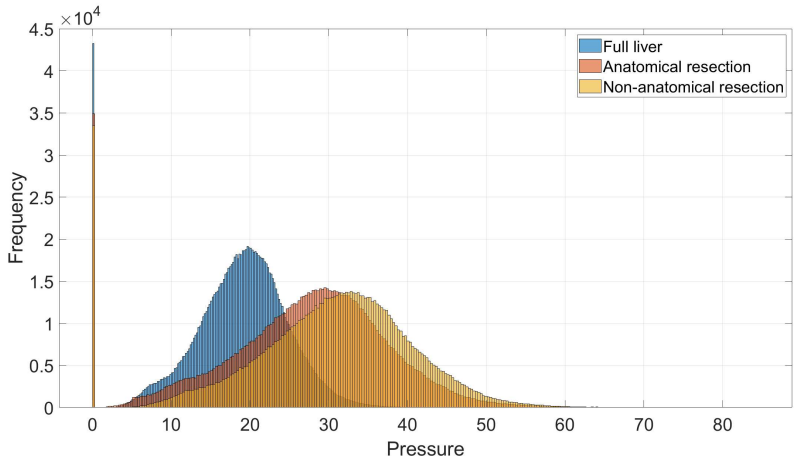

Figure 5.18: Distribution of pressure (nodal values).

5.5 Critical assessment

Modeling blood perfusion through the presented poroelastic framework of the liver has proven valuable for understanding the implications of various surgical resection scenarios on liver function. With a recent publication [69] we demonstrated the efficacy of this

approach. However, several critical issues have emerged that necessitate a reevaluation and enhancement of the modeling framework to better capture the complexities of liver perfusion.

While the results obtained from modeling liver perfusion through a poroelastic model have been promising, there are notable challenges. A significant issue arises from the implementation of Dirichlet boundary conditions, which are essential for simulating fluid flow through the draining tree. The necessity of defining boundaries for these conditions leads to the introduction of voids within the model, which can complicate the computational process. These voids, while intended to represent areas without vascular structures, introduce additional layers of complexity that affect the accuracy of the simulations.

From a computational point of view, the presence of voids necessitates intricate meshing around these regions. This increased discretization effort leads to a substantial rise in computational costs. For instance, in the case of the liver perfusion problem, the model required approximately 7.4 million elements for discretization. This level of complexity can significantly hinder the feasibility of large-scale patient-specific simulations, especially when the primary goal is to model liver growth in conjunction with perfusion.

Moreover, from a modeling point of view, the existing framework combines the lower levels of the vascular tree and microcirculation without adequately accounting for their distinct physiological characteristics. The physiological behaviors of blood flow and tissue interaction at various scales are inherently different, necessitating a multiscale approach to ensure accurate representation in simulations.

Therefore, in the following, we will introduce a modeling framework for modeling liver regrowth which consists, among other concepts, of a multiscale perfusion model. This model considers more physiological realism. By accounting for distinct characteristics across various scales within the vascular system, the model more accurately represents the complexities of liver perfusion. Additionally, the elimination of voids in the new model results in a less complex meshing requirement, significantly reducing computational costs. This makes it feasible to conduct large patient-specific simulations without excessive resource demands.

6 A modeling framework for liver tissue regrowth

In this section, we present a framework to address hyperperfusion-driven liver tissue regrowth. To address the issues with regard to the perfusion model, we propose a refined modeling framework that integrates a multiscale perfusion model and accounts for the distinct characteristics of the vascular system across different scales. Additionally, we present a framework to model hyperperfusion-driven volumetric growth based on a growth evolution equation. The results shown in the following sections are published in [70].

6.1 Fundamental concepts for modeling hyperfusion-driven liver regrowth

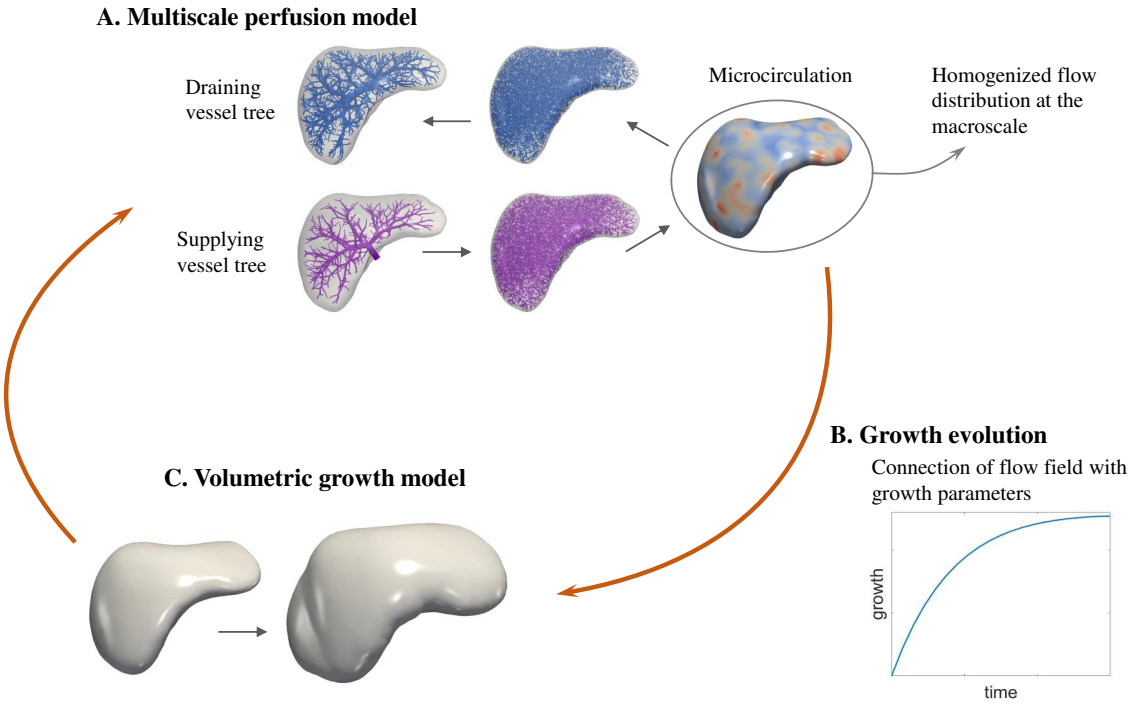

Figure 6.1: Modeling framework of liver regrowth.

Building upon our understanding of the multiscale driving mechanisms behind liver regrowth, we develop the following fundamental modeling concept, illustrated in Fig. 6.1:

A. **Multiscale perfusion model:** As the key stimulus for liver regrowth is hyperperfusion in the microcirculation, understanding the current state of blood perfusion at the lobule scale is the key prerequisite for assessing liver regrowth. We therefore require a detailed perfusion model, based on suitable scale-bridging concepts, which is able to separate the overall liver perfusion into macro- and mesoscale blood distribution and collection, and microscale blood flow through the functional units of the liver at the lobule scale. We can then use the corresponding model representation of microscale blood flow to obtain a measure of hyperperfusion in a particular region of the liver.

B. **Growth evolution model:** Once a multiscale perfusion model is established that can assess hyperperfusion at the lobule scale at each point of the liver domain, we can set up a (phenomenological) growth evolution equation that relates an increased level of blood flow to a growth rate of homogenized liver tissue, which represents the effect of hepatocyte proliferation. An important requirement is that the growth evolution equation is based on parameters that can be calibrated by available experimental data.

C. **Organ-scale growth model:** Once the growth evolution model for homogenized liver tissue is known, it can be integrated into an organ-scale growth model, for which well-established concepts exist in continuum poroelasticity. It represents macroscale growth, locally driven by the growth evolution equation, which depends on the local state of hyperperfusion in the microcirculation. We assume that lobular remodeling in the microcirculation takes effect immediately, such that macroscale growth of liver tissue also implies an increase in volume of the vasculature. In turn, growth of the liver tissue enlarges the microcirculatory domain of the perfusion model, such that hyperperfusion can be regulated at each point of the liver.

6.2 Modeling of blood flow through hierarchical vascular networks

In this section, we describe our multiscale perfusion model that corresponds to part A of our modeling framework illustrated in Fig. 6.1. It consists of two fundamental components: (a) a synthetic discrete model that represents the upper levels of the hierarchical vasculature for blood distribution and collection which has been introduced in section 4.2, and (b) a homogenized flow model that is divided into multiple compartments to individually represents the lower levels of the hierarchical vasculature for blood distribution and collection, and the microcirculation at the lobule scale.

6.2.1 Multi-compartment homogenized flow equations

The characteristic size of vessel diameters across the hierarchy of the supplying and draining trees ranges from several millimeters for the macro-scale arteries and veins to 100 micrometers for the smallest arterioles and venules [4]. With the vascular tree geometry provided by the discrete model presented above, direct flow modeling over the complete vascular tree is possible, see e.g. the technologies reviewed in [146], but requires a significant computing effort, especially within an iterative solution procedure. In order to find a compromise between resolution accuracy and computational effort, we follow a different approach that still takes into account the hierarchically complex structure of the tissue and vessels. To this end, we use the lower hierarchies of the discrete vascular trees to calibrate a porous medium, where flow can be homogenized in a continuum sense. To separately represent homogenized flow in different parts of the vascular tree, we compartmentalize the vasculature into spatially co-existing compartments and associate only those vessels to each compartment that belong to the selected (supplying or draining) tree and the selected range of spatial scales [17], [20]–[22].

To set up the model, we divide the discrete vessel structure (or parts of it) into N compartments, assigning to each compartment $i = 1, ..., N$ its own (positive definite) permeability tensor $\mathbf{K}_i$, pore pressure p_i, mass source term θ_i, and homogenized flow velocity $\mathbf{w}_i$. We consider the system of first-order differential equations that is governed by Darcy's law and the continuity equation

$$\mathbf{w}_i + \mathbf{K}_i \nabla p_i = \mathbf{0} \quad \text{in } \Omega, \tag{6.1a}$$

$$\nabla \cdot \mathbf{w}_i + Q_i = \theta_i \quad \text{in } \Omega, \tag{6.1b}$$

in each compartment i, in an open bounded region $\Omega \subset \mathcal{R}^d$, with space dimension d and impermeable outer boundary Γ. The quantities Q_i denote the pressure-dependent mass exchange between compartment i and all other compartments and are given by:

$$Q_i = \sum_{k=1}^{N} \beta_{i,k}(p_i - p_k), \tag{6.2}$$

where $\beta_{i,k} \geq 0$ denotes the perfusion coefficient for coupling compartments i and k. As such, mass exchange is absent in pressure equilibrium. We assume $\beta_{i,k} = \beta_{k,i}$ which is consistent with the mass balance $\sum_i Q_i = 0$. Due to the assumption of an incompressible fluid, we use the terms mass flow and volumetric flow interchangeably. Furthermore, the strict hierarchy of the vessels in the synthetically generated vessel tree implies that mass exchange only occurs between neighboring compartments: $\beta_{i,k} = 0$ when $k < i - 1$ or $i + 1 < k$.

Summation of (6.1b) over the compartments $i = 1, ..., N$ shows that the model (6.1) locally conserves mass:

$$\sum_{i=1}^{N} \nabla \cdot \mathbf{w}_i = \sum_{i=1}^{N} \theta_i \quad \text{in } \Omega, \tag{6.3}$$

where we have invoked the identity:

$$\sum_{i=1}^{N} Q_i = \sum_{i,k=1}^{N} \beta_{i,k}(p_i - p_k) = 0. \tag{6.4}$$

Substituting (6.1a) into (6.1b) converts the first-order system into an equivalent system of one second-order differential equation per compartment:

$$-\nabla \cdot (\mathbf{K}_i \nabla p_i) + Q_i = \theta_i \quad \text{in } \Omega. \tag{6.5}$$

Here, the pressure p_i is the sole unknown variable, and the compartment velocities $\mathbf{w}_i, i = 1, ..., N$ follow from Darcy's law in 6.1a. We supplement the model with a Neumann boundary condition to account for the impermeability:

$$-(\mathbf{K}_i \nabla p_i) \cdot \mathbf{n} = 0 \quad \text{on } \Gamma_N = \Gamma. \tag{6.6}$$

The model is equipped with the following global properties:

$$\sum_{i=1}^{N} \int_{\Omega} \theta_i \, \mathrm{d}\Omega = 0, \tag{6.7a}$$

$$\sum_{i=1}^{N} \int_{\Omega} \theta_i p_i \, \mathrm{d}\Omega \geq 0. \tag{6.7b}$$

The property (6.7a) shows that global mass is conserved, whereas (6.7b) is a global energy stability property. The global mass conservation follows from:

$$\sum_{i=1}^{N} \int_{\Omega} \theta_i \, \mathrm{d}\Omega = \sum_{i=1}^{N} \int_{\Omega} \nabla \cdot \mathbf{w}_i \, \mathrm{d}\Omega = -\sum_{i=1}^{N} \int_{\Omega} \nabla \cdot (\mathbf{K}_i \nabla p_i) \, \mathrm{d}\Omega = -\sum_{i=1}^{N} \int_{\Gamma} (\mathbf{K}_i \nabla p_i) \cdot \mathbf{n} \, \mathrm{d}\Gamma = 0, \tag{6.8}$$

where the first identity results from (6.3). To see (6.7b) we first note the identity:

$$\sum_{i=1}^{N} Q_i p_i = \sum_{i,k=1}^{N} \beta_{i,k}(p_i - p_k)p_i = \frac{1}{2} \sum_{i,k=1}^{N} \beta_{i,k}(p_i - p_k)^2 \geq 0, \tag{6.9}$$

in which we have utilized the symmetry of $\beta_{i,k}$. A straightforward substitution now provides the result:

$$\begin{aligned} \sum_{i=1}^{N} \int_{\Omega} \theta_i p_i \, \mathrm{d}\Omega &= \sum_{i=1}^{N} \int_{\Omega} Q_i p_i \, \mathrm{d}\Omega - \sum_{i=1}^{N} \int_{\Omega} \nabla \cdot (\mathbf{K}_i \nabla p_i) p_i \, \mathrm{d}\Omega \\ &= \sum_{i,k=1}^{N} \int_{\Omega} \frac{1}{2} \beta_{i,k}(p_i - p_k)^2 \, \mathrm{d}\Omega + \sum_{i=1}^{N} \int_{\Omega} (\mathbf{K}_i \nabla p_i) \cdot \nabla p_i \, \mathrm{d}\Omega - ... \\ &\quad ... - \sum_{i=1}^{N} \int_{\Gamma} p_i (\mathbf{K}_i \nabla p_i) \cdot \mathbf{n} \, \mathrm{d}\Gamma \geq 0, \end{aligned} \tag{6.10}$$

where the boundary term vanishes due to (6.6).

6.2.2 Calibrating model parameters from the vessel network

In the next step, we describe the computation of the model parameters directly from the vessel network, particularly the permeability tensors $\mathbf{K}_i$ for each compartment and the intercompartmental perfusion coefficients $\beta_{\mathrm{i,k}}$, using averaging procedures [20], [147]–[149]. In the following, the index set $\mathbb{K}_i(\mathbf{x})$ contains all indices of the vessels of compartment i that are located at least partially within an Averaging Volume (AV) of spatial position $\mathbf{x}$. Furthermore, the index set $\mathbb{I}_{ik}$ contains all indices of the vessels within the AV that belong to compartment i but share a node with one or more vessels of compartment k. As a consequence of the hierarchical structure of the compartments without skipped compartments, it follows that $\mathbb{I}_{i,k} = \varnothing$ if $|i-k| \neq 1$ and $\mathbb{I}_{i,k} \subseteq \mathbb{K}_i(\mathbf{x})$ if $|i-k| = 1$.

The components of the permeability tensor at spatial position $\mathbf{x}$ for a network of straight rigid tubes subject to Poiseuille's law can be computed according to

$$K_{ij}(x) = \frac{\pi}{8\eta V_{\mathrm{AV}}} \sum_{a \in \mathbb{K}_i(\mathbf{x})} \frac{(r_a)^4 \Delta x_{a,i} \Delta x_{a,j}}{l_a}, \tag{6.11}$$

with V_{AV} the volume of the AV, η the dynamic viscosity, r_a the vessel radius, l_a the vessel length, and $\Delta x_{a,i}$ and $\Delta x_{a,j}$ the components of the spatial vessel segment vector of vessel a (see Fig. 6.2). Note that only the segment of the vessel that actually intersects the AV is considered for Δx_a and l_a.

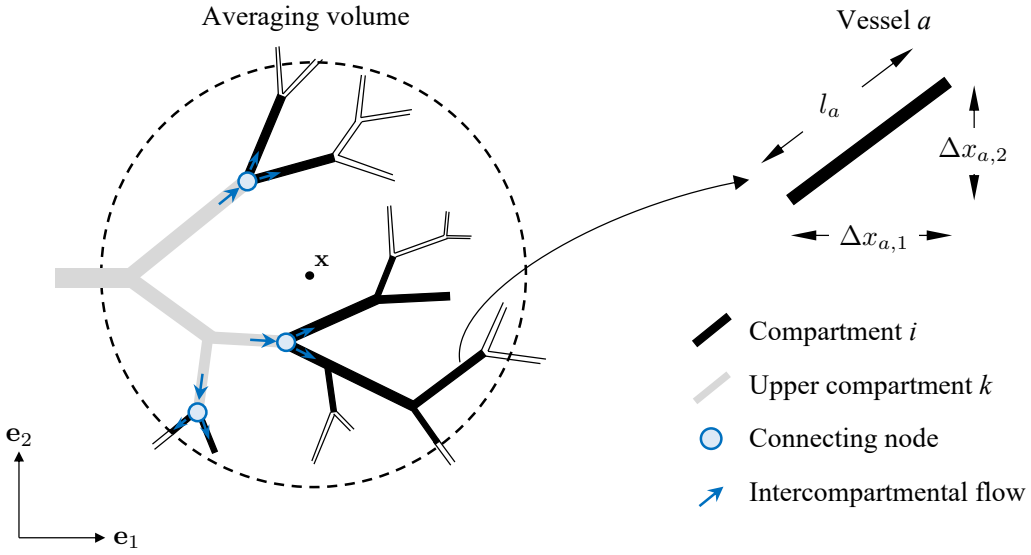

Figure 6.2: Averaging volume at spatial position $\mathbf{x}$.

Unlike the permeability tensor, which in combination with a given (and constant) dynamic viscosity can be determined solely based on geometry, the perfusion coeffi-

cients require flow quantities [20]. The synthetically generated vessel trees are based on Poiseuille's flow, providing the flow in each vessel and the pressure at each node. Using the same AV as above, we obtain the perfusion coefficient via

$$\beta_{i,k} = \begin{cases} \frac{\overline{Q}_{i,k}(\mathbf{x})}{|\overline{p}_i(\mathbf{x}) - \overline{p}_k(\mathbf{x})|} & \text{if } |\overline{p}_i(\mathbf{x}) - \overline{p}_k(\mathbf{x})| \neq 0, \\ 0 & \text{else,} \end{cases} \tag{6.12}$$

where $\overline{Q}_{i,k}(\mathbf{x})$ is the bulk-volume-average for the intercompartmental flow and can be obtained by division with the volume of the AV

$$\overline{Q}_{i,k}(\mathbf{x}) = \frac{1}{V_{\mathrm{AV}}} \sum_{a \in \mathbb{I}_{i,k}(\mathbf{x})} \hat{Q}_a, \tag{6.13}$$

where $\overline{p}_i(\mathbf{x})$ is the real-volume-average of the pressure in compartment i. For straight vessels with a constant diameter, $\overline{p}_i$ can generally be determined by

$$\overline{p}_i(\mathbf{x}) = \frac{\sum_{a \in \mathbb{K}_i(\mathbf{x})} p_a V_a}{\sum_{a \in \mathbb{K}_i(\mathbf{x})} V_a}, \tag{6.14}$$

where $V_a = \pi d_a^2 l_a / 4$ is the volume of the vessel a and p_a represents the average pressure within the vessel. Since the pressure in the vessel varies linearly (see Poiseuille's flow), the average pressure can be determined as

$$p_a = \frac{p_u + p_v}{2}, \tag{6.15}$$

where p_u and p_v are the known pressures at the proximal and distal node, respectively. When determining the mean pressure, all vessels whose end nodes are within the AV of the spatial point $\mathbf{x}$ can be considered in their entire length. To circumvent the need to determine the mean pressure of a segment section, we assume that this is true even if the starting point of the vessels lies outside this volume. For computing the perfusion coefficients coupling the lowest hierarchy of the vascular trees with the microcirculation, we use the constant and prescribed reference pressure $\overline{p}_{\mathrm{micro}} = p_{\mathrm{root}} - \Delta p$.

Remark 1. The case $|\overline{p}_i(\mathbf{x}) - \overline{p}_k(\mathbf{x})| = 0$ in (6.12) is not relevant for a hierarchical structured network as the pressure decreases continuously from the root segment to the terminals within the supplying tree and from the terminals to the root segment within the draining tree.

6.2.3 Compartmentalization strategy

In micromechanics, the suitability for homogenization is related to the existence of a RVE, which is defined as a partial volume of material that is statistically homogeneous from a macroscopic point of view, is not unique in its choice and is selected based on the assumption of a periodic microstructure [122]. Homogenization relies on the separation

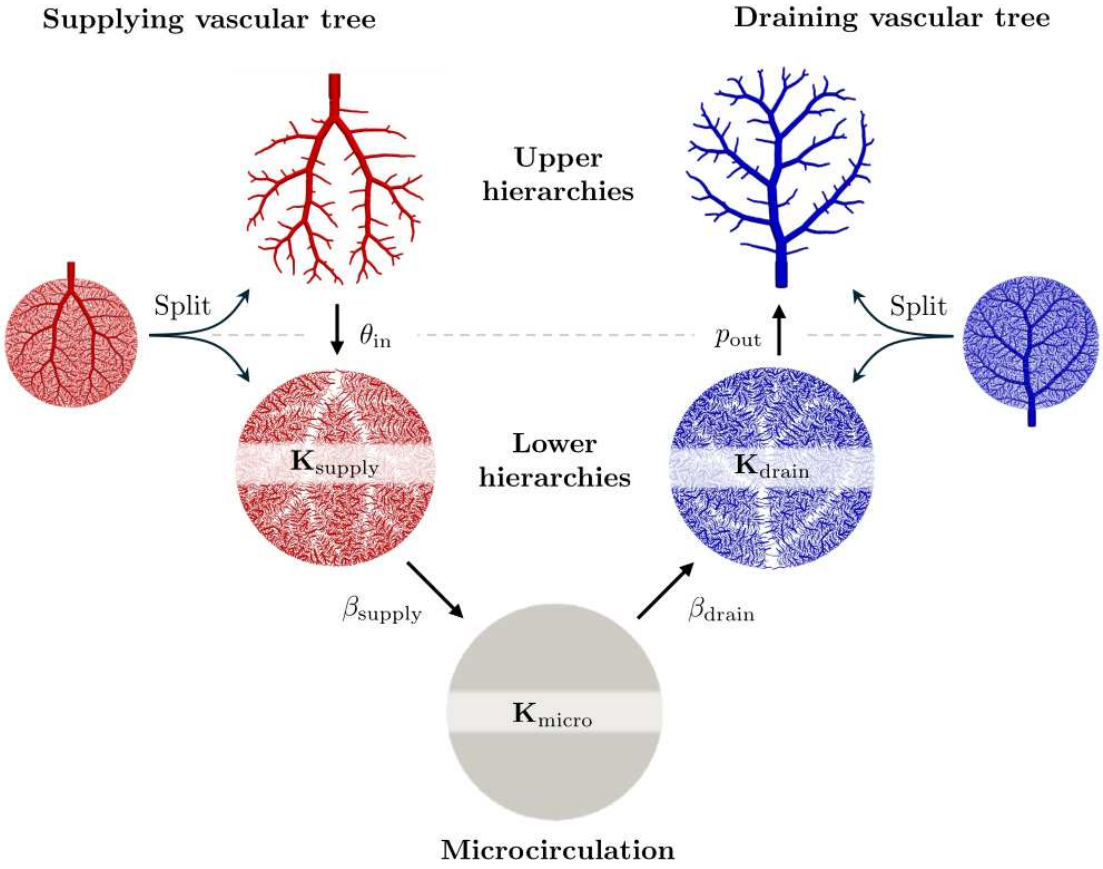

Figure 6.3: Compartmentalization of vascular tree structure.

of scales

$$d \ll l \ll L, \tag{6.16}$$

where d, l, and L denote the characteristic length of the structure of the porous medium, the averaging volume (in this sense the RVE), and the macroscopic process under consideration, see e.g. [123]–[125]. It is obvious that scale separation cannot be guaranteed for the upper hierarchies of the vascular tree structure, which therefore need to remain a network of resolved individual vessels.

We assume that vessel segments with radii below or equal to an appropriate threshold of r_{thresh} are suitable for homogenization. Therefore, we categorize the vessels $a \in \mathbb{A}$ of the vascular tree $\mathbb{T}(\mathbb{V}, \mathbb{A})$ in two groups: the lower hierarchies $\mathbb{A}_{lower}$, suitable for homogenization, and the upper hierarchies $\mathbb{A}_{upper}$, unsuitable for homogenization and which therefore must remain as a network of resolved vessels. We define

$$\mathbb{A}_{upper} = \{a \in \mathbb{A} : r_a > r_{thresh}\}, \quad \mathbb{A}_{upper} \subseteq \mathbb{A}, \tag{6.17}$$

$$\mathbb{A}_{lower} = \{a \in \mathbb{A} : r_a \leq r_{thresh}\}, \quad \mathbb{A}_{lower} \subseteq \mathbb{A}, \tag{6.18}$$

where we can also define the respective subsets of nodes

$$\mathbb{V}_{upper} = \{u, v \in a = uv : a \in \mathbb{A}_{upper}\}, \quad \mathbb{V}_{upper} \subseteq \mathbb{V}, \tag{6.19}$$

$$\mathbb{V}_{lower} = \{u, v \in a = uv : a \in \mathbb{A}_{lower}\}, \quad \mathbb{V}_{lower} \subseteq \mathbb{V}. \tag{6.20}$$

With that, we introduce the sets

$$\mathbb{V}_{conn} = \mathbb{V}_{upper} \cap \mathbb{V}_{lower}, \tag{6.21}$$

$$\mathbb{A}_{conn} = \{a = uv \in \mathbb{A}_{\text{lower}} : u \in \mathbb{V}_{conn}\}, \tag{6.22}$$

where $\mathbb{V}_{conn}$ denotes the set of nodes connecting the upper with the lower hierarchies and $\mathbb{A}_{conn}$ denotes the set of vessels of the lower hierarchies with proximal node in $\mathbb{V}_{conn}$.

Note that $\mathbb{A}_{lower}$ and $\mathbb{V}_{lower}$ can be further divided into several compartments. In the scope of the present study, we will focus on the following simple compartmentalization strategy, illustrated in Fig. 6.3 for the model problem of the circular domain: One compartment for each of the lower hierarchies of the respective vascular tree (compartment supply and compartment drainage) and the microcirculatory compartment: labeled *supply*, *micro* and *drain*.

Due to the symmetry of the perfusion coefficient and the absence of intercompartmental flow between compartment supply and drainage, i.e. $\beta_{1,3} = 0$, two perfusion coefficients remain, and we write $\beta_{1,2} = \beta_{\text{supply}}$ and $\beta_{2,3} = \beta_{\text{drain}}$. The permeability tensors of compartments supply and drainage as well as the perfusion coefficients β_{supply} and β_{drain} are determined using the averaging procedure described in Section 6.2.2. For the microcirculation, we use the isotropic permeability parameter $k_{\text{micro}} = 2 \times 10^{-8}$ mm^2 determined in [48] and set an isotropic and homogeneous permeability $K_{\text{micro}} = k_{\text{micro}}/\eta = 1/180$ mm^3 s kg^{-1}.

At the microscale, permeability is intrinsically anisotropic. However, when modeling perfusion characteristics at the lobular (meso-) scale, this anisotropy tends to average out across multiple lobules, yielding an effectively isotropic behavior. This homogenization is a necessary simplification for mesoscopic modeling. It is important to note that the compartment microcirculation of our model and its permeability represents the resistance of the sinusoid network at the microscale, see the illustration in Fig. 2.3. It cannot represent the flow patterns in the lobular structures at the mesoscale, as for instance the model in [150]. In this sense, our model can be interpreted as the averaged flow redistribution across the microcirculation, which occurs through the network of the smallest-scale venules and arterioles.

The respective resolved vascular tree structure (upper hierarchies) and the lower hierarchy compartments can be connected by deriving suitable inflow and outflow conditions at the connecting nodes $\mathbb{V}_{conn}$. This can be achieved via suitably calibrated source and sink terms θ_{in} and θ_{out} in the continuity equation (6.1b) [69]. For the inflow into compartment supply, we compute for each node $u \in \mathbb{V}_{conn}$ the net flow $\hat{Q}_{u,\text{in}}$ that enters from

the resolved part of the supplying tree into compartment supply:

$$\hat{Q}_{u,\mathrm{in}} = \sum_{\substack{a=uv \\ a\in\mathbb{A}_{conn}}} \hat{Q}_a \,. \tag{6.23}$$

To avoid singularities in the homogenized flow results due to point-wise inflow, we set up the following source function

$$\theta_{\mathrm{in}}(\mathbf{x}) = \sum_{u\in\mathbb{V}_{conn}} \frac{\hat{Q}_{u,\mathrm{in}}}{(2\pi\sigma^2)^{\frac{d}{2}}} \exp\left\{\left(-\frac{1}{2}\frac{\|\mathbf{x}-\mathbf{x}_u\|^2}{\sigma^2}\right)\right\}, \tag{6.24}$$

where we spatially distribute the net flow $\hat{Q}_{u,\mathrm{in}}$ at each node $u \in \mathbb{V}_{conn}$ in a symmetric way in the form of a weighted multivariate Gaussian distribution [69]. We note that $d = \dim(\Omega)$ is the spatial dimension of the problem and σ^2 is the variance of the radially symmetric distribution that controls the effective spread of the source distribution. In the sense of homogenization, we choose the variance to be sufficiently small with respect to the AV radius such that the distributed inflow $\hat{Q}_{u,\mathrm{in}}$ from the supplying vascular tree lies well within the range of the AV.

Remark 2. *Due to mass conservation, the following relation should hold:*

$$\int_\Omega \theta_{in}(\mathbf{x})\,\mathrm{d}V = \hat{Q}_{perf}, \tag{6.25}$$

where $\hat{Q}_{perf}$ is the inflow at the root of the supplying vascular tree. Due to the Gaussian distribution, which has unbounded support, this relation will in general not be exactly satisfied. In this paper, we assume that the corresponding mass error is sufficiently small for our application. As an alternative, one could also scale the Gaussian distribution such that its integration over the finite domain Ω yields one.

For the outflow, a pressure-dependent sink term θ_{out} is imposed in compartment drainage. Similar to the intercompartmental mass exchange, θ_{out} is introduced as a pressure-dependent outflow

$$\theta_{\mathrm{out}} = -\beta_{\mathrm{out}}(p_{\mathrm{drain}} - p_{\mathrm{out}}) \quad \text{in } \Omega_{\mathrm{outflow}}, \tag{6.26}$$

where $\Omega_{\mathrm{outflow}} \subseteq \Omega$ with $\Omega_{\mathrm{outflow}} \neq \varnothing$ denotes the region of outflow. The penalty parameter β_{out} enforces the prescribed outflow pressure p_{out} acting in a similar way as the intercompartmental perfusion coefficient and must be chosen sufficiently large.

Note that the overall outflow

$$\hat{Q}_{\mathrm{out}} = \int_\Omega \theta_{\mathrm{out}}(\mathbf{x})\,\mathrm{d}\Omega = -\hat{Q}_{perf}, \tag{6.27}$$

is regulated by global mass conservation

$$\sum_{i=1}^{N} \int_{\Omega} \theta_i \, \mathrm{d}\Omega = \sum_{i=1}^{N} \int_{\Omega} \nabla \cdot \mathbf{w}_i \, \mathrm{d}\Omega = -\sum_{i=1}^{N} \int_{\Omega} \nabla \cdot (\mathbf{K}_i \nabla p_i) \, \mathrm{d}\Omega = -\sum_{i=1}^{N} \int_{\Gamma} (\mathbf{K}_i \nabla p_i) \cdot \mathbf{n} \, \mathrm{d}\Gamma = 0, \tag{6.28}$$

which results from summation of (6.1b).

Finally, the system of equations (6.5) for our compartmentalization strategy reads

$$-\nabla \cdot (\mathbf{K}_{\mathrm{supply}} \nabla p_{\mathrm{supply}}) + Q_{\mathrm{supply}} = \theta_{\mathrm{in}} \quad \text{in } \Omega, \tag{6.29a}$$

$$-\nabla \cdot (\mathbf{K}_{\mathrm{micro}} \nabla p_{\mathrm{micro}}) + Q_{\mathrm{micro}} = 0 \quad \text{in } \Omega, \tag{6.29b}$$

$$-\nabla \cdot (\mathbf{K}_{\mathrm{drain}} \nabla p_{\mathrm{drain}}) + Q_{\mathrm{drain}} = \theta_{\mathrm{out}} \quad \text{in } \Omega, \tag{6.29c}$$

with the intercompartmental flow rate densities

$$Q_{\mathrm{supply}} = \beta_{\mathrm{supply}} (p_{\mathrm{supply}} - p_{\mathrm{micro}}), \tag{6.30a}$$

$$Q_{\mathrm{micro}} = \beta_{\mathrm{supply}} (p_{\mathrm{micro}} - p_{\mathrm{supply}}) + \beta_{\mathrm{drain}} (p_{\mathrm{micro}} - p_{\mathrm{drain}}), \tag{6.30b}$$

$$Q_{\mathrm{drain}} = \beta_{\mathrm{drain}} (p_{\mathrm{drain}} - p_{\mathrm{micro}}). \tag{6.30c}$$

6.2.4 Prototypical model problem in 2D

We further illustrate the concepts of our multi-compartment perfusion model via the model problem of a 2D circular disk with a radius of 10 mm. We use the supplying and draining tree structures described by Fig. 4.2 and Tab. 4.1 and apply our compartmentalization strategy illustrated in Fig. 6.3. Furthermore, we discretize the circular domain into a mesh of 459 standard six-noded triangular elements (see Fig. 6.4a).

The material parameters are determined by assigning a circular AV at the center of the respective mesh element. On the one hand, the AV size must be chosen sufficiently large to ensure that scale separation holds and homogenization can be applied. On the other hand, the AV size cannot be too large such that macroscale variations in the material parameters are not lost by averaging. The optimal choice of AV size is always task-specific and ideally should be validated through a sensitivity study. A sensitivity study in this regard has been performed in [20]. A suitable AV dimension in the range of about 1/10 of the domain dimension has been proposed based on finding a suitable balance between increasing the smoothness of the Darcy pressure and minimizing its deviation from the Poiseuille pressure. We specify the dimension of each AV by choosing its radius one order of magnitude smaller than the characteristic length of the domain, i.e. 1 mm. The resulting permeability tensors and perfusion coefficients are assigned to the corresponding element, where it is assumed to be constant in that element. We choose the threshold for separation to $r_{thresh} = 0.1\,\mathrm{mm}$, one order of magnitude smaller than the AV size.

Remark 3. *The statement on the size of the AV, according to which its characteristic length should be chosen sufficiently large to ensure an adequate continuum representation of all (discontinuous) properties of the microstructure, and sufficiently small to*

avoid smoothing macroscopic variations of these properties throughout the domain can also be seen as the restriction to (6.16)*. It should be ensured that a sufficient number of vessels from the considered compartment are present in the AV, thereby guaranteeing a homogenized and continuous representation of the microscopic structure with a desired level of smoothness. Additionally, the AV size should be chosen sufficiently small to prevent the smoothing of macroscopic heterogeneities across the entire domain. Accordingly, in the sense of practicability of modeling the vessel tree as a multi-compartment Darcy model, the strict constraints of scale separation* (6.16) *should be replaced by a weakened condition on the dimensional relations of the structure*

$$r < l < L, \tag{6.31}$$

where r denotes the largest vessel radius within the compartment (0.1 mm), l is the radius of the circular AV (1 mm) and L corresponds to the radius of the circular domain (10 mm). Therefore, with the present choice of AV size and the separation criterion r_{thresh}, the classical requirements of scale separation for homogenization are not fully met. However, in terms of efficient computation with the given trees, the scale separation of one order of magnitude each is considered sufficient.

We illustrate homogenized material parameters by plotting the perfusion coefficient β_{supply} component in Fig. 6.4 and the permeability in Fig. 6.5. We can observe in Figs. 6.4a and 6.5a that for an AV radius of 1 mm, geometry and topology of the resolved larger vessels is reflected in the material parameters of the supply and drainage compartments. This result is intuitively clear, as the presence of a (resolved) larger vessel implies the absence of smaller vessels (to be homogenized), which directly leads to a decrease in the corresponding permeability tensor and perfusion coefficient. In our case, we would like to maintain this mechanism to (a) implicitly represent the flow obstacle due to the resolved larger vessels in the homogenized compartments, and (b) mitigate intercompartmental flow from the compartment supply into the microcirculation and from the microcirculation into compartment drainage. Hence, we conclude from Figs. 6.4a and 6.5a that the AV radius size must be appropriately chosen in the sense that macroscopic heterogeneities of the material parameters are not smoothed too heavily over the entire domain. This observation does not apply to a larger AV radius, such as 5 mm, as demonstrated in Figs. 6.4b and 6.5b. We note that unlike in the current 2D case, blood can flow around the obstacles in a 3D liver representation by using the third dimension.

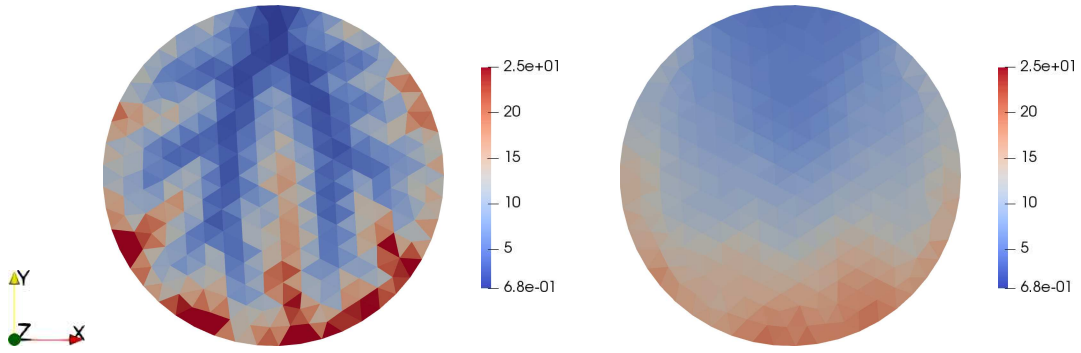

(a) AV radius of 1 mm (b) AV radius of 5 mm

Figure 6.4: Perfusion coefficient β_{supply} [mm s kg^{-1}] for coupling compartment supply and compartment microcirculation.

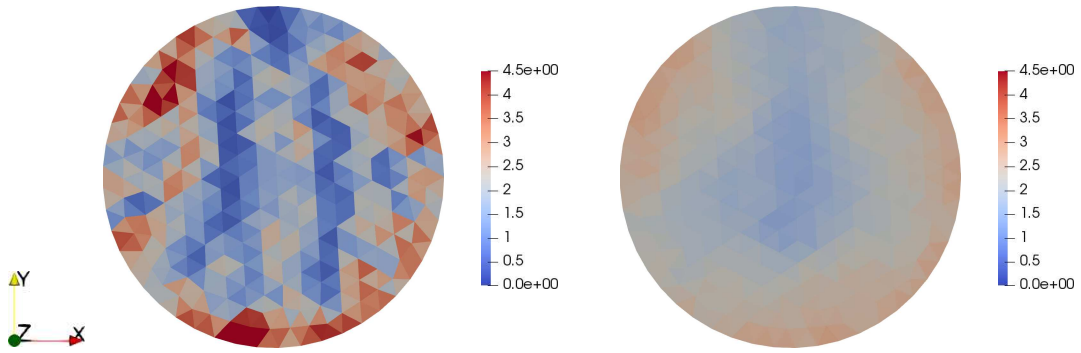

(a) AV radius of 1 mm (b) AV radius of 5 mm

Figure 6.5: Permeability component K_{yy} [mm^3 s kg^{-1}] for compartment supply.

We solve the associated coupled boundary value problems (6.5) and (6.6) of the compartmentalized model via the open-source finite element framework FEniCS [140], using standard quadratic nodal basis functions on the triangular mesh shown in Fig. 6.4a. The averaged outflow pressure p_{out} is enforced by a sufficiently large penalty parameter $\beta_{\text{out}} = 10^5$.

We utilize the Bubunov-Galerkin finite element method [139] for the discretization of the reduced multi-compartment Darcy model in (6.5). Multiplication with discrete test functions $q_{h,i}$, integrating over the domain Ω, and subsequently applying integration by parts leads to the weak statement: Find $p_{h,i} \in \mathcal{W}_{h,i}$ such that for all $q_{h,i} \in \mathcal{W}_{h,i}$:

$$\int_\Omega \left(\mathbf{K}_i \nabla p_{h,i}\right) \cdot \left(\nabla q_{h,i}\right) \mathrm{d}\Omega + \int_\Omega q_{h,i} \sum_{k=1}^{N} \beta_{i,k}(p_{h,i} - p_{h,k}) \,\mathrm{d}\Omega = \int_\Omega \theta_i q_{h,i} \,\mathrm{d}\Omega, \tag{6.32}$$

where subscript h denotes the discretized version of the quantity. The discrete function space $\mathcal{W}_{h,i}$ consists of Lagrange basis functions of degree $P = 2$. Selecting the weighting

functions as $q_{h,i} = 1$ and $q_{h,i} = p_{h,i}$ shows that the discretization inherits the conservation and energy-stability properties (6.33):

$$\sum_{i=1}^{N} \int_{\Omega} \theta_i \, \mathrm{d}\Omega = 0, \tag{6.33a}$$

$$\sum_{i=1}^{N} \int_{\Omega} \theta_i p_{h,i} \, \mathrm{d}\Omega \geq 0. \tag{6.33b}$$

Note that (6.33b) implies coercivity of the associated bilinear form:

$$B(\{p_{h,i}\}_{i=1,\dots,N}, \{p_{h,i}\}_{i=1,\dots,N}) \geq 0, \tag{6.34}$$

where the bilinear form is given by:

$$\begin{aligned} B(\{p_{h,i}\}_{i=1,\dots,N}, \{q_{h,i}\}_{i=1,\dots,N}) = & \int_{\Omega} \left(\mathbf{K}_i \nabla p_{h,i}\right) \cdot \left(\nabla q_{h,i}\right) \, \mathrm{d}\Omega + \dots \\ & \dots + \int_{\Omega} q_{h,i} \sum_{k=1}^{N} \beta_{i,k} (p_{h,i} - p_{h,k}) \, \mathrm{d}\Omega. \end{aligned} \tag{6.35}$$

The results of the pressure fields for all three compartments are shown in Fig. 6.6. We observe that compartments supply and drainage exhibit pronounced pressure differences, following the structure of the resolved supplying and draining trees. In the microcirculation, in contrast, we can see an almost uniform pressure field. In particular, the pressure in compartment supply decreases from the root to the terminals. In compartment drainage, we observe that the pressure decreases from the terminals to the root.

Figure 6.7 presents the velocity magnitudes across all three compartments. The streamlines indicate that flow consistently moves away from upper hierarchy vessels within the compartment supply and towards them within the compartment drainage. The observed flow directions agree with the orientations of the vessels in the lower hierarchies of the corresponding vascular tree, as depicted in Fig. 4.2.

In the compartment microcirculation, the velocity magnitudes are three orders of magnitude lower than those observed in the compartments supply and drainage. Therefore, a flow redistribution through the compartment microcirculation does not occur. This observation is in agreement with our interpretation that the compartment microcirculation represents the flow resistance of the microscale sinusoids, but cannot involve significant flow redistribution at the macroscale, as the lobular structure would not allow that.

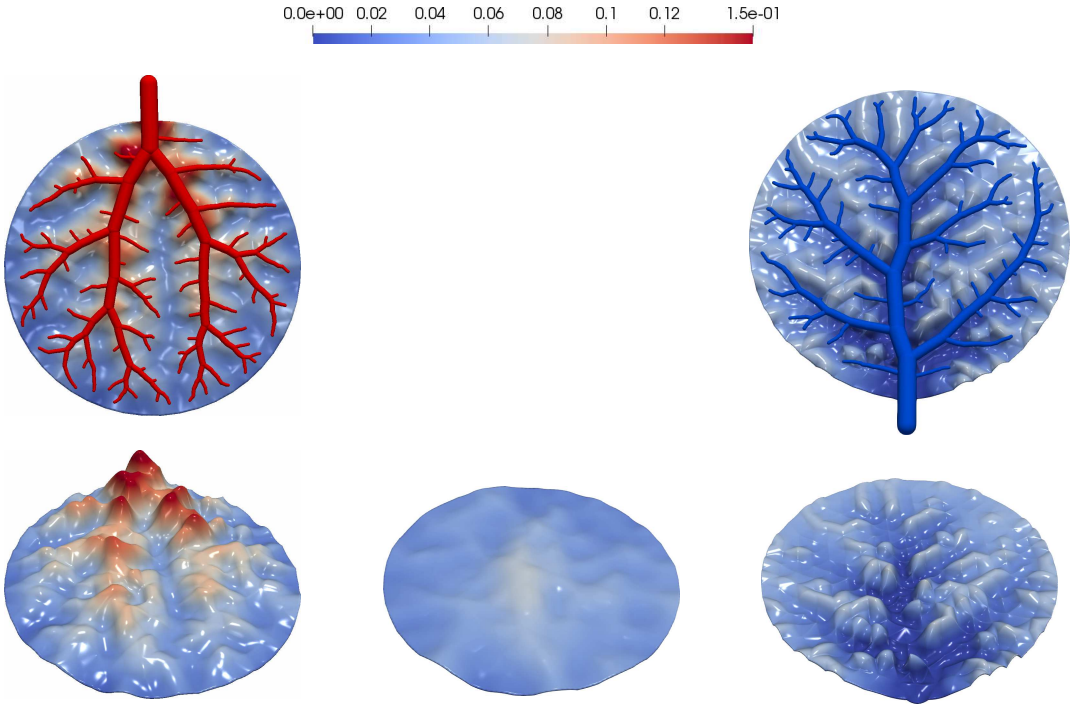

Figure 6.6: FE solution of the pressure fields p_i [kg mm^{-1} s^{-2}] for the model problem of the circular domain.

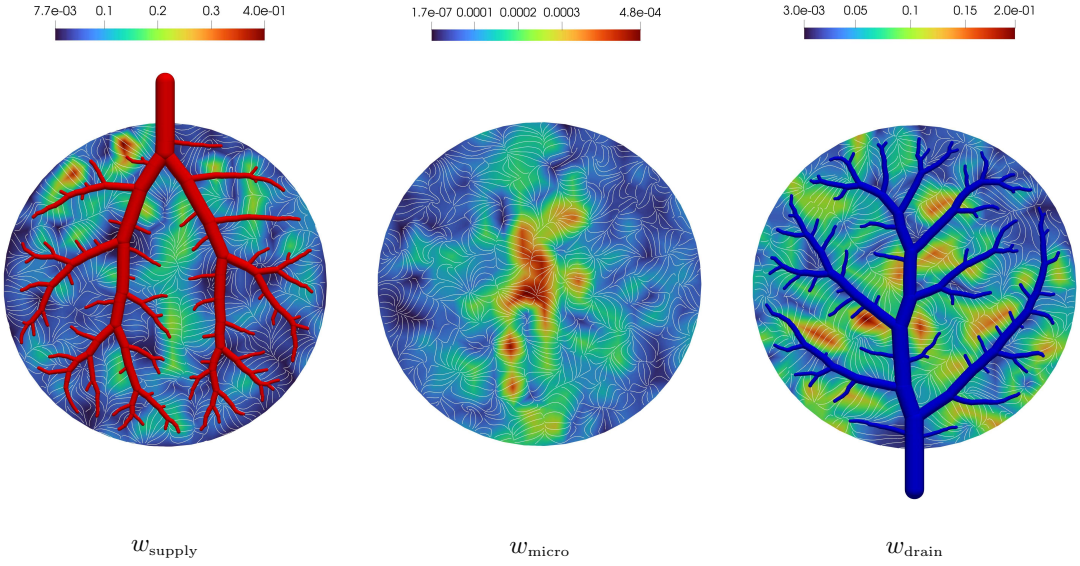

Figure 6.7: FE solution of the homogenized velocity magnitude fields w_i [mm s^{-1}] for the model problem of the circular domain with streamlines indicating the directions of flow.

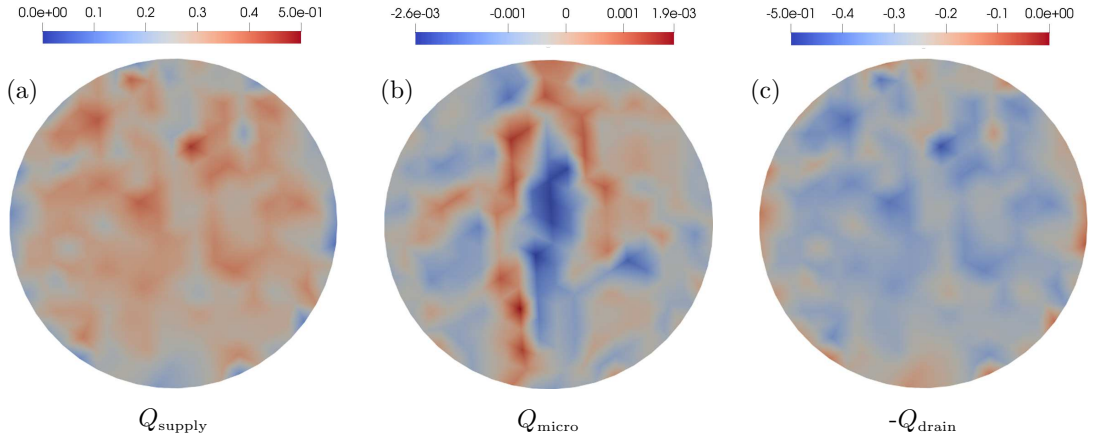

Figure 6.8: FE solution of homogenized intercompartmental flow fields Q_i [s^{-1}] for the model problem of the circular domain representing (a) the supply and (c) the drainage of compartment microcirculation. In (b) the difference between supply and drainage is depicted, representing the redistribution of fluid within compartment microcirculation.

Figure 6.8 shows the intercompartmental flow rate densities, computed from (6.30a), (6.30b) and (6.30c). The patterns for supply into and drainage from the microcirculation do not show large variations across the domain. The difference between supply and drainage confirms that a significant fluid redistribution at the macroscale within the compartment microcirculation does practically not occur, as its magnitude is two orders lower than supply and drainage. In other words, the fluid flowing into the microcirculation at a particular location also flows out at the same location.

6.3 A hyperperfusion-driven poroelastic growth model

In this section, we present our model for compensatory liver regrowth driven by hyperperfusion at the lobule scale. It is based on a flow dependent evolution equation that corresponds to part B of our modeling framework, illustrated in Fig. 6.1. We extend the multi-compartment perfusion model by a poroelastic growth model that is defined at the lobule scale, but provides a growth map for the resolved vessel trees and the compartments 1 (supply) and 3 (drainage). Additionally, we discuss how our model represents lobular remodeling at the microcirculation as well as remodeling in the vascular tree. The poroelastic growth model corresponds to part C of our modeling framework, illustrated in Fig. 6.1.

The coupling of tissue deformation and fluid flow can naturally be achieved within the framework of poroelasticity as introduced in section 3, which can be rigorously based on continuum mixture theory [126]. For a comprehensive review, we refer the interested reader to [127]–[129], [132], and particularly for large deformation formulations to [69], [131], [133], [134]. Models to describe growing poroelastic media have also been proposed [151], [152], including tissue growth [150], [153], biomass growth [154] or tumor growth [155]–[157].

6.3.1 Homogenization and porosity

We start by focusing on the liver lobule scale, as described in Section 2.2.2 and illustrated in Fig. 2.3. In line with our discussion on perfusion in Section 6.2, we idealize the lobule scale as a porous material in the sense of a heterogeneous mixture. In our model, it consists of two constituents: a skeleton phase that includes all cells, the extracellular matrix and the interstitial fluid, and one perfusion phase that represents the blood moving through the sinusoids. Corresponding quantities are indexed by *skel* and *perf*, respectively.

We recall the notion of an averaging volume (AV), discussed in Section 6.2.2. The two-constituent porous material is illustrated at the micro- and macroscale in Fig. 6.9. Following averaging over a representative AV at the microscale, the volume fraction of the perfusion phase can be described by the porosity $\phi = \phi^{perf}$. The porosity can be expressed at the macroscale as

$$\phi(\mathbf{x}, t) = \frac{dV^{perf}}{dV} \tag{6.36}$$

where dV^{perf} is the incremental volume of the perfusion phase after homogenization and dV is the incremental total volume. In a two-phase mixture under the assumption of absent void spaces (full saturation), one can express the volume fracture of the skeleton as $\phi^{skel} = 1-\phi$. We note that the corresponding total mass at each point of the macroscale domain is

$$dm = \left(\rho^{perf}\phi + \rho^{skel}(1-\phi)\right) dV \tag{6.37}$$

where ρ^{perf} and ρ^{skel} are the true densities of the perfusing blood and the tissue skeleton, respectively. We recall that ρ^{perf} is constant based on our incompressibility assumption for blood, and in addition, we assume ρ^{skel} to be constant as well.

6.3.2 Kinematics of growth

Analogous to section 3.2.1, we assume that the Lagrangian configuration of the constituents coincides and that each of the two constituents of the porous material simultaneously occupies a common spatial region. Accordingly, the deformation map $\mathbf{x} = \chi(\mathbf{X}, t)$ describes the spatial position of a particle of the liver lobule (see Fig. 6.9).

To incorporate growth into the framework, the deformation map is decomposed into two components, illustrated in Fig. 6.9. A material point is first mapped into an intermediate, incompatible growth configuration Ω_g. This state is considered stress-free, and only mass generation occurs between Ω_0 and Ω_g. To ensure compatibility of the domain, elastic deformations are then applied to the intermediate configuration [23]. The split of the deformation map into two consecutive mappings leads to a multiplicative decomposition of the deformation gradient

$$\mathbf{F} = \mathbf{F}_e\mathbf{F}_g, \tag{6.38}$$

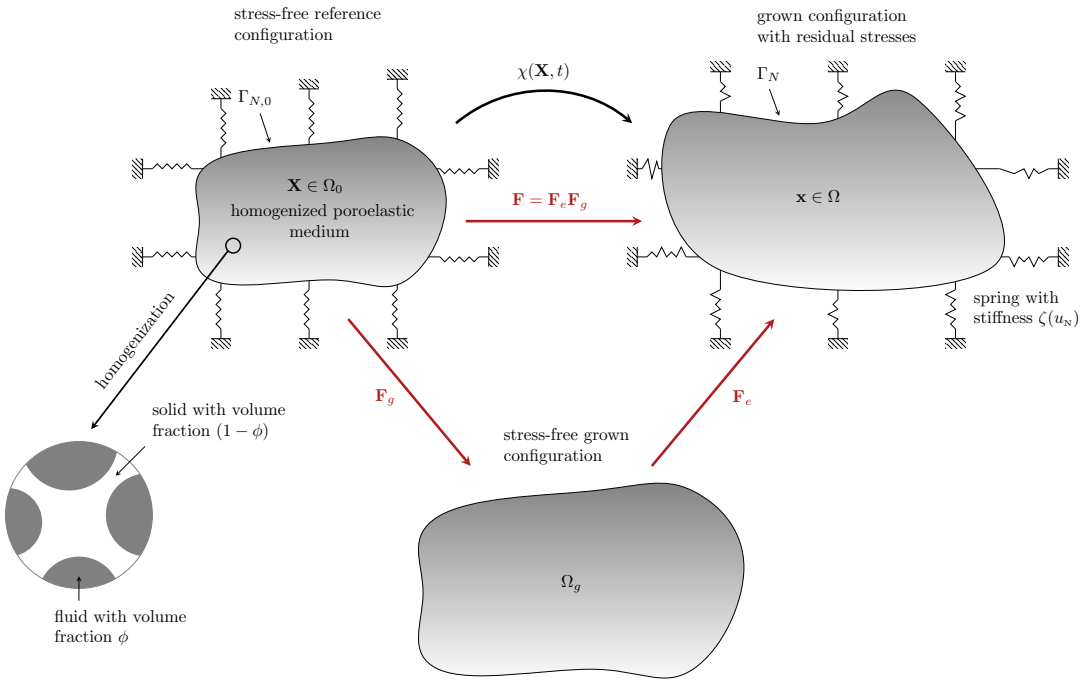

Figure 6.9: Kinematics of finite growth of a poroelastic medium.

into a purely elastic part $\mathbf{F}_e$ and a growth deformation gradient $\mathbf{F}_g$ [23], analogous to the decomposition of the deformation gradient in elastoplasticity [158]. Accordingly, we introduce the elastic part of the right Cauchy-Green strain tensor

$$\mathbf{C}_e = \mathbf{F}_e^T\mathbf{F}_e. \tag{6.39}$$

6.3.3 Balance laws and constitutive equations

Liver regeneration is a dynamic and multiscale process that occurs over various scales in space and time. As our growth model is formulated at the macroscale, where the time scale consists of days or weeks, we can describe liver growth within this time window by a sequence of quasi-static growth processes, within which we can neglect any time-dependent effects.

We then introduce the momentum balance, assuming a quasi-static setting and the absence of body forces, in reference configurations as

$$\nabla_0 \cdot (\mathbf{FS}) = \mathbf{0} \quad \text{in } \Omega_0. \tag{6.40}$$

Analogous to the idea in section 5.1, we augment the balance of momentum with an

interaction term

$$W_c(u_{\mathrm{N}}) = \zeta u_{\mathrm{N}}, \tag{6.41}$$

with ζ representing the nonlinear stiffness of the spring element. This term is supported on the outer boundary of the liver $\Gamma_{N,0}$ and accounts for the contact of the liver with surrounding organs (see Fig. 6.9). The contact contribution is applied in the normal direction, where $\mathbf{N}$ denotes the outward unit normal vector on the boundary $\Gamma_{N,0}$, and $u_{\mathrm{N}} = \mathbf{u} \cdot \mathbf{N}$ is the normal component of the displacement vector. The effect of spring elements at the boundary is best included variationally in the weak formulation of the balance of linear momentum. For details, we refer the interested reader to [69], [159] and the references therein.

The nonlinear deformation-dependent stiffness $\zeta(u_{\mathrm{N}})$ is given by equation (5.2) where we set $c = 2$.

We recall the pressure equation in (6.5), which we obtained upon substituting Darcy's law (6.1a) into the balance of fluid mass (6.1b). These relations also arise in the theory of poroelasticity and are therefore also applicable for compartment microcirculation, where coupling with compartments supply and drainage is ensured by the mass exchange term Q_{micro}, see (6.29b). We use the pull-back operation $\nabla = \mathbf{F}^{-T}\nabla_0$ and the identity $\nabla \cdot \mathbf{w}\, d\Omega = \nabla_0 \cdot (J\mathbf{F}^{-1}\mathbf{w})\, d\Omega_0$ for the mapping of (6.5) to the reference configuration Ω_0

$$-\nabla_0 \cdot (\mathbf{K}_{i,0}\nabla_0 p_i) + \sum_{k=1}^{N} \beta_{i,k,0}(p_i - p_k) = \theta_{i,0} \quad \text{in } \Omega_0, \tag{6.42}$$

with ∇_0 denoting the material gradient and $\mathbf{K}_{i,0}$, $\beta_{i,k,0} = J\beta_{i,k}$, $\theta_{i,0} = J\theta_i$ denoting the permeability tensor, the perfusion coefficient, and the source term in the reference configuration, respectively. The pull-back operation for the permeability tensor is defined by

$$\mathbf{K}_{i,0} = J\mathbf{F}^{-1}\mathbf{K}_i\mathbf{F}^{-T}. \tag{6.43}$$

For compartments supply and drainage we can find simple update relation for the permeability tensors and perfusion coefficients based on the assumption that the perfusion properties of the vascular network are maintained during growth. Given the deformation field for each quasi static iteration step, the update formulations read

$$\mathbf{K}_i = J^{-1}\mathbf{F}\,\mathbf{K}_i\big|_{t=0}\mathbf{F}^T, \quad i = \text{supply, drain} \tag{6.44}$$

$$\beta_{i,k} = J^{-1}\beta_{i,k}\big|_{t=0}, \qquad i = \text{supply, drain} \tag{6.45}$$

where $\mathbf{K}_i|_{t=0}$ and $\beta_{i,k}|_{t=0}$ denote the permeability and perfusion coefficient in the initial state, respectively. Using these relations, we avoid the computationally expensive redetermination of the model parameters in each iteration step. Inserting (6.44) into (6.43) shows constancy of the permeability tensor in the reference configuration, whereby the same applies to the perfusion coefficient.

For compartment microcirculation, we assume that lobular remodeling preserves the

permeability of the microcirculation, i.e. the permeability remains isotropic and, in the current configuration, equal to the initial value. Therefore, equation (6.44) is not applicable, and $K_{\text{micro},0}$ is determined using (6.43).

Remark 4. *Equations (6.42) describe the mass balance equations of the fluid constituents. The skeleton mass balance equations are not explicitly part of the proposed modeling framework since the skeleton partial density $\rho^{skel}(1-\phi)$ does not appear in both the fluid mass balance laws (6.42) and the total momentum equation (6.40).*

Similiarly to section 3.4.2, we work with the concept of effective stress and decompose the Cauchy stress as

$$\sigma = \sigma' - p_{\text{micro}}\mathbf{I}, \tag{6.46}$$

where p_{micro} is now the interstitial fluid pressure in the liver microcirculation. Considering this and incorporating the split of the deformation gradient $\mathbf{F} = \mathbf{F}_e\mathbf{F}_g$ lead to the following updated constitutive relations:

$$\mathbf{S} = \mathbf{S}' - Jp_{\text{micro}}\mathbf{C}^{-1}, \tag{6.47a}$$

$$\mathbf{S}' = 2J_g\mathbf{F}_g^{-1}\frac{\partial\Psi^{\text{skel}}}{\partial\mathbf{C}_e}\mathbf{F}_g^{-T}, \tag{6.47b}$$

$$p_{\text{micro}} = -\frac{\partial\Psi^{\text{vol}}}{\partial J^s}, \tag{6.47c}$$

where J_g is the determinant of the growth deformation gradient and Ψ^{skel} and Ψ^{vol} are given by equations (3.32) and (3.33), respectively.

6.3.4 Isotropic compensatory growth

Following our exposition in section 2.4, we recall that hepatocyte proliferation is the central mechanism by which the liver regains its mass. Growth factors and cytokines that drive hepatocyte proliferation at the cell level can quickly spread with the blood flow due to the thorough vascularization of the liver, ensuring that regenerative signals reach all parts of the liver. Additionally, lobular remodeling supports the even distribution of blood flow through the regenerating lobule tissue. Therefore, we assume that hepatocytes proliferate uniformly, leading to a consistent increase in liver mass in all directions

At the microscale, growth might still occur orthotropically, as hepatocyte proliferation might differ along the sinusoid axis in flow direction and perpendicular to the sinusoid axis. We can assume, however, that even in this case, liver regrowth can be regarded as isotropic from a macroscopic viewpoint, so that any potential direction dependence would be averaged out in the homogenization process.

We therefore consider compensatory volumetric growth to occur isotropically, expressed in the following classical form:

$$\mathbf{F}_g = \vartheta^{1/3}\,\mathbf{I}, \tag{6.48}$$

where the growth factor ϑ denotes the volumetric change due to growth [25]. It corresponds to the determinant of the growth deformation tensor

$$\vartheta = \det \mathbf{F}_g = J_g = \frac{dV^g}{dV^0} \tag{6.49}$$

which denotes the ratio between the volume increase in the intermediate configuration and the initial volume in the reference configuration at each point of the macroscale domain. In the context of our quasi-static poroelastic model, we assume that we can keep the same porosity when we map each AV from the initial to the intermediate configuration. Hence, we can write for the change in mass at the macroscale:

$$\begin{aligned} dm^g &= \left(\rho^{perf}\phi + \rho^{skel}(1-\phi)\right) dV^g \\ &= \vartheta \left(\rho^{perf}\phi + \rho^{skel}(1-\phi)\right) dV^0 \\ &= \vartheta \, dm^0. \end{aligned} \tag{6.50}$$

We emphasize that in (6.50), the growth factor is not only applied to the tissue skeleton, but also to the perfusing blood. In the context of our quasi-static model, the associated "growth" of the fluid, $\vartheta\rho^{perf}\phi dV^0$, represents the added mass of the blood that occupies additional sinusoid space. We also refer to the discussion in terms of lobular remodeling in Section 6.3.7 below.

Following (6.50), the interpretation of the growth factor ϑ in terms of the change in homogenized mass under consistent microstructure is straightforward:

$$\vartheta = \frac{dm^g}{dm^0}. \tag{6.51}$$

We note that depending on the growth stimulus, the growth factor ϑ can take different forms [24], [26], e.g. strain-driven [27], [32], [33], stress-driven [33], [38], [160] or nutrient-driven [27], [37].

6.3.5 Hyperperfusion as the main stimulus

Growth evolution laws describe how living tissues alter their shape in response to external stimuli. These laws establish a relationship between the growth tensor $\mathbf{F}_g$ and mechanical fields, chemical fields, or biological signaling [24]. There have been a number of attempts to derive universal growth laws from fundamental physical principles. Several of these are based on thermodynamic considerations. However, there is no consensus on the primary drivers of growth processes [24], [161].

Following our exposition in Section 2.4, we identified hyperperfusion in the microcirculation as the starting stimulus for liver regrowth. Our perfusion model, derived in the previous section, explicitly captures the local blood flow into and out of the microcirculation at each point within the liver domain. The corresponding quantity is the intercompartmental flow Q_{micro}, given by (6.30b), which represents the homogenized volumetric flow rate per volume between the compartments supply and drainage and the

microcirculation. Due to the compartmentalized structure of the perfusion model, the local blood flow into and out of the microcirculation naturally separates from the flow that occurs within the supply and drainage trees.

In the scope of the current work, we choose to adopt the inflow rate into the microcirculation, which is the first part of Q_{micro} in (6.30b) as an effective measure of (hyper-)perfusion in the microcirculation. Due to mass conservation, the inflow rate is equivalent to the outflow rate Q_{supply}, given in (6.30a), from the compartment supply into the compartment microcirculation, which we will use in the following.

We will establish a measure for compensatory volumetric growth, described through an evolution equation, through a data-based phenomenological relationship to (hyper-)perfusion, measured by the homogenized inflow rate field into the microcirculation. The complex cell-scale mechanisms briefly touched upon in Section 2.4 and sketched in Fig. 2.7 are not explicitly represented in this model, but incorporated implicitly through data calibration.

Motivated by existing growth models for other biological tissues [27], we adopt the following form of the evolution equation for the growth factor ϑ that results from the multiplication of a growth scaling factor with a mechanism-specific growth criterion:

$$\dot{\vartheta}(\mathbf{X}) = \begin{cases} k_\vartheta(\vartheta)\ \ \gamma_g(Q_{\text{supply}}) & \text{for } \gamma_g(Q_{\text{supply}}) > 0, \\ 0 & \text{for } \gamma_g(Q_{\text{supply}}) \leq 0. \end{cases} \tag{6.52}$$

which is defined at each point of the macroscale domain. The specific form (6.52) enables the separation of the dependence on the size of the growth factor ϑ itself and the mechanism-specific field variable Q_{supply} into two separate variables k_ϑ and γ_g, which can then be considered one at a time.

We begin with the liver-specific growth criterion γ_g. Following our discussion on hyperperfusion-driven growth, we propose the following new growth criterion γ_g,

$$\gamma_g = \frac{|Q_{\text{supply}}| - |\tilde{Q}_{\text{equi}}|}{|\tilde{Q}_{\text{equi}}|}. \tag{6.53}$$

which depends on the current homogenized blood flow rate into the microcirculation (after resection). It is related to $\tilde{Q}_{\text{equi}}$, which denotes the homogenized blood inflow rate at each point before resection. The growth criterion thus represents the relative increase of the current homogenized blood flow at each macroscale point with respect to the healthy equilibrium state before resection.

We observe that our growth criterion (6.53) is designed to mitigate hyperperfusion by driving growth only at the location where a discrepancy between the current and the preferred flow exists. In other words, growth is activated only if the current local flow rate into the microcirculation exceeds a physiological equilibrium value. In the scope of this work, we assume the physiological equilibrium $\tilde{Q}_{\text{equi}}$ simply as the flow rate into the liver's microcirculation before resection. This choice automatically accounts for potential patient-specific perfusion characteristics of a simulation model that is set up by including patient-specific data such as overall liver geometry or the location of large

vessels.

The growth scaling coefficient k_ϑ is commonly used for preventing unbounded growth and enabling the calibration of a specific growth curve. For the growth scaling coefficient, we choose the following form [25]:

$$k_\vartheta(\vartheta) = k_\vartheta^+ \left[\frac{\vartheta^+ - \vartheta}{\vartheta^+ - 1} \right]^{m_\vartheta^+} . \tag{6.54}$$

It has three well-defined material parameters, which can be adjusted based on experimental data. The parameter ϑ^+ is the limiting value of growth and can be determined based on clinical observations with regard to the maximum size of lobules after growth. The parameter k_ϑ^+ represents the growth speed, which allows calibration of the growth model with respect to time. Additionally, the parameter m_ϑ^+ allows the adjustment of the nonlinearity of the growth process.

6.3.6 Calibration based on experimental data

Experimentally determined graphs of liver volume regeneration typically show a rapid initial increase in volume due to the high regeneration rate, followed by a slower increase as the resected liver approaches its original volume [89], [95]–[97]. We can now fit the parameters of the growth scaling coefficient (6.54) to match growth curves observed in experimental measurements.

Available data refer to growth of a complete liver, and do not feature local growth in a particular region. We therefore assume that the local growth process with respect to the AV sizes that we will choose for the simulation scenarios in the following does not differ from the growth process averaged over the complete organ. In addition, we make the simplified assumption that during calibration of the growth scaling coefficient, we set the growth criterion $\gamma_g = 1$. By doing so, we treat γ_g as a growth driver that merely indicates whether growth is activated or not, without specifying its intensity in different regions of the liver. This allows us to focus on calibrating the free parameters of the growth scaling function (6.54), so that the overall growth curves produced by the model match the global trends observed in the experimental data available.

In the first step, we set the limiting value of growth $\vartheta^+ = 2.0$ for all examples, as experimental measurements show that the grown lobules can increase to double their original size [162]. In the next step, we conduct a sensitivity study for the remaining two parameters by numerically integrating the evolution equation (6.52) with a simple forward Euler method and a time step $\Delta t = 2$ h. In Fig. 6.10a, we plot the resulting evolution of the growth factor ϑ versus time for different m_ϑ^+ and a fixed $k_\vartheta^+ = 0.01$. We see that the nonlinearity of the growth process is influenced by the parameter m_ϑ^+. In Fig. 6.10b, we plot the evolution of the growth factor for different values of the growth speed k_ϑ^+ and a fixed $m_\vartheta^+ = 1$.

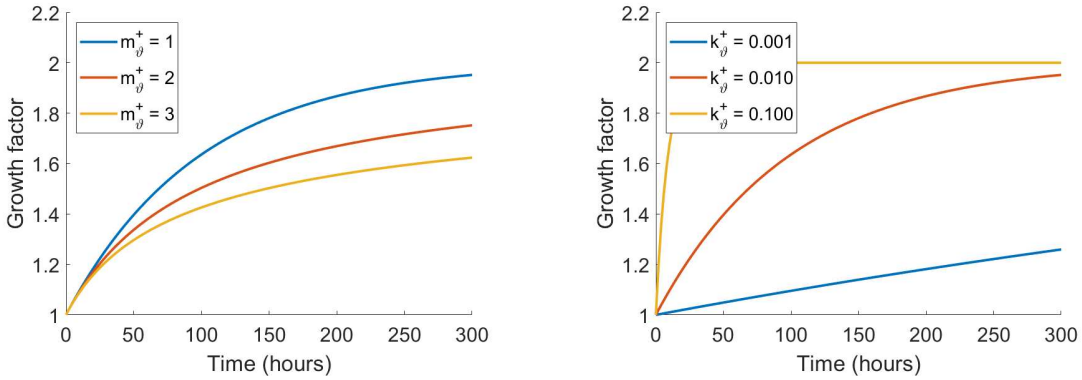

(a) For different nonlinearity parameters m_ϑ^+

(b) For different growth speed parameters k_ϑ^+

Figure 6.10: Evolution of the growth factor ϑ over time.

To calibrate the growth factor, we use the data reported in [95] which comes from experimental measurements conducted on mice. These experiments involved PHx, where 70 % of the liver was surgically removed. The recovery of liver mass over time was monitored, and the remnant liver weight was measured at different time steps to assess the regeneration process (see Fig. 6.11a).

Next, we use the remnant liver weight (mass data) in Fig. 6.11a to determine the corresponding growth factor ϑ, which is defined in equation (6.51) and is directly linked to the mass. The determined growth factor (see blue curve in Fig. 6.11b) ranges between 1.0 and 2.0, where $\vartheta = 1.0$ corresponds to the initial mass (30%) and $\vartheta = 2.0$ corresponds to the fully regenerated liver mass (100%) due to the previously determined limiting value of growth $\vartheta^+ = 2.0$.

Based on this data and the sensitivity study above, we choose the nonlinearity parameter of the growth process to be $m_\vartheta^+ = 1.0$ and the growth speed to be $k_\vartheta^+ = 0.01$. In Fig. 6.11b, we plot the resulting evolution of the modeled growth factor alongside the growth factor derived from the experimental mass data in [95]. We observe a very good fit for our choice of parameters. In addition, we observe that the duration of the growth process of 300 h (12.5 days) also matches clinical data available [95], [96].

6.3.7 Volumetric growth vs. lobular remodeling

According to our discussion in section 2.4, we recall that the central mechanism by which the liver restores lost mass is hepatocyte proliferation, enabling the liver to resume its metabolic, detoxification, and synthetic activities. In addition, liver regeneration also involves changes across the hierarchical vascular tree. Part of the existing vasculature, in particular the smaller vessels in areas where liver growth occurs, must expand to accommodate the increased blood flow. In addition, these vessels undergo remodeling and angiogenesis to guarantee the optimal supply and drainage of the regenerating lobular tissue.

In this work, we focus on a growth model that represents the effect of compensatory

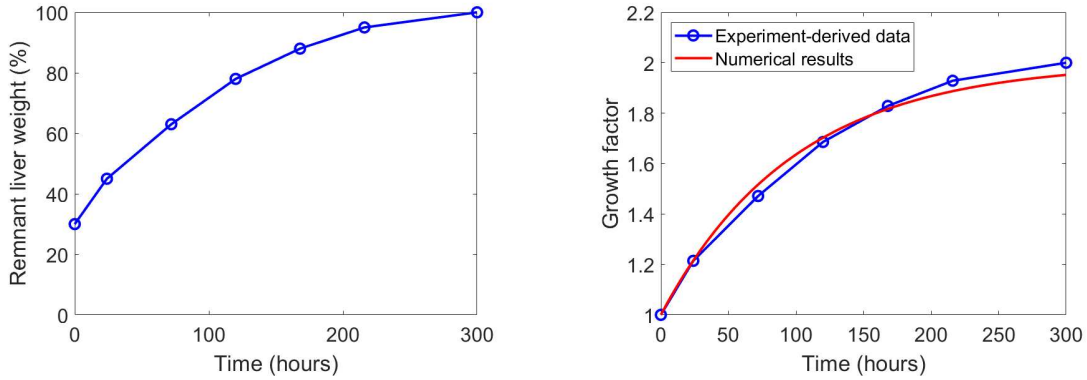

(a) Remnant liver weight recovery reported in [95]

(b) Numerical results vs. experimental-derived data

Figure 6.11: Evolution of the modeled growth factor (numerical results) vs. the growth factor derived from experimental mass data reported in [95].

growth at the lobular level. We do not explicitly incorporate the additional complexity associated with vascular adaptation and angiogenic processes. We assume that the resected vascular trees undergo solely geometric changes rather than changes in their topology when the liver grows. For the largest hierarchy of vessels that we keep fully resolved, we assume that they maintain their supply and drainage activity in the same way as before, essentially scaling up their initial contribution. The higher hierarchies dictate the direction of blood flow and ensure that tissue segments are adequately supplied by the larger branches of the vascular tree. We assume a constant outflow from these upper hierarchies during growth to maintain a consistent fluid distribution into the tissue segments. To achieve this, the vessels must be able to change their diameter and position. Moreover, we assume that the vessels remain straight cylindrical tubes during growth (see Fig. 6.12). This allows the vessels still to be described by the spatial position of the proximal and distal nodes and the new position is determined by the applied deformation field of the tissue.

The medium- and smaller-sized vessels in the intrahepatic branches are homogenized into two compartments for supply and drainage. These vessels also undergo angiogenesis and remodeling to connect new tissue areas with the existing vascular network. These changes improve blood distribution within the liver, ensuring that all regenerating regions receive sufficient nutrients and oxygen, thus maintaining uniform perfusion and supporting efficient metabolic activity across the liver. We assume that these reorganization effects are reflected through geometric updates during homogenization. Geometric changes can be achieved by updating the material parameters of the homogenized model as defined in equations (6.44) and (6.45) using the geometric-related quantities $\mathbf{F}$ and J.

Liver regeneration is a dynamic and multiscale process that occurs over various scales in space and time. Hepatocyte proliferation in the liver lobules begins within hours after liver injury or partial hepatectomy. During the first week, other liver cell types, such as

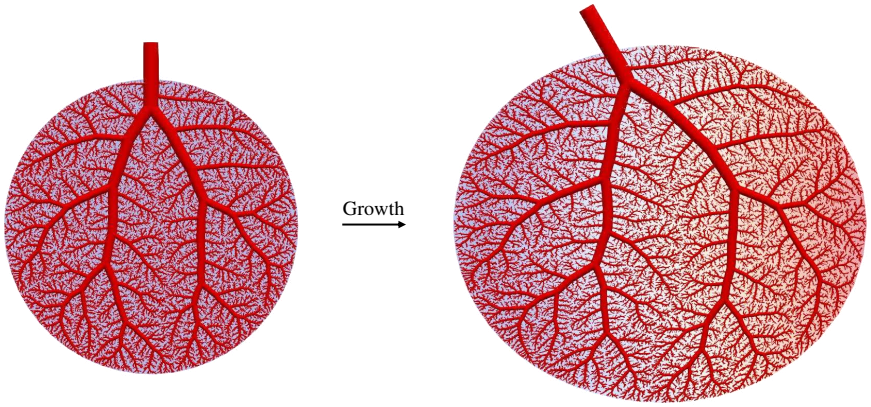

Figure 6.12: Vessel tree in growing medium.

sinusoidal endothelial cells, Kupffer cells, and stellate cells, also start to proliferate and contribute to tissue repair and remodeling at the scale of the microcirculation. Within two weeks, the liver mass significantly increases, often approaching its pre-resection size. After four weeks, most of the hepatocyte proliferation has subsided. The increase in tissue mass requires the remodeling and adjustment of the vascularization, which occurs within three months after liver injury or partial hepatectomy. This stage also includes angiogenesis and the maturation of newly formed vessels, ensuring proper integration of the enlarged liver tissue and the vascular network. Within a year, the stabilization and restoration of the liver's structure and function is complete.

Our growth model focuses on the representation of the effect of compensatory growth at the lobular level that occurs within the first few weeks. Our first key assumption is that we can describe liver growth within this time window by a sequence of quasi-static growth processes, within which we can neglect any time-dependent effects. Therefore, the multiscale perfusion model presented in 6.2 captures the steady-state distribution of blood flow within the tissue, while the finite growth model at the microcirculation accounts for the temporal evolution of tissue growth and therefore involves a time component. By coupling these models, the system is viewed as a sequence of steady-state processes, where at each time stage, the perfusion distribution is assessed in order to drive the growth of the tissue. Please note, that we solely consider compensatory growth in equation (6.52). After the initial phase of regeneration, during which the liver rapidly regrows to compensate for the lost tissue, there may be a period of slower remodeling as the liver undergoes structural changes to optimize its function [79]. The liver may gradually shrink over time once the process of compensatory growth is completed. This process of liver shrinkage typically occurs gradually over a period of weeks to months. Therefore, shrinkage, which is part of the remodeling process and occurs at a larger time scale than the compensatory growth, is not considered in this work.

6.4 Integration of poroelastic growth model within the multi-compartment perfusion model

The final system of equations for the multi-compartment poroelastic growth model takes the form:

$$\mathbf{0} = \nabla_0 \cdot (\mathbf{F}\mathbf{S}) \quad \text{in } \Omega_0, \tag{6.55a}$$

$$\theta_{i,0} = -\nabla_0 \cdot (\mathbf{K}_{i,0} \nabla_0 p_i) + \sum_{k=1}^{N} \beta_{i,k,0}(p_i - p_k) \quad \text{in } \Omega_0, \tag{6.55b}$$

$$\mathbf{S} = 2J_g \mathbf{F}_g^{-1} \frac{\partial \Psi^{\text{skel}}}{\partial \mathbf{C}_e} \mathbf{F}_g^{-T} - J p_{\text{micro}} \mathbf{C}^{-1}, \tag{6.55c}$$

$$p_{\text{micro}} = -\frac{\partial \Psi^{\text{vol}}}{\partial J^s}, \tag{6.55d}$$

$$\mathbf{F} = \mathbf{F}_e \mathbf{F}_g, \quad \mathbf{F}_g = \vartheta \mathbf{I}, \quad \mathbf{C}_e = \mathbf{F}_e^T \mathbf{F}_e, \tag{6.55e}$$

$$\dot{\vartheta}(\mathbf{X}) = \begin{cases} k_\vartheta(\vartheta) \;\; \gamma_g(Q_{\text{supply}}) & \text{for } \gamma_g(Q_{\text{supply}}) > 0, \\ 0 & \text{for } \gamma_g(Q_{\text{supply}}) \leq 0. \end{cases} \tag{6.55f}$$

6.5 Prototypical model problem in 2D

We utilize the same two-dimensional test problem of a circular disk with planar trees described in Section 6.2.4 to study the multi-compartment poroelastic growth model. The only difference is the addition of the poroelastic growth model presented in 6.3, while the rest of the setup (perfusion-related parameters, discretization, supplying and draining tree structures, compartmentalization and homogenization procedure) remains identical to the example above (Section 6.2.4).

Additionally, for the poroelastic growth model, we introduce tissue deformation-related parameters, such as the Young's modulus E and Poisson's ratio ν, which are crucial for describing the mechanical behavior of the tissue during growth. The perfusion-related parameters along with representative liver values of E and ν [144] used for the simulation are listed in Table 6.1. For the contact boundary condition on the outer surface of the circular disk, we require a parameter in the nonlinear stiffness relation (5.2), which we choose as $\alpha = 5 \times 10^{-3}$. This choice is based on the elastic properties of the surrounding organs of the liver, see [145] for details.

Table 6.1: Simulation parameters for the circular disk problem.

Tissue deformation-related parameters	Perfusion-related parameters
Young's modulus $E = 5\ \text{kg mm}^{-1}\ \text{s}^{-2}$	Permeability $K_{\text{micro}} = 1/180\ \text{mm}^3\ \text{s kg}^{-1}$
Poisson's ratio $\nu = 0.35$	Blood viscosity $\eta = 3.6 \times 10^{-6}\ \text{kg mm}^{-1}\ \text{s}^{-1}$

In this study, we select the equilibrium physiological flow $\tilde{Q}_{\text{equi}}$ to be the same as the supply flow, Q_{supply}, illustrated in Fig. 6.8 (a). The solution field Q_{supply} results from

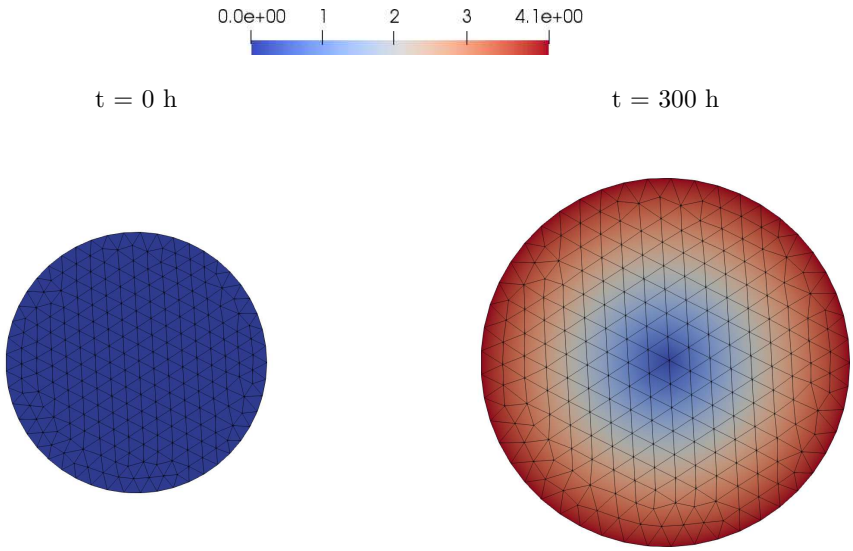

Figure 6.13: Displacement magnitude $\|\mathbf{u}\|$ [mm] for the grown circular disk at time instant t = 300 h. The quantity A_C corresponds to the area of the disk.

the parameters provided in Tab. 4.1, which define the baseline physiological state of the system. To simulate and induce growth within the model, we introduce a perturbation by doubling the flow through the supplying vascular tree. This increase in flow rate serves as a stimulus, pushing the system out of its equilibrium state and mimicking tissue growth driven by hyperperfusion.

We employ the standard Galerkin finite element method [139] to discretize the poroelastic-growth model in the Lagrangian (reference) configuration Ω_0. Multiplication of the momentum equation (6.55a) with discrete test function $\mathbf{v}_h$ and the pressure equation (6.55b) with discrete test function $q_{h,i}$, subsequently integrating over the reference domain Ω_0, and applying integration by parts leads to the weak statement: Find $\mathbf{u}_h \in \mathcal{V}_h$ and $p_{h,i} \in \mathcal{W}_{h,i}$ such that for all $\mathbf{v}_h \in \mathcal{V}_h$ and $q_{h,i} \in \mathcal{W}_{h,i}$:

$$\mathbf{0} = \int_{\Omega_0} (\mathbf{F}_h \mathbf{S}_h) : \nabla_0 \mathbf{v}_h \, \mathrm{d}\Omega_0 + \int_{\Gamma_{N,0}} \zeta \, (\mathbf{u}_h \cdot \mathbf{N}) \, (\mathbf{v}_h \cdot \mathbf{N}) \, \mathrm{d}\Gamma_{N,0}, \tag{6.56}$$

$$\int_{\Omega_0} \theta_{i,0} q_{h,i} \, \mathrm{d}\Omega_0 = \int_{\Omega_0} \left(\mathbf{K}_{i,h,0}(\nabla_0 p_{h,i}) \right) \cdot \left(\nabla_0 q_{h,i} \right) \mathrm{d}\Omega_0 + \ldots$$

$$\ldots + \int_{\Omega_0} q_{h,i} \sum_{k=1}^{N} \beta_{i,k,0} (p_{h,i} - p_{h,k}) \, \mathrm{d}\Omega_0. \tag{6.57}$$

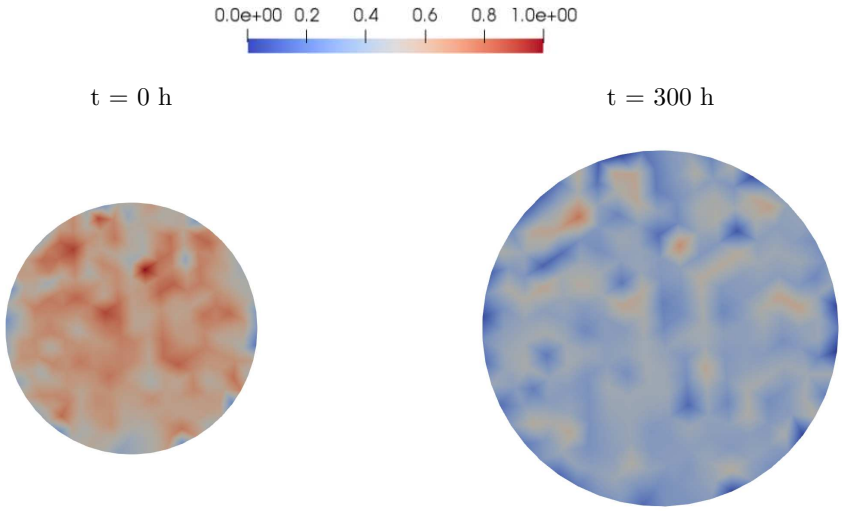

Figure 6.14: Homogenized volumetric flow rate Q_{supply} [s^{-1}] for the grown circular disk at time instant t = 300 h.

The discrete function spaces $\mathcal{V}_h$ and $\mathcal{W}_{h,i}$ consist of linear and quadratic Lagrange basis functions of degree $P = 1$ and $P = 2$, and are applied to discretize the displacements and the pressures, respectively.

We apply a forward Euler method for incremental updates of the growth factor ϑ at each pseudo time step:

$$\vartheta^{n+1} = \vartheta^n + \Delta t\, \dot{\vartheta}^n = \vartheta^n + \Delta t \left[k_\vartheta^+ \left[\frac{\vartheta^+ - \vartheta^n}{\vartheta^+ - 1} \right]^{m_\vartheta^+} \left(\frac{|Q_{\text{supply}}^n| - |\tilde{Q}_{\text{equi}}|}{|\tilde{Q}_{\text{equi}}|} \right) \right]. \tag{6.58}$$

Since the system of equations (6.55) is defined in the reference configuration, the permeability tensors and perfusion coefficients are independent of the time step. We adopt the FEniCS finite element libary in combination with the standard Newton-Raphson method for linearization [140].

We present the growth results of the circular disk in Fig. 6.13. It's evident that the disk undergoes nearly uniform expansion, with no noticeable areas exhibiting disproportionate growth. This aligns with our expectations as the full circular disk receives a uniform blood supply from the vascular network. We also observe that the fully regrown circular disk has doubled in size after 300 hours, which aligns with the fact that we introduced a perturbation by doubling the flow through the supplying vascular tree.

Additionally, we compare the homogenized blood flow rate Q_{supply} of the fully regrown state after 300 hours to the initial state of the circular disk in Fig. 6.14. It is evident that as the disk grows, the blood flow rate becomes more homogeneous and in areas with the highest flow, the intensity decreases. In the following section, we will examine these observations for the liver problem in further detail and perform a statistical analysis.

7 Towards simulation based assessment of liver growth

Liver resection triggers a complex regenerative process that is heavily influenced by the organ's vascular architecture and the redistribution of blood flow. The close relationship between liver regeneration and blood perfusion is well-known, as the liver's highly vascularized nature plays a crucial role in maintaining essential functions like metabolism and detoxification [79].

In the previous sections, we established a multiscale modeling framework for simulating tissue growth and blood flow, which is driven by hyperperfusion. These serve as the basis for the following investigation into liver growth after surgical resection. Therefore, this section focuses on the simulation-based analysis of liver growth in response to a surgical intervention, particularly a partial liver resection.

The primary aim of this section is to apply the simulation-based framework to model and predict liver growth following surgical resection. By integrating a patient-specific liver geometry and vascular architecture, we aim to understand how blood flow redistribution influences the regenerative processes of the liver. Through the calibration of physiological parameters and the simulation of perfusion, this section aims to provide insights into the mechanisms driving liver regeneration, ultimately contributing to improved surgical planning in clinical settings.

In the first part of this section, we detail the patient-specific liver geometry model used in this study, along with the associated vascular geometry. The second part of the section explores simulations of liver perfusion, which are essential for calibrating the parameters of the growth evolution model. In particular, we compare the results of the full and resected liver via a statistical analysis. Finally, we present numerical examples that illustrate liver growth and its temporal evolution following resection.

7.1 Model generation

For the liver geometry, we use the same model as presented in section 5.4.1.

We then generate the vasculature of the liver synthetically as described in Section 4, using the patient-specific liver domain as a boundary and locations of the patient-specific root locations. We emphasize again that we lump the portal vein and the hepatic artery into one supplying tree, as their trees run largely in parallel. Figure 7.1 shows the patient-specific liver domain with the synthetic supplying tree (hepatic artery and portal vein) and the synthetic draining tree (hepatic vein). The generated supplying and draining trees consist of 24,247 and 23,201 terminal vessels, respectively. The underlying parameters for synthetic tree generation are summarized in Table 7.1.

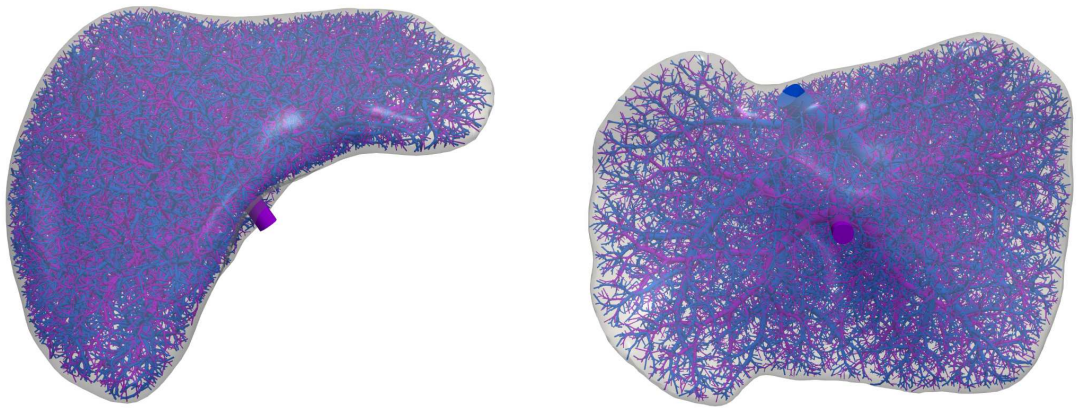

(a) Anterior view (b) Inferior view

Figure 7.1: Patient-specific liver model containing the supplying (purple) and draining (blue) vascular tree structures.

Table 7.1: Model parameters for synthetic tree generation of the liver.

	N_{vessel}	N_{term}	p_{root} $[\frac{\text{kg}}{\text{mm s}}]$	$\hat{Q}_{\text{perf}}$ $[\frac{\text{mm}^3}{\text{s}}]$
Supplying tree	48493	24247	0.17	20000.0
Draining tree	46401	23201	0.0	20000.0

7.2 Model results for liver (hyper-)perfusion

We first focus on simulating liver perfusion in the unresected liver, assuming a healthy state. We divide the synthetic vascular network generated in the previous section into spatially co-existing compartments. To this end, vessels with a radius exceeding 0.5 mm belong to the upper hierarchies that are kept resolved, while those with a radius of 0.5 mm or less are assigned to the lower hierarchies. The compartmentalization of the liver perfusion tree is illustrated in Fig. 7.2. We then generate a finite element mesh, illustrated in Fig. 7.3a, that consists of 16,495 tetrahedral elements. For our multi-compartment model, we use the model parameters, summarized in Tab. 7.2. For the computation of the homogenized material parameters, we choose the radius of the spherical AV to 20 mm.

Table 7.2: Simulation parameters for the liver problem [48], [49], [144].

Tissue deformation-related parameters	Perfusion-related parameters
Young's modulus $E = 5\,\text{kg mm}^{-1}\,\text{s}^{-2}$	Permeability $K_{\text{micro}} = 1/180\,\text{mm}^3\,\text{s kg}^{-1}$
Poisson's ratio $\nu = 0.35$	Blood viscosity $\eta = 3.6 \times 10^{-6}\,\text{kg mm}^{-1}\,\text{s}^{-1}$

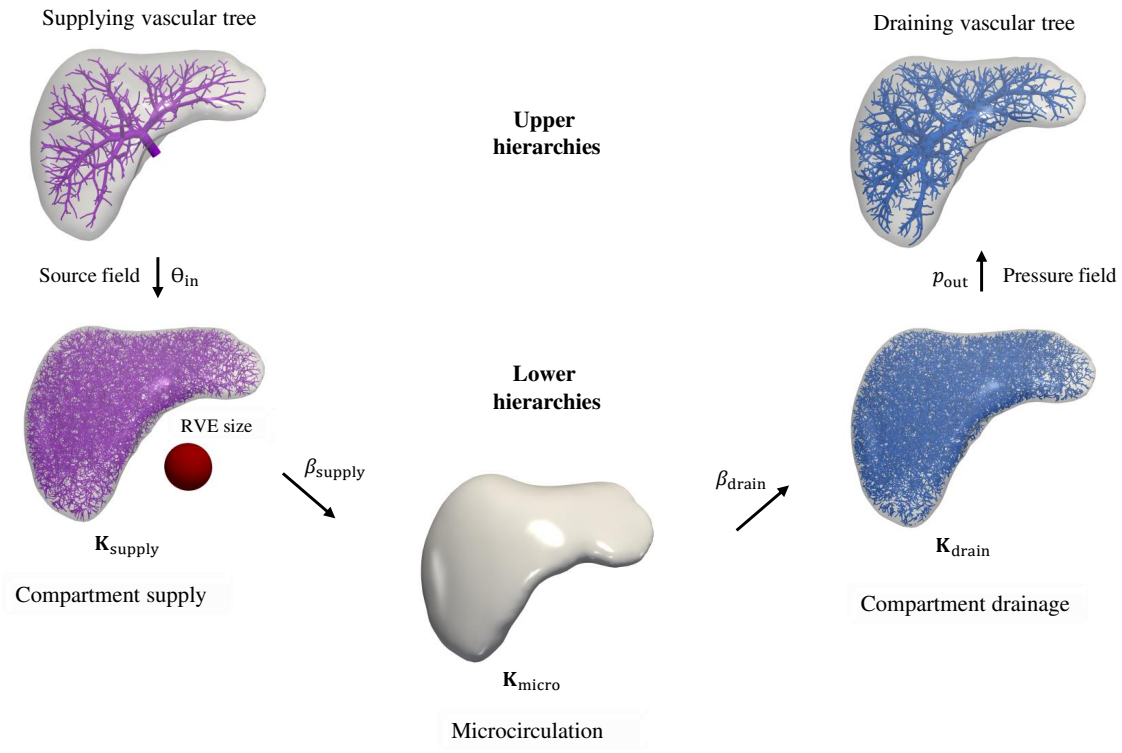

Figure 7.2: Compartmentalization of vascular trees for the liver.

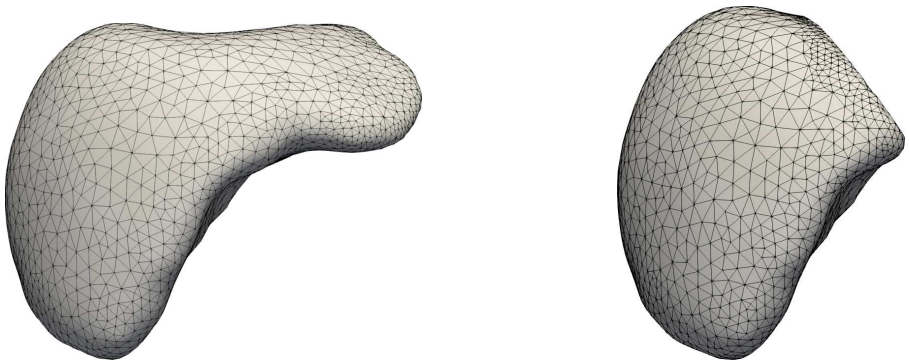

(a) Full liver (b) Resected liver

Figure 7.3: Finite element meshes.

7.2.1 Full liver before resection

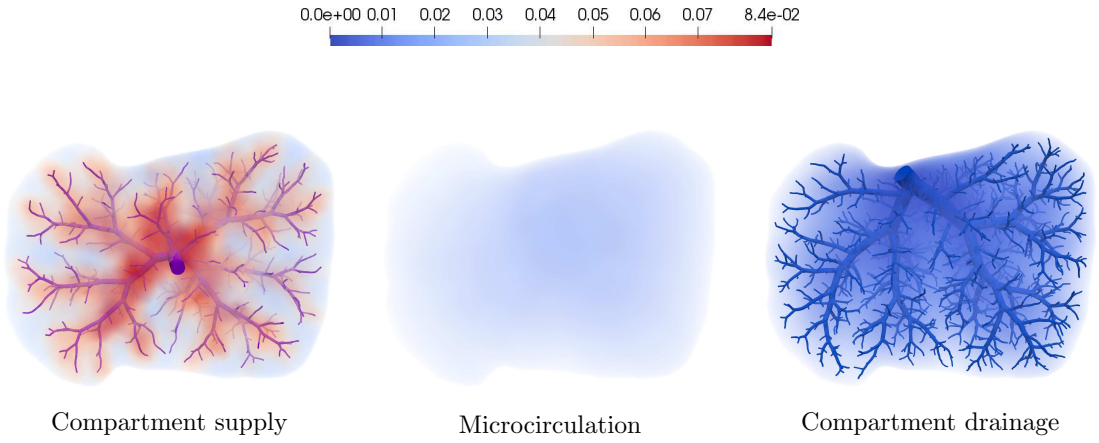

Figure 7.4: Homogenized pressure fields p_i [kg mm^{-1} s^{-2}] of the full liver.

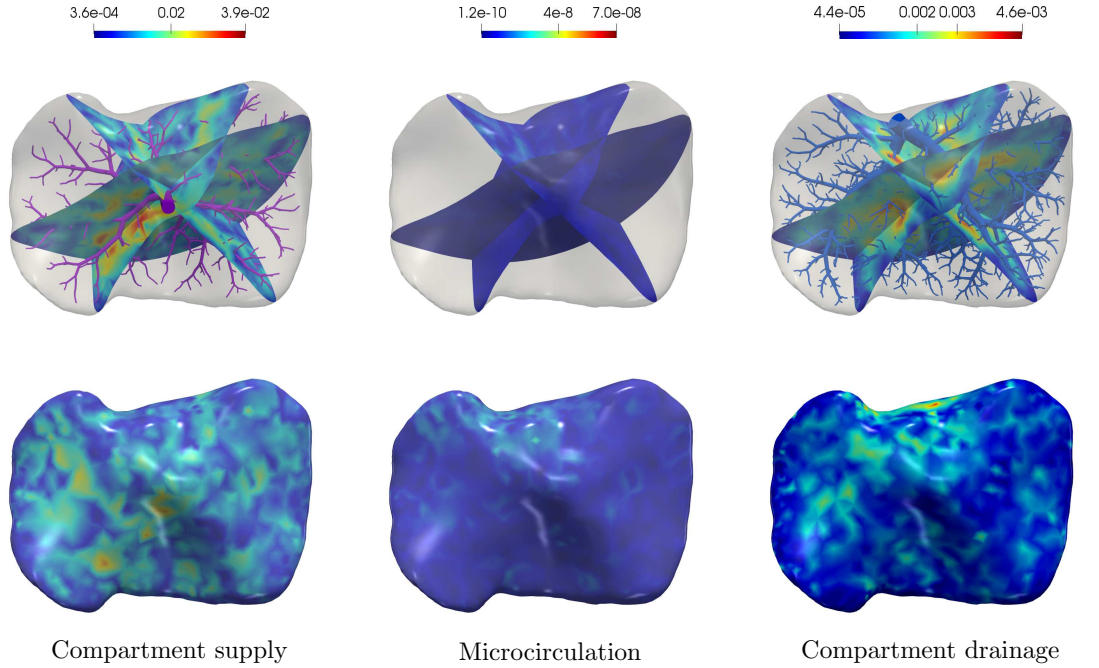

Figure 7.5: Magnitude of the homogenized velocity fields $\|\mathbf{w}_i\|$ [mm s^{-1}] of the full liver.

We first consider the results for the full liver before resection. Figure 7.4 shows the homogenized pressure fields for the compartment supply with the upper hierarchies of the supplying tree, for the microcirculation and for the compartment drainage with the upper hierarchies of the draining tree. We observe that in the compartments supply and

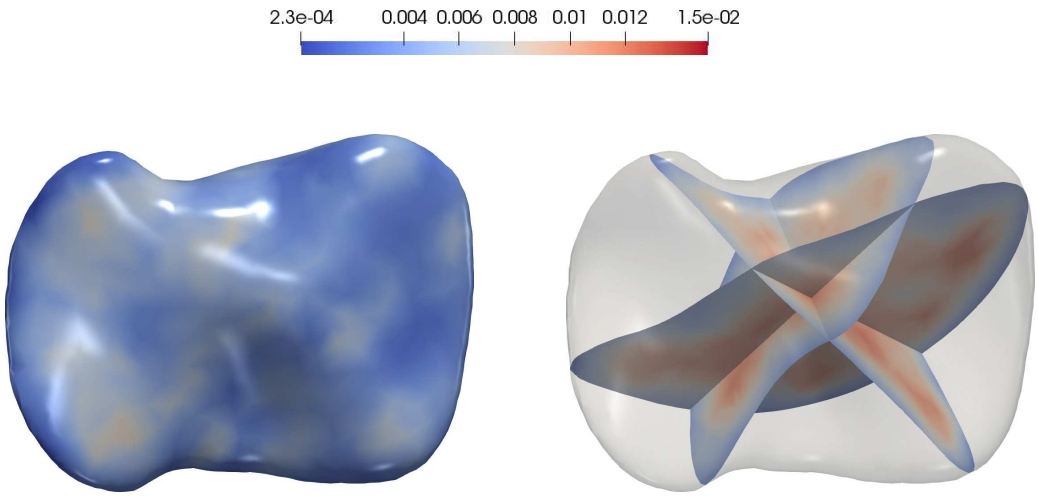

Inferior view View with slices

Figure 7.6: Homogenized volumetric flow rate Q_{supply} [s^{-1}] of the full liver.

drainage, distinct pressure differences along the vessel tree structures are clearly visible, whereas the microcirculation exhibits a much more uniform pressure field.

In Fig. 7.5, we show the corresponding magnitudes of the homogenized velocities. In compartments supply and drainage, we can observe a larger flow along vessel segments of both supplying and draining trees. In the compartment microcirculation, we observe velocity magnitudes that are three to five orders of magnitude lower than those in the compartments supply and drainage. This confirms that the compartment microcirculation connects the compartments supply and drainage by representing the resistance of the sinusoids, and does not redistribute flow across the macroscale domain.

Figure 7.6 shows the homogenized volumetric flow rate density Q_{supply} of the full liver. We can observe an almost uniform blood supply to the liver which is to be expected in a healthy state.

In the following section, we will see that performing a resection will result in significant changes in flow disparities. In particular, we will observe that in the case of the full liver, the blood supply is more homogeneously distributed compared to the resected liver.

7.2.2 Liver after partial resection

We now consider a scenario where a tumor is located in the left lateral section of the liver as illustrated in Fig. 7.7a. The partial resection required to remove the tumor-affected region involves a standard surgical cut that removes liver segments two and three according to the Couinaud classification. The cut also implies cutting the vasculature, and the remaining vascular tree model is shown in Fig. 7.7b. We note that we only plot the "active" vessels that are still connected to the root of the corresponding tree, and remove all orphan vessels that lost this connection. The resected supplying tree now consists of 35,760 vessel segments and 17,857 terminal nodes and the resected draining

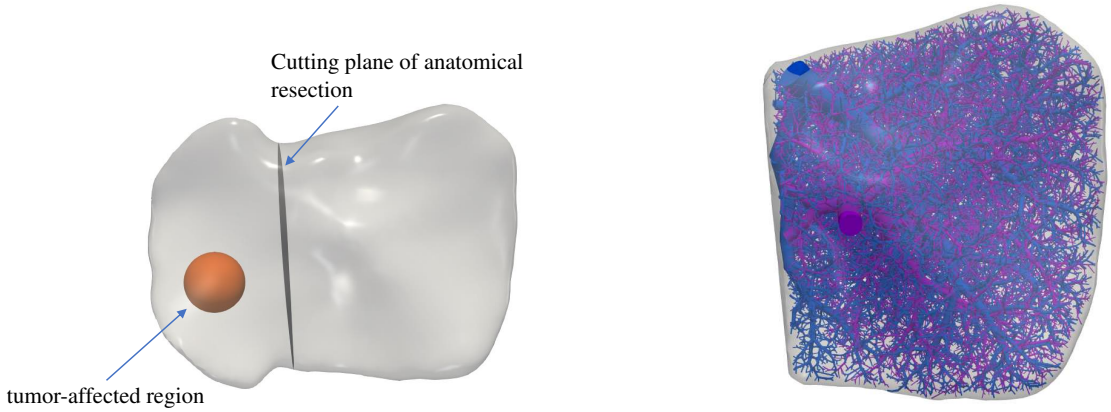

(a) Position of pathology and cutting plane.

(b) Cut synthetic vasculature.

Figure 7.7: Liver geometry and synthetic vasculature after resection (inferior view).

tree consists of 35,362 vessel segments and 17,630 terminal nodes.

Vessels that are cut are sealed during surgery to prevent blood loss. In our simulations, we thus assume that blood flow through any cut segment does not occur. The blood flow associated with cut segments is then redistributed evenly across the remaining portion of the intact tree, in line with our assumptions discussed in Section 6.3.7. We note that after partial resection, the cardiovascular system tries to reduce the overall blood flow rate in the liver by reducing the flow in the hepatic artery. In the scope of the present study, this effect is not considered. The resected liver domain is discretized by a finite element mesh of 14,746 tetrahedral elements, which is illustrated in Fig. 7.3b. The homogenization procedure described above is repeated based on the cut synthetic vasculature and the perfusion simulation is re-run.

Figure 7.8 plots the resulting homogenized volumetric flow rate density of the resected liver before regrowth. On the one hand, we can clearly see a much higher overall flow rate as compared to the results for the full liver in Fig. 7.6. The increased flow rate density represents the state of hyperperfusion, as in our model, the same amount of blood needs to pass through a smaller domain after partial liver resection. On the other hand, we see a significantly lower flow rate density in the bottom left corner. This is due to the existence of orphans in this area that do not receive blood supply. In Fig. 7.7, we can see that in the corresponding region, there are no active vessels of the supplying tree.

7.2.3 Statistical analysis of liver flow rate distributions

In this section, we conduct a statistical analysis to assess the effects of liver resection on the homogenized flow rate Q_{supply} within the liver. The purpose of this analysis is to evaluate how the model represents the impact of the surgical procedure on changes in

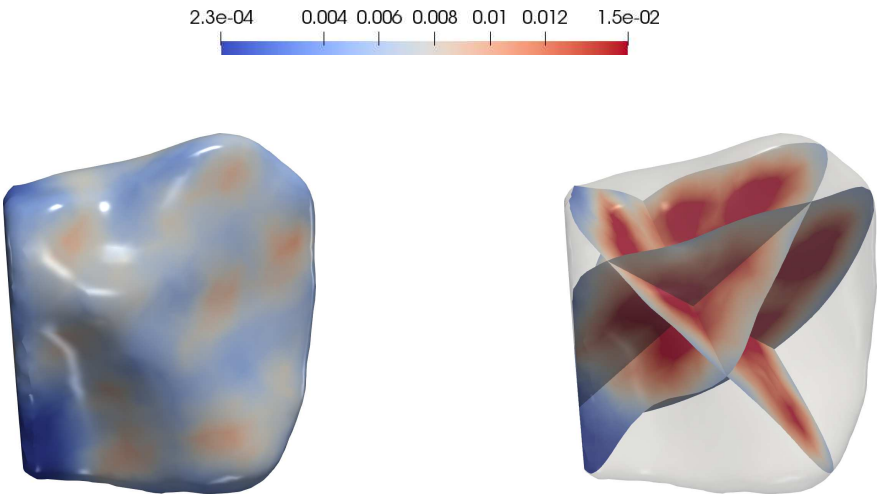

Inferior view View with slices

Figure 7.8: Homogenized volumetric flow rate Q_{supply} [s^{-1}] of the resected liver.

perfusion characteristics.

To this end, we construct histograms to compare the distributions of the homogenized flow rate Q_{supply} before and after partial resection. The histograms, along with the mean, the standard deviation and the coefficient of variation, illustrate the variability of the physical quantities across the liver domain, and how this variability changes after partial resection. By comparing histograms of the full and resected liver, we can identify shifts in the distribution and assess our model's ability to represent hyperperfusion.

For constructing histograms for the full and resected liver, we assume that we have sample data for both cases taken at points that cover each domain sufficiently close to an equal distribution. For simplicity, we choose the nodal points of the two tetrahedral meshes shown in Figs. 7.3a and 7.3b. For both cases, we group the values into the same 75 flow rate bins, which we found suitable to clearly visualize the underlying distribution patterns. To account for the difference in the number of nodes in the two cases, we normalize the frequency in each bin by the total number of nodes multiplied by one hundred, such that the histogram reports the percentage of nodes in each bin.

Using our simulation results for the full and resected liver sampled at the nodes of the corresponding finite element meshes, we arrive at the histograms plotted in Fig. 7.9 for the homogenized volumetric flow rate Q_{supply} of the full liver (in blue) and resected liver (in orange).

The histograms clearly exhibit a marked increase in the mean flow rate in the case of the resected liver, demonstrating the state of hyperperfusion compared to the normal homeostatic conditions in the case of the full liver. We can observe that there is also a significant rise in the variability and dispersion of the blood supply Q_{supply} in the case of the resected liver. The larger standard deviations observed in the histograms of the resected liver suggest a more heterogeneous distribution of homogenized flow rate. This

variability is likely due to the altered flow dynamics and uneven blood supply following the partial resection. Additionally, we notice that the histogram for the resected liver shows an increased concentration of flow values near zero, reflecting the significantly lower flow rate in the bottom left corner and the effect of orphans in the vasculature that practically lead to the inhibition of perfusion.

The results demonstrate that our model is able to represent hyperperfusion as a consequence of partial resection. In addition, they reflect how the surgical procedure disrupts normal perfusion patterns, leading to increased flow variability. The pronounced spread in the data underscores the need for a localized growth criterion to accommodate the hyperperfusion in different regions of the liver when modeling liver regrowth.

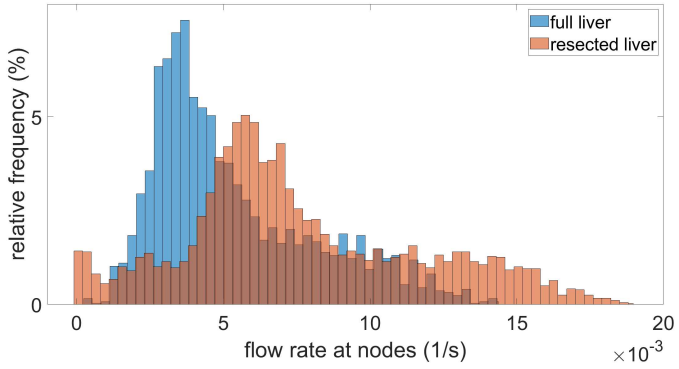

Figure 7.9: Histograms of homogenized volumetric flow rate Q_{supply} [s^{-1}] of the full and resected liver.

7.3 Model results for liver regrowth

In the next step, we focus on the modeling of liver regrowth after partial resection. The results are crucial for understanding how well our modeling framework represents characteristic phenomena associated with liver regeneration at the organ scale. Our growth criterion (6.53) requires a measure for the homeostatic perfusion state, which we have chosen to express via homogenized blood flow inflow rate $\tilde{Q}_{\text{equi}}$ of the full liver before resection. We also set a stiffness parameter, $\alpha = 5 \times 10^{-3}$, for the contact boundary condition on the liver's surface according to the elastic properties of the surrounding organs [145]. Otherwise, we use the same parameters as specified in Section 6.5 and Table 7.2. We integrate with respect to time using a standard explicit forward Euler method with a time step of Δt = 15 hours, up to a final time of t = 300 hours after resection.

Figure 7.10 compares the growing liver, including two selected planes (see Fig. 7.11), at different time instants of the simulated regeneration process. We also state the associated volume of the deformed liver V_L at each time instant. Referring these volumes to the volume of the full liver before resection ($V_L = 2,403,749$ mm^3), we see that directly after resection, the liver is reduced to 77.6% of its original volume, but after 300h has recovered 99.2% of its original volume.

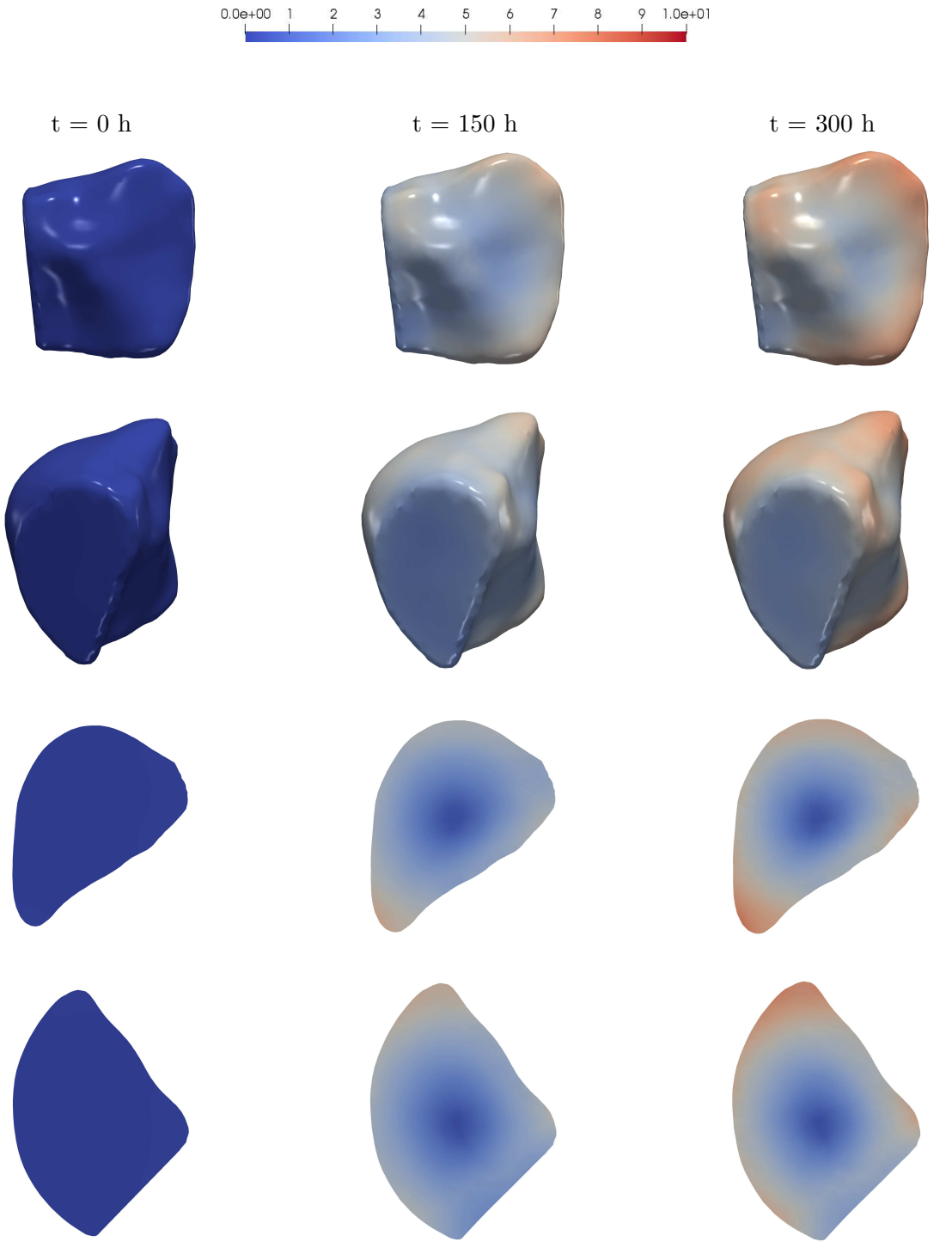

Figure 7.10: Displacement magnitude $\|\mathbf{u}\|$ [mm] of the growing liver at different time instants [h], plotted on the deformed configuration. The quantity V_L corresponds to the current volume of the liver at each time instant.

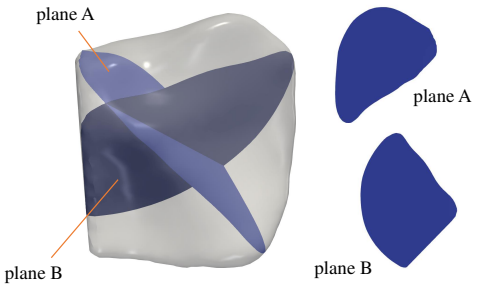

Figure 7.11: Plane sections of the resected liver labeled as plane A and B.

To elucidate this observation further, we first plot the minimum and maximum values, the mean and the standard deviation of the local growth factor, monitored at the nodal points of the finite element mesh during regrowth (see Fig. 7.12). We observe that on average, each volume element of the resected liver eventually increases its volume by a factor of approx. 1.28, which agrees well with the global volume increase from 77.6% to 99.2% of the original volume of the unresected liver. The growth factor, however, ranges from 1.6 (twice the average growth factor) to 1.0 (no growth at all). The minimum growth factor of 1.0 is likely to occur in the bottom left corner, where the flow was observed to be very low (see Fig. 7.8).

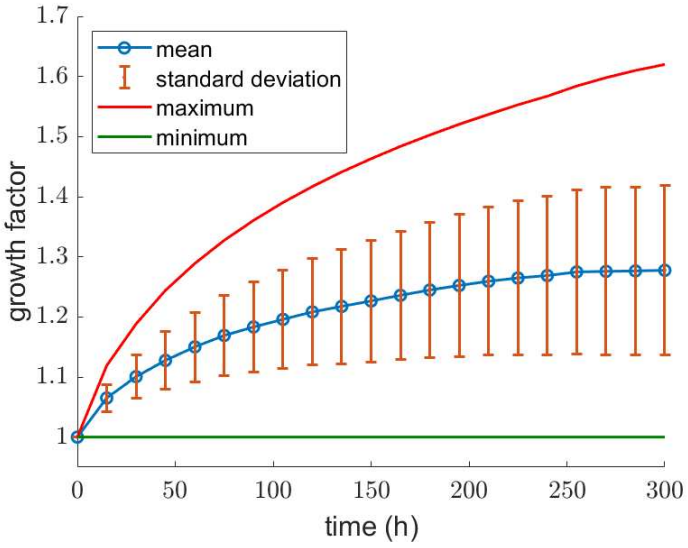

Figure 7.12: Variability of the growth factor ϑ across the growing liver domain over time [h].

Additionally, we compare the homogenized blood flow rate density of the regrown state after 300 hours to the initial state of the resected liver before growth in Fig. 7.13. Comparing these results to the results of the full liver in Fig. 7.6, we observe that the flow rate density reduces over time to the level of the homeostatic state in the unresected

full liver. On the one hand, the intensity of the flow rate decreases in areas that initially experienced the highest increase. On the other hand, the flow rate does not recover in the area where the flow rate dropped due to orphans in the supplying tree.

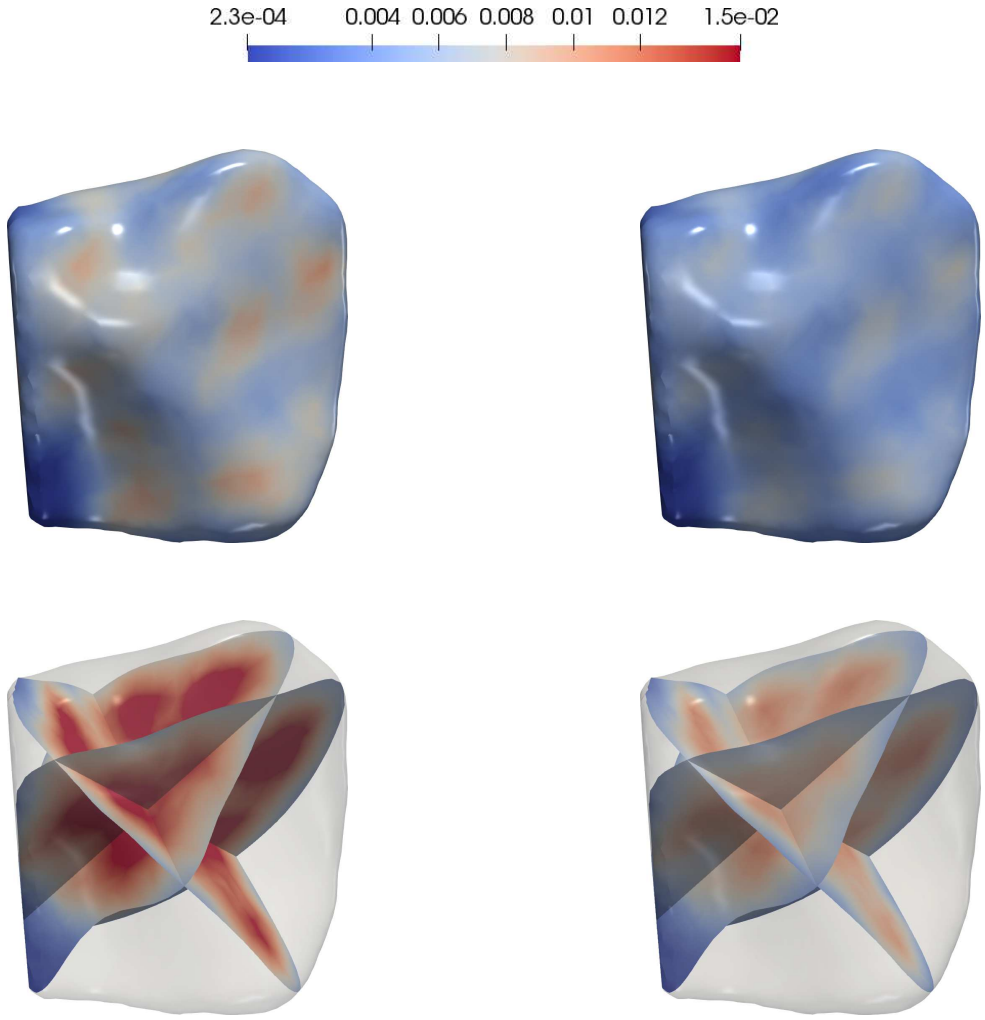

(a) Resected liver

(b) Regrown liver at t = 300 h

Figure 7.13: Homogenized volumetric flow rate Q_{supply} [s^{-1}] of the resected liver and the regrown liver at time instant t = 300 h.

7.3.1 Local hyperperfusion vs. local hypoperfusion

The results reported in the histograms above suggest a pronounced variability in the local perfusion state across the growing liver domain. In particular, they indicate that after resection, we do not only encounter hyperperfusion, but also a reduction of blood flow (hypoperfusion) in some regions of the compartment microcirculation. We would like to further investigate this variation in local perfusion behavior in our liver model, as

it underscores the need for a localized growth criterion. Capturing variations in perfusion during regrowth is likely a key component for potential applications in simulation-based diagnosis and prediction, e.g., for hypoperfusion-driven ischemia.

We first focus on the region in the upper region shown in Fig. 7.13, where the simulated homogenized flow rate density indicates hyperperfusion. To quantify local hyperperfusion, we restrict our selection of nodal points to this region and plot the local variability of the homogenized flow rate density Q_{supply} during regrowth. Figure 7.14 illustrates the local region as well as the flow rate density plots over time.

We observe that on average, the flow rate density decreases from around 0.0095 to 0.0069 s^{-1}, which corresponds inversely to the average growth factor of 1.28 reported in Fig. 7.12 for the complete liver. We also observe a significant variability in the flow rate density in this region, with the maximum value at t = 0 as large as 0.018 s^{-1} and the minimum value as low as 0.005 s^{-1}. This variability results from the variation in permeability and the inhomogeneous distribution of inflow source terms in the multi-compartment model, which both directly reflect properties of the synthetic vascular tree.

It is important to note that all curves - average, minimum and maximum - still exhibit the same relative decrease in flow rate density over time. It is straightforward to infer from our definitions of the evolution equation (6.52) and the growth criterion (6.53) that at the locations of low flow rate density, the homeostatic reference $\tilde{Q}_{\text{equi}}$ in (6.53), taken from the full unresected liver, must have also been low - for instance, due to the existence of a larger resolved vessel at that location. We can therefore conclude that Figure 7.14, including the curve of the minimum value, does not reflect a state of hypoperfusion.

We then focus on the region in the lower left part shown in Fig. 7.13. We repeat the same procedure, illustrated in Fig. 7.14, for this region. We then plot the variability of the local homogenized flow rate density during regrowth in Fig. 7.15. We now observe that only the curve for the maximum value shows a slight decrease over time, while the average and minimum curves remain constant. We therefore infer from (6.52) and (6.53) that the homeostatic reference $\tilde{Q}_{\text{equi}}$ in the unresected liver must have been larger in this region, such that an increase in the growth factor (6.52) is excluded. We can therefore conclude that Figure 7.15 does reflect a state of hypoperfusion, which indicates the existence of orphans in the supplying tree. The plot of the active vasculature in Fig. 7.7b indeed confirms the existence of orphans in this region.

7.3.2 Flow rate variability before, during and after regrowth

The histograms plotted in Figs. 7.16 and 7.17 compare the variability of the homogenized volumetric flow rate Q_{supply} in the resected liver at the beginning of the regrowth process and after 45, 150 and 300 hours (in orange). As the homeostatic reference, we also show again the variability in the full unresected liver (in blue). Table 7.3 also reports the maximum and minimum values, the mean, the standard deviation (SD) and the coefficient of variation (CV) at the beginning and after 45, 150 and 300 hours.

We observe that the mean and the standard deviation of the flow rate density reduces during regeneration. When we compare the histogram of the fully regrown state after 300 hours to the initial state of the full liver, we observe that the regrown liver exhibits

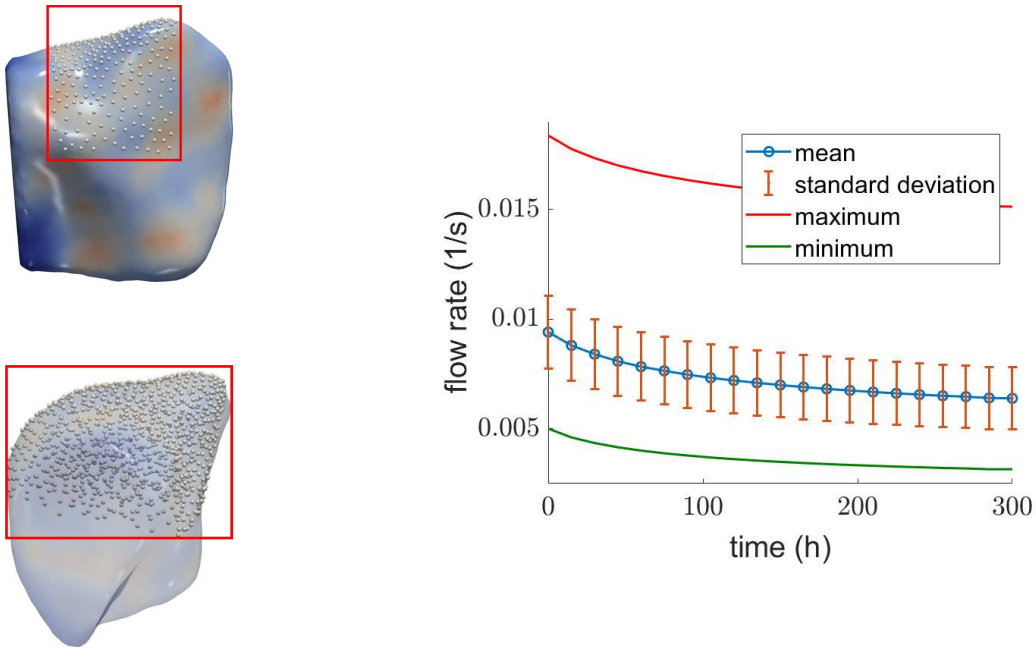

Figure 7.14: Local hyperperfusion: variability of the homogenized volumetric flow rate Q_{supply} [s^{-1}] across the selected region (red box) over time [h]. The white dots show the selected nodal points, where the flow rate density is evaluated.

a flow rate variability and distribution close to the initial homeostatic state. We also see that the minimum flow rate, which is practically zero, remains and does not recover. The slightly increased mean and the slight shift towards larger flow rates in the histogram are likely due to the presence of regions with zero perfusion, which the remaining regions need to compensate for. In general, our results demonstrate again that our model is able to account for the reduction of hyperperfusion towards a homeostatic perfusion state in the regrown liver.

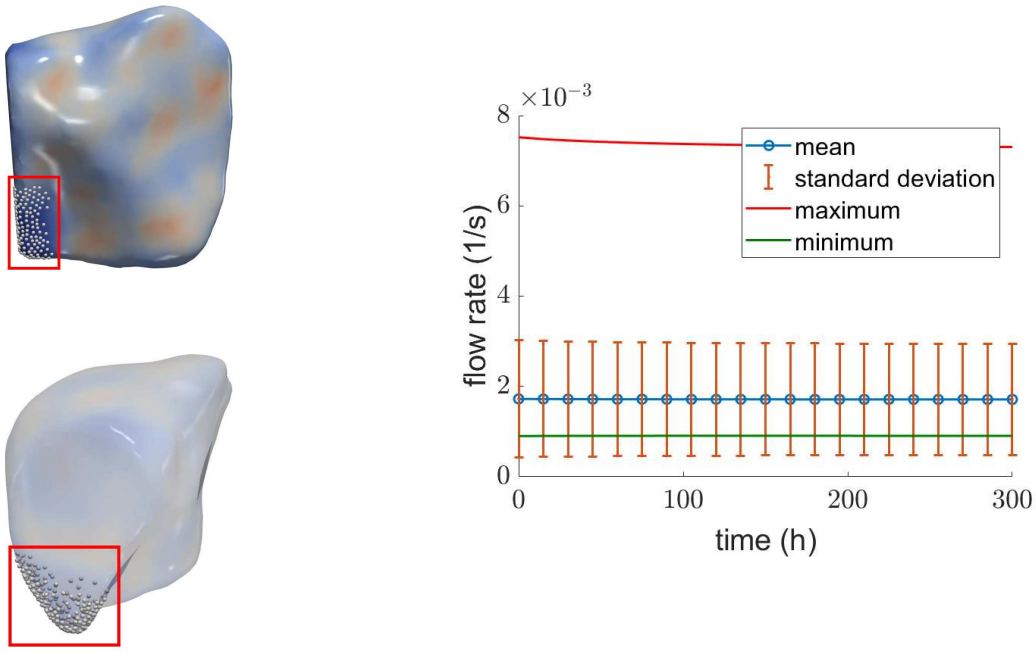

Figure 7.15: Local hypoperfusion: variability of the homogenized volumetric flow rate Q_{supply} [s^{-1}] across the selected region (red box) over time [h]. The white dots show the selected nodal points, where the flow rate density is evaluated.

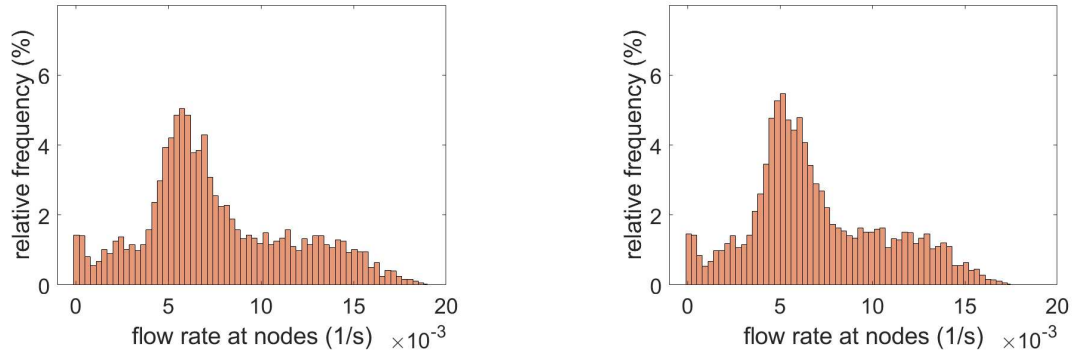

(a) Resected liver at t = 0 h

(b) Regrown liver at t = 45 h

Figure 7.16: Histograms of homogenized volumetric flow rate Q_{supply} [s^{-1}] at the beginning of the regrowth process and after 45 hours.

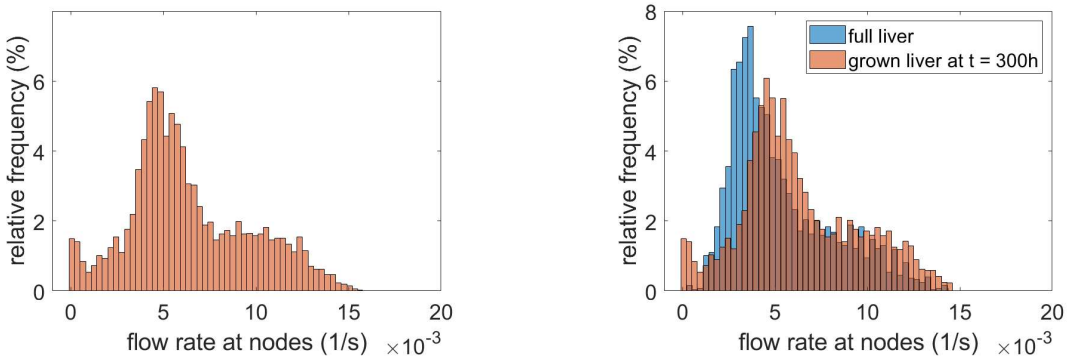

(a) Regrown liver at t = 150 h

(b) Full liver and regrown liver at t = 300 h

Figure 7.17: Histograms of homogenized volumetric flow rate Q_{supply} $[\text{s}^{-1}]$ of the growing liver at time instants t = 150 h and t = 300 h. As a homeostatic reference, we also include the results for the full liver before resection.

Table 7.3: Variability measures for the homogenized volumetric flow rate Q_{supply} at different liver states.

	max. $[\frac{1}{\text{s}}]$	mean $[\frac{1}{\text{s}}]$	min. $[\frac{1}{\text{s}}]$	SD $[\frac{1}{\text{s}}]$	CV
Full liver (homeostatic reference)	$1.44 \cdot 10^{-2}$	$5.36 \cdot 10^{-3}$	$2.32 \cdot 10^{-4}$	$1.91 \cdot 10^{-3}$	0.356
Resected liver	$1.89 \cdot 10^{-2}$	$7.59 \cdot 10^{-3}$	$9.93 \cdot 10^{-9}$	$5.78 \cdot 10^{-3}$	0.762
Regrown liver at t = 45 h	$1.75 \cdot 10^{-2}$	$6.99 \cdot 10^{-3}$	$9.44 \cdot 10^{-9}$	$4.17 \cdot 10^{-3}$	0.597
Regrown liver at t = 150 h	$1.57 \cdot 10^{-2}$	$6.38 \cdot 10^{-3}$	$9.35 \cdot 10^{-9}$	$3.07 \cdot 10^{-3}$	0.481
Regrown liver at t = 300 h	$1.47 \cdot 10^{-2}$	$6.19 \cdot 10^{-3}$	$9.41 \cdot 10^{-9}$	$2.63 \cdot 10^{-3}$	0.425

8 Conclusions and outlook

8.1 Conclusions

In the first part of the thesis (Sections 2-5), we presented a modeling framework that connects continuum poroelasticity and discrete vascular tree structures to model liver tissue in terms of perfusion and deformation. The connection is achieved through a series of modeling assumptions and decisions. Firstly, we used bell-shaped functions as source terms in the pressure equation to impose inflow at the interfaces of the terminal vessels of the supplying tree and the poroelastic domain. Secondly, we introduced void regions that model the interface between the terminal vessels of the draining tree and the poroelastic domain, where pressure boundary conditions could be applied accordingly. The rationale behind this approach to draining vessels is rooted in establishing boundary conditions that mimic physical behavior. The most intuitive way to achieve this is by applying a reference pressure as a Dirichlet boundary condition. Implementing a Dirichlet condition necessitates a boundary, which led to the introduction of voids. Obviously, the primary drawback is the required computational discretization effort, which would be significantly less in the absence of these voids.

Additionally, we took into account contact with surrounding tissue, using nonlinear springs at the boundary of the poroelastic domain. We demonstrated the numerical behavior and versatility of our modeling framework via a poroelastic circular disc connected to planar trees. We performed a series of sensitivity studies to test the model behavior with respect to source term parameters, stiff and soft contact and hierarchical tree depth.

We then investigated our modeling framework for a liver problem that consisted of two different resection scenarios of a patient-specific liver geometry. We used a patient-specific liver geometry model based on imaging data obtained from CT scans. The vessel trees themselves are not patient-specific in the sense that they are segmented directly from imaging data. However, they have a patient-specific component in its connection to the geometry. We then computed the flow redistribution after the two different cuts. As expected, the numerical results indicate a difference in blood supply for the two resection scenarios, in which the anatomically resected liver performed satisfactorily and the non-anatomically resected liver exhibited parts with insufficient blood supply. Regardless of the depth we choose for the tree structure, an observable relative difference in pressure and flow is always present. The main purpose of the model, however, is to visualize changes in perfusion at the organ scale, e.g. due to resections. This does not qualitatively change when increasing the number of vessels. The current number seems appropriate to assess redistributed flow and pressure disparities on a global organ scale. The model is not intended to depict a physiological response with respect to

local perfusion characteristics, metabolism or any other physiological function. It is also evident that the finer the tree is, the more homogeneous the pressure and flow fields become. Of course, the quantitative results of framework would change when adopting a finer tree (and computational mesh).

In summary, our results demonstrate that the combination of poromechanics and synthetic vascular trees can be a useful tool for modeling liver perfusion and constitutes a first step towards assessing the redistributed flow characteristics after a liver resection. Our results demonstrate that the framework has the potential of a first step towards guiding suitable cut patterns for liver resection surgery. In this approach, we incorporate different length scales from the vascular trees and the lobule scale. Indeed, we agree that, from a physiological point of view, one usually considers these scales separately. However, in this framework, the relative pressure and flow differences play a major role. It should be noted that the model does not cover further processes in the liver, e.g. growth or metabolism. Moreover, the model is not intended to depict local effects concerning perfusion but instead captures perfusion characteristics regarding redistributed flow. It offers a better visualization of perfusion changes on the organ scale, e.g. due to resection. Although a robust validation study with clinical data is still lacking, we can already observe that the presented approach has the potential to aid in assessing and optimizing different surgical resection scenarios regarding the perfusion.

Furthermore, deformation and stresses play an important role in the further development towards modeling liver regrowth after surgical resection. This is the reason for adopting a poroelastic model rather than a porous medium model; mechanical behavior of the tissue is indispensable.

At the end of Section 5, we performed a critical assessment of the modeling framework, highlighting its limitations. While the framework successfully connects continuum poroelasticity and discrete vascular trees to simulate liver perfusion and deformation, several challenges emerged. One key issue is the introduction of voids required for applying Dirichlet boundary conditions on the draining vessels, which significantly increases computational complexity and cost due to intricate meshing. This limits the feasibility of large-scale, patient-specific simulations when extending this framework with a growth model. Additionally, the model's current representation of lower vascular tree levels does not fully capture their distinct physiological behaviors, necessitating more advanced modeling approaches. This led to the development of a new multiscale modeling framework, which was discussed and applied in subsequent sections.

In the second part of the thesis (Sections 6 and 7) we presented a novel framework for modeling liver regrowth on the organ scale. It combines the following three main model components:

(A) *a multiscale perfusion model* that combines synthetic vascular tree generation with a multi-compartment homogenized flow model, including a homogenization procedure to obtain effective permeabilities and intercompartmental perfusion coefficients from the lower hierarchies of the synthetic tree structure.

(B) *a poroelastic finite growth model* that is defined in the compartment microcirculation, but acts also on the other compartments and the synthetic vascular tree

structure by transfer of the resulting finite kinematics.

(C) *an evolution equation* for the local volumetric growth factor, driven by the homogenized flow rate density into the compartment microcirculation that we identified as a measure for local hyperperfusion.

Unlike the previous approach, the new model eliminates the need for voids and accounts for the distinct characteristics of the vascular system across different scales, improving both accuracy and computational efficiency.

Our framework is based on a series of modeling assumptions and interpretations. The most important are summarized here:

(1) We assumed that the hierarchical vascular structures of the liver can be approximated by straight vessel segments, where blood is a Newtonian fluid and Poiseuille's law holds. We then synthesized the vascular tree structure of the liver via non-intersecting directed graphs that minimize a combination of the metabolic demand and the hydrodynamic resistance [16]. We combined the vascular trees of the portal vein and the hepatic artery into one synthetic supplying tree.

(2) We divided the synthetic supplying and draining trees in larger vessel segments that are kept resolved, and smaller vessel segments that are replaced by two homogenized flow compartments, one for the lower hierarchies of the supplying tree and one for the lower hierarchies of the draining tree. We used the smaller vessel segments to find compartmental permeability and intercompartmental perfusion coefficients via a homogenization procedure, based on a scale separation of one order of magnitude between macroscale (full organ), representative averaging volume, and radii of the vessels to be homogenized.

(3) We assumed that the compartments supply and drainage are connected via a compartment microcirculation, whose permeability represents the resistance of the capillary network of sinusoids at the microscale. The compartments supply and drainage are coupled to the outlets of the resolved vessel segments via suitably calibrated source and sink terms in the continuity equation.

(4) The characteristic time scale of our regrowth model formulated in the compartment microcirculation is days. We therefore describe liver regrowth by a sequence of quasi-static growth processes. We also assumed that liver regrowth can be regarded as isotropic from a macroscopic viewpoint.

(5) We assumed that we can keep the same porosity during regrowth. Hence, the growth factor is not only applied to the tissue skeleton, but also to the perfusing blood, representing the added mass of the blood that occupies additional sinusoid space.

(6) We postulated a phenomenological link between the evolution equation for the growth factor, representing volumetric growth, and the inflow rate density into the compartment microcirculation, measuring (hyper-)perfusion. We then proposed a

growth criterion that represents the relative increase of the current homogenized blood flow at each macroscale point with respect to the (supposedly healthy) homeostatic state before resection in the same liver. This homeostatic reference automatically accounts for potential individual perfusion characteristics in a patient-specific simulation model.

(7) For the largest vessels of the resected vascular tree structure, we assumed that remodeling solely involves adaptations in length and position. Furthermore, their supply and drainage activity is scaled up after resection via a corresponding change in diameter (vasodilation). For medium- and smaller-sized vessels homogenized in the compartments supply and drainage, we assumed that remodeling is reflected through geometric updates of the homogenized permeability and perfusion coefficients. At the capillary level, we assumed that remodeling is effective instantly, so that the resistance of the sinusoid network in terms of the permeability in the compartment microcirculation always corresponds to the same (healthy) tissue.

We calibrated our regrowth model with experimental liver data, adjusting parameters for the growth speed, nonlinearity, and maximum growth factor, to match observed liver volume regeneration curves. We then applied the resulting modeling framework to a full-scale patient-specific liver example, for which we assumed a common surgical resection cut. The cut also involved orphan vessels that lose their connection to the root of the supplying tree and hence inducing local insufficient blood supply of the microcirculation (hypoperfusion). We conducted finite element simulations of the perfusion behavior of the unresected full liver and the regeneration of the resected liver, with a focus on how well our modeling framework represents characteristic phenomena at the organ scale.

We observed that the resection reduced our example liver to 77.6% of its original volume, but after 300h it recovered to 99.2%. The overall regrowth dynamics of our model thus corresponds well with common clinical observations. We furthermore observed that the homogenized flow rate density significantly increased after resection and reduced over time to the level of the the homeostatic state in the unresected full liver. These results demonstrate that our model is able to represent hyperperfusion as a consequence of partial resection and to account for the reduction of hyperperfusion towards a homeostatic perfusion state in the regrown liver.

Furthermore, the simulation results suggest a pronounced variability in the local perfusion state across the growing liver domain, demonstrated via histograms and distribution parameters. The growth factor observed ranges from 1.6 (twice the average) to 1.0 (no growth at all), the homogenized flow rate density from 0.018 to 0.001 s^{-1}. Hence, we do not only capture hyperperfusion, but also the expected local hypoperfusion in the vicinity of the orphan vessels. Capturing variations in perfusion during regrowth is likely a key component for potential applications in simulation-based diagnosis and prediction, e.g., for hypoperfusion-driven ischemia or for the preoperative identification of suitable cut patterns for partial liver resection. These observations emphasize the need for a localized growth criterion such as the one proposed in this work.

8.2 Potential impact in the broader field of computational biomechanics

The development and application of the proposed modeling framework for liver perfusion and regrowth hold potential impacts across several domains.

The ability to predict how different surgical resection scenarios affect liver perfusion and subsequent regrowth can enhance clinical decision-making. By providing insights into the redistribution of blood flow and its influence on tissue growth, the model could guide surgeons in planning resection strategies that optimize blood supply and support effective liver regrowth. This could lead to more precise and individualized surgical approaches, improving patient outcomes and reducing complications associated with inadequate perfusion.

The framework's ability to simulate changes in liver perfusion and tissue growth could also be utilized for postoperative monitoring. By comparing simulated outcomes with real-time clinical data, surgeons could better assess the effectiveness of surgical interventions and adjust treatment plans accordingly. This could lead to improved monitoring protocols and more responsive care, enhancing patient recovery and reducing the risk of postoperative complications.

The hyperperfusion-driven liver growth model provides a framework for further investigating liver regeneration processes. Extending this framework to include physiological responses (e.g. considering metabolism, liver functions, pathological changes) could facilitate research into the mechanisms underlying liver regrowth, helping to identify factors that promote or hinder regeneration. Insights gained from such research could lead to new therapeutic strategies for liver diseases.

The integration of synthetic vascular trees and a compartmentalized perfusion model with continuum poroelasticity growth represents an advancement in computational modeling. The techniques developed in this framework could be adapted and applied to other biological tissues or complex physiological systems. This interdisciplinary approach could drive further progress in the field of computational biomechanics and tissue engineering, contributing to a broader understanding of tissue mechanics in health and disease.

8.3 Future work

The current model offers a framework for understanding liver perfusion and hyperperfusion-driven tissue regrowth but leaves several areas for further research and refinement. Here are some key areas for future exploration:

- **Integration of liver functions and pathological changes**: While our model provides insights into perfusion and growth dynamics, it does not account for liver functions, metabolism, or pathological changes, as this is beyond the scope of this work and is not essential for the current application. However, future investigations could integrate these aspects into the model to capture a more comprehensive understanding of liver regeneration processes. One approach to achieve this could involve the integration of ODEs that incorporate various risk factors associated

with postoperative liver failure. Incorporating these aspects is essential in advancing the proposed model towards a more evidence-based physiological simulation tool suitable in clinical practice. For example, including metabolic activity could enhance predictions of liver regeneration in the context of different metabolic conditions or diseases.

- **Parameter sensitivity analysis:** To better understand the impact of parameter variations on model outcomes, a detailed sensitivity analysis (e.g. for the multi-compartment model) is needed. This may involve systematically varying model parameters (RVE size, number of compartments, separation criterion for macroscopic and microscopic vasculature) to identify how changes affect predictions of liver regrowth and perfusion. Such analyzes will help in identifying critical factors influencing liver recovery and guide more accurate model calibration.

- **Personalization and validation:** The current model would benefit from further personalization to reflect individual patient characteristics more accurately. This includes refining material parameters such as elasticity, permeability, and porosity based on patient-specific data. At the current stage of development of our modeling framework, comprehensive validation studies against experimental and clinical data have not been conducted yet, but constitute a crucial next step. For the current model, our plans include the monitoring of tissue growth rates and changes in the vascular system, based on available experimental and clinical CT data [163]. We also plan to assess our results in comparison with existing simpler ODE-based regrowth models [3], [96].

- **Refinement of growth model:** The current approach assumes isotropic growth, but liver regrowth may exhibit anisotropic behavior. Future research could explore anisotropic growth models to provide a possibly more realistic representation of liver regeneration. This involves defining preferred directions for growth based on local mechanical or biological factors.

- **Incorporation of a lobule-level perfusion model:** Extending our current framework to include a liver lobule-level perfusion model can offer more accurate predictions at the microscale. Incorporating an efficient reduced-order model for simulating blood perfusion in liver lobules as introduced in [55] into our framework could refine the representation of microcirculation and improve the overall multi-scale predictions of liver perfusion. Specifically, the perfusion characteristics, such as flow fields, from the supply and drainage compartments in our current compartmentalized model could serve as inputs to the lobule model. This would enhance the coupling between the macroscale vascular tree structures and microscale lobule dynamics, allowing for more physiologically accurate predictions of flow distribution and liver function during regeneration.

Bibliography

[1] F. Bray, J. Ferlay, I. Soerjomataram, R. L. Siegel, L. A. Torre, and A. Jemal, "Global cancer statistics 2018: Globocan estimates of incidence and mortality worldwide for 36 cancers in 185 countries," *CA Cancer J. Clin.*, vol. 68, no. 6, pp. 394–424, 2018.

[2] R. I. Macias, M. J. Monte, M. A. Serrano, J. M. González-Santiago, I. Martín-Arribas, A. L. Simão, and J. J. Marin, "Impact of aging on primary liver cancer: Epidemiology, pathogenesis and therapeutics," *Aging (Albany NY)*, vol. 13, no. 19, p. 23 416, 2021.

[3] B. Christ, U. Dahmen, K. H. Herrmann, M. König, J. R. Reichenbach, T. Ricken, and N. Waschinsky, "Computational modeling in liver surgery," *Front. Physiol.*, vol. 8, p. 906, 2017.

[4] C. Debbaut, "Multi-level modelling of hepatic perfusion in support of liver transplantation strategies," Ph.D. dissertation, Ghent University, 2013.

[5] W. Schreiner and P. F. Buxbaum, "Computer-optimization of vascular trees," *IEEE Trans. Biomed. Eng.*, vol. 40, no. 5, pp. 482–491, 1993.

[6] R. Karch, F. Neumann, M. Neumann, and W. Schreiner, "A three-dimensional model for arterial tree representation, generated by constrained constructive optimization," *Comput. Biol. Med.*, vol. 29, no. 1, pp. 19–38, 1999.

[7] L. O. Schwen and T. Preusser, "Analysis and algorithmic generation of hepatic vascular systems," *Int. J. Hepatol.*, 2012.

[8] A. A. Guy, A. W. Justin, D. M. Aguilar-Garza, and A. E. Markaki, "3d printable vascular networks generated by accelerated constrained constructive optimization for tissue engineering," *IEEE Trans. Biomed. Eng.*, vol. 67, no. 6, pp. 1650–1663, 2019.

[9] Z. A. Sexton, A. R. Hudson, J. E. Herrmann, D. J. Shiwarski, J. Pham, J. M. Szafron, S. M. Wu, M. Skylar-Scott, A. W. Feinberg, and A. Marsden, "Rapid model-guided design of organ-scale synthetic vasculature for biomanufacturing," *Preprint: https://arxiv.org/abs/2308.07586v1*, 2023.

[10] C. D. Murray, "The physiological principle of minimum work: I. the vascular system and the cost of blood volume," *Proc. Natl. Acad. Sci.*, vol. 12, no. 3, pp. 207–214, 1926.

[11] L. O. Schwen, W. Wei, F. Gremse, J. Ehling, L. Wang, U. Dahmen, and T. Preusser, "Algorithmically generated rodent hepatic vascular trees in arbitrary detail," *J. Theor. Biol.*, vol. 365, pp. 289–300, 2015.

[12] C. Jaquet, L. Najman, H. Talbot, L. Grady, M. Schaap, B. Spain, H. J. Kim, I. Vignon-Clementel, and C. A. Taylor, "Generation of patient-specific cardiac vascular networks: A hybrid image-based and synthetic geometric model," *IEEE Trans. Biomed. Eng.*, vol. 66, no. 4, pp. 946–955, 2018.

[13] G. D. M. Talou, S. Safaei, P. J. Hunter, and P. J. Blanco, "Adaptive constrained constructive optimisation for complex vascularisation processes," *Sci. Rep.*, vol. 11, no. 1, p. 6180, 2021.

[14] E. Jessen, M. C. Steinbach, C. Debbaut, and D. Schillinger, "Rigorous mathematical optimization of synthetic hepatic vascular trees," *J. R. Soc. Interface*, vol. 19, no. 191, p. 20 220 087, 2022.

[15] E. Jessen, M. C. Steinbach, C. Debbaut, and D. Schillinger, "Branching exponents of synthetic vascular trees under different optimality principles," *IEEE Trans. Biomed. Eng.*, vol. 71, no. 4, pp. 1345–1354, 2023.

[16] E. Jessen, M. C. Steinbach, and D. Schillinger, "Optimizing non-intersecting synthetic vascular trees in nonconvex organs," *Preprint: https://arxiv.org/abs/2410.06002*, 2024.

[17] E. Rohan, V. Lukeš, and A. Jonášová, "Modeling of the contrast-enhanced perfusion test in liver based on the multi-compartment flow in porous media," *J. Math. Biol.*, vol. 77, no. 2, pp. 421–454, 2018.

[18] C. Debbaut, D. Monbaliu, C. Casteleyn, P. Cornillie, D. Van Loo, B. Masschaele, and P. Segers, "From vascular corrosion cast to electrical analog model for the study of human liver hemodynamics and perfusion," *IEEE Trans. Biomed. Eng.*, vol. 58, no. 1, pp. 25–35, 2010.

[19] S. K. Stoter, P. Müller, L. Cicalese, M. Tuveri, D. Schillinger, and T. J. Hughes, "A diffuse interface method for the navier–stokes/darcy equations: Perfusion profile for a patient-specific human liver based on mri scans," *Comput. Methods Appl. Mech. Eng.*, vol. 321, pp. 70–102, 2017.

[20] E. R. Hyde, C. Michler, J. Lee, A. N. Cookson, R. Chabiniok, D. A. Nordsletten, and N. P. Smith, "Parameterisation of multi-scale continuum perfusion models from discrete vascular networks," *Med. Biol. Eng. Comput.*, vol. 51, pp. 557–570, 2013.

[21] A. N. Cookson, J. Lee, C. Michler, R. Chabiniok, E. Hyde, D. A. Nordsletten, and N. P. Smith, "A novel porous mechanical framework for modelling the interaction between coronary perfusion and myocardial mechanics," *J. Biomech.*, vol. 45, no. 5, pp. 850–855, 2012.

[22] C. Michler, A. N. Cookson, R. Chabiniok, E. Hyde, J. Lee, M. Sinclair, and N. P. Smith, "A computationally efficient framework for the simulation of cardiac perfusion using a multi-compartment darcy porous-media flow model," *Int. J. Numer. Method. Biomed. Eng.*, vol. 29, no. 2, pp. 217–232, 2013.

[23] E. K. Rodriguez, A. Hoger, and A. D. McCulloch, "Stress-dependent finite growth in soft elastic tissues," *J. Biomech.*, vol. 27, no. 4, pp. 455–467, 1994.

[24] D. Ambrosi, G. A. Ateshian, E. M. Arruda, S. C. Cowin, J. Dumais, A. Goriely, and K. Garikipati, "Perspectives on biological growth and remodeling," *J. Mech. Phys. Solids*, vol. 59, no. 4, pp. 863–883, 2011.

[25] V. A. Lubarda and A. Hoger, "On the mechanics of solids with a growing mass," *Int. J. Solids Struct.*, vol. 39, no. 18, pp. 4627–4664, 2002.

[26] A. Menzel and E. Kuhl, "Frontiers in growth and remodeling," *Mech. Res. Commun.*, vol. 42, pp. 1–14, 2012.

[27] E. Kuhl, "Growing matter: A review of growth in living systems," *J. Mech. Behav. Biomed. Mater.*, vol. 29, pp. 529–543, 2014.

[28] K. Garikipati, E. M. Arruda, K. Grosh, H. Narayanan, and S. Calve, "A continuum treatment of growth in biological tissue: The coupling of mass transport and mechanics," *J. Mech. Phys. Solids*, vol. 52, no. 7, pp. 1595–1625, 2004.

[29] G. W. Jones and S. J. Chapman, "Modeling growth in biological materials," *SIAM Rev.*, vol. 54, no. 1, pp. 52–118, 2012.

[30] C. J. Cyron and J. D. Humphrey, "Growth and remodeling of load-bearing biological soft tissues," *Meccanica*, vol. 52, pp. 645–664, 2017.

[31] D. Ambrosi, M. Ben Amar, C. J. Cyron, A. DeSimone, A. Goriely, J. D. Humphrey, and E. Kuhl, "Growth and remodelling of living tissues: Perspectives, challenges and opportunities," *J. R. Soc. Interface*, vol. 16, no. 157, p. 20 190 233, 2019.

[32] W. Kroon, T. Delhaas, T. Arts, and P. Bovendeerd, "Computational modeling of volumetric soft tissue growth: Application to the cardiac left ventricle," *Biomech. Model. Mechanobio.*, vol. 8, pp. 309–310, 2009.

[33] S. Göktepe, O. J. Abilez, and E. Kuhl, "A generic approach towards finite growth with examples of athlete's heart, cardiac dilation, and cardiac wall thickening," *J. Mech. Phys. Solids*, vol. 58, pp. 1661–1680, 2010.

[34] S. Göktepe, S. N. S. Acharya, J. Wong, and E. Kuhl, "Computational modeling of passive myocardium," *Int. J. Numer. Methods Biomed. Eng.*, vol. 27, pp. 1–12, 2011.

[35] S. Budday, T. C. Ovaert, G. A. Holzapfel, P. Steinmann, and E. Kuhl, "Fifty shades of brain: A review on the mechanical testing and modeling of brain tissue," *Arch. Comput. Methods Eng.*, vol. 27, pp. 1187–1230, 2020.

[36] S. Budday, P. Steinmann, and E. Kuhl, "The role of mechanics during brain development," *J. Mech. Phys. Solids*, vol. 72, pp. 75–92, 2014.

[37] D. Ambrosi and F. Mollica, "On the mechanics of a growing tumor," *Int. J. Eng. Sci.*, vol. 40, pp. 1297–1316, 2002.

[38] E. Kuhl, R. Maas, G. Himpel, and A. Menzel, "Computational modeling of arterial wall growth: Attempts towards patient-specific simulations based on computer tomography," *Biomechan. Model. Mechanobiol.*, vol. 6, pp. 321–331, 2007.

[39] S. Sankaran, J. D. Humphrey, and A. L. Marsden, "An efficient framework for optimization and parameter sensitivity analysis in arterial growth and remodeling computations," *Comput. Methods Appl. Mech. Eng.*, vol. 256, pp. 200–210, 2013.

[40] E. L. Schwarz, M. R. Pfaller, J. M. Szafron, M. Latorre, S. E. Lindsey, C. K. Breuer, J. D. Humphrey, and A. L. Marsden, "A fluid–solid-growth solver for cardiovascular modeling," *Comput. Methods Appl. Mech. Eng.*, vol. 417, p. 116 312, 2023.

[41] A. B. Ramachandra, J. D. Humphrey, and A. L. Marsden, "Gradual loading ameliorates maladaptation in computational simulations of vein graft growth and remodelling," *J. R. Soc. Interface*, vol. 14, no. 130, p. 20 160 995, 2017.

[42] K. N. Yamamoto, M. Ishii, Y. Inoue, F. Hirokawa, B. D. MacArthur, A. Nakamura, and K. Uchiyama, "Prediction of postoperative liver regeneration from clinical information using a data-led mathematical model," *Sci. Rep.*, vol. 6, no. 1, p. 34 214, 2016.

[43] Y. K. Shestopaloff and I. F. Sbalzarini, "A method for modeling growth of organs and transplants based on the general growth law: Application to the liver in dogs and humans," *PLoS One*, vol. 9, no. 6, e99275, 2014.

[44] V. Periwal, J. R. Gaillard, L. Needleman, and C. Doria, "Mathematical model of liver regeneration in human live donors," *J. Cell. Physiol.*, vol. 229, no. 5, pp. 599–606, 2014.

[45] D. Cook, B. A. Ogunnaike, and R. Vadigepalli, "Systems analysis of non-parenchymal cell modulation of liver repair across multiple regeneration modes," *BMC Syst. Biol.*, vol. 9, pp. 1–24, 2015.

[46] S. Lorente, M. Hautefeuille, and A. Sanchez-Cedillo, "The liver, a functionalized vascular structure," *Sci. Rep.*, vol. 10, no. 1, p. 16 194, 2020.

[47] A. Bonfiglio, K. Leungchavaphongse, R. Repetto, and J. H. Siggers, "Mathematical modeling of the circulation in the liver lobule," *J. Biomech. Eng.*, vol. 132, p. 111 011, 2010.

[48] C. Debbaut, J. Vierendeels, C. Casteleyn, P. Cornillie, D. Van Loo, P. Simoens, and P. Segers, "Perfusion characteristics of the human hepatic microcirculation based on three-dimensional reconstructions and computational fluid dynamic analysis," *J. Biomech. Eng.*, vol. 134, no. 1, p. 011 003, 2012.

[49] C. Debbaut, J. Vierendeels, J. H. Siggers, R. Repetto, D. Monbaliu, and P. Segers, "A 3d porous media liver lobule model: The importance of vascular septa and anisotropic permeability for homogeneous perfusion," *Comput. Methods Biomech. Biomed. Engin.*, vol. 17, no. 12, pp. 1295–1310, 2014.

[50] T. Ricken, D. Werner, H. G. Holzhütter, M. König, U. Dahmen, and O. Dirsch, "Modeling function–perfusion behavior in liver lobules including tissue, blood, glucose, lactate and glycogen by use of a coupled two-scale pde–ode approach," *Biomech. Model. Mechanobiol.*, vol. 14, pp. 515–536, 2015.

[51] L. Lambers, N. Waschinsky, J. Schleicher, M. König, H. M. Tautenhahn, M. Albadry, and T. Ricken, "Quantifying fat zonation in liver lobules: An integrated multiscale in silico model combining disturbed microperfusion and fat metabolism via a continuum biomechanical bi-scale, tri-phasic approach," *Biomech. Model. Mechanobiol.*, pp. 1–23, 2024.

[52] L. Lambers, "Multiscale and multiphase modeling and numerical simulation of function-perfusion processes in the liver," Ph.D. dissertation, Universität Stuttgart, 2023.

[53] N. Waschinsky, D. Werner, T. Ricken, U. Dahmen, and O. Dirsch, "On a bi-scale and tri-phasic model for the description of growth in biological tissue using the example of the human liver," *PAMM*, vol. 16, no. 1, pp. 109–110, 2016.

[54] T. Ricken, U. Dahmen, and O. Dirsch, "A biphasic model for sinusoidal liver perfusion remodeling after outflow obstruction," *Biomech. Model. Mechanobiol.*, vol. 9, pp. 435–450, 2010.

[55] A. A. Siddiqui, E. Jessen, S. K. F. Stoter, D. Néron, and D. Schillinger, "Reduced order modeling of blood perfusion in parametric multipatch liver lobules," *Preprint: https://www.researchsquare.com/article/rs-3906153/v1*, 2024.

[56] B. J. Binder, K. A. Landman, M. J. Simpson, M. Mariani, and D. F. Newgreen, "Modeling proliferative tissue growth: A general approach and an avian case study," *Phys. Rev. E.*, vol. 78, no. 3, p. 031 912, 2008.

[57] P. Adhyapok, X. Fu, J. P. Sluka, S. G. Clendenon, V. D. Sluka, Z. Wang, and J. A. Glazier, "A computational model of liver tissue damage and repair," *PLoS One*, vol. 15, no. 12, e0243451, 2020.

[58] P. Van Liedekerke, M. M. Palm, N. Jagiella, and D. Drasdo, "Simulating tissue mechanics with agent-based models: Concepts, perspectives and some novel results," *Comput. Part. Mech.*, vol. 2, pp. 401–444, 2015.

[59] D. Drasdo, S. Hoehme, and M. Block, "On the role of physics in the growth and pattern formation of multi-cellular systems: What can we learn from individual-cell based models?" *J. Stat. Phys.*, vol. 128, pp. 287–345, 2007.

[60] J. M. Osborne, A. Walter, S. K. Kershaw, G. R. Mirams, A. G. Fletcher, P. Pathmanathan, D. Gavaghan, O. E. Jensen, P. K. Maini, and H. M. Byrne, "A hybrid approach to multi-scale modelling of cancer," *Philos. Transact. A Math. Phys. Eng. Sci.*, vol. 368, no. 1930, pp. 5013–5028, 2010.

[61] A. Ghallab, M. Myllys, C. H. Holland, A. Zaza, W. Murad, R. Hassan, Y. A. Ahmed, T. Abbas, E. A. Abdelrahim, K. M. Schneider, *et al.*, "Influence of liver fibrosis on lobular zonation," *Cells*, vol. 8, no. 12, p. 1556, 2019.

[62] H. Byrne and D. Drasdo, "Individual-based and continuum models of growing cell populations: A comparison," *J. Math. Biol.*, vol. 58, pp. 657–687, 2009.

[63] S. Höhme, J. G. Hengstler, M. Brulport, M. Schäfer, A. Bauer, R. Gebhardt, and D. Drasdo, "Mathematical modelling of liver regeneration after intoxication with ccl4," *Chem. Biol. Interact.*, vol. 168, no. 1, pp. 74–93, 2007.

[64] D. Drasdo and S. Höhme, "A single-cell-based model of tumor growth in vitro: Monolayers and spheroids," *Phys. Biol.*, vol. 2, no. 3, p. 133, 2005.

[65] S. Hoehme, M. Brulport, A. Bauer, E. Bedawy, W. Schormann, M. Hermes, V. Puppe, R. Gebhardt, S. Zellmer, M. Schwarz, *et al.*, "Prediction and validation of cell alignment along microvessels as order principle to restore tissue architecture in liver regeneration," *Proc. Natl. Acad. Sci.*, vol. 107, no. 23, pp. 10 371–10 376, 2010.

[66] M. König, S. Bulik, and H. G. Holzhütter, "Quantifying the contribution of the liver to glucose homeostasis: A detailed kinetic model of human hepatic glucose metabolism," *PLoS Comput. Biol.*, vol. 8, no. 6, e1002577, 2012.

[67] M. Radszuweit, M. Block, J. G. Hengstler, E. Schöll, and D. Drasdo, "Comparing the growth kinetics of cell populations in two and three dimensions," *Phys. Rev. E*, vol. 79, no. 5, p. 051 907, 2009.

[68] D. Drasdo, R. Kree, and J. S. McCaskill, "Monte carlo approach to tissue-cell populations," *Phys. Rev. E*, vol. 52, no. 6, p. 6635, 1995.

[69] A. Ebrahem, E. Jessen, M. F. ten Eikelder, T. Gangwar, M. Mika, and D. Schillinger, "Connecting continuum poroelasticity with discrete synthetic vascular trees for modelling liver tissue," *Proc. R. Soc. A*, vol. 480, no. 2285, p. 20 230 421, 2024.

[70] A. Ebrahem, J. Hohl, E. Jessen, M. F. P. ten Eikelder, and D. Schillinger, "A multiscale-multiphysics framework for modeling organ-scale liver regrowth," *Preprint: https://arxiv.org/abs/2410.19529*, 2024.

[71] J. Hohl, A. Ebrahem, E. Jessen, M. F. P. ten Eikelder, and D. Schillinger, "A multi-compartment perfusion model of blood flow through deformed hierarchical vessel networks," *In preparation*, 2024.

[72] T. Roskams, V. J. Desmet, and C. Verslype, "Development, structure and function of the liver," *MacSween's Pathology of the Liver*, pp. 1–72, 2007.

[73] S. Lorente, M. Hautefeuille, and A. Sanchez-Cedillo, "The liver, a functionalized vascular structure," *Sci. Rep.*, vol. 10, p. 16 194, 2020.

[74] A. W. Paulsen, "Hepatic anatomy, physiology and assessment of hepatic function," *Transplantation of the liver. Philadelphia: Saunders*, pp. 43–64, 1996.

[75] U. Frevert, S. Engelmann, S. Zougbédé, J. Stange, B. Ng, K. Matuschewski, and H. Yee, "Intravital observation of plasmodium berghei sporozoite infection of the liver," *PLoS Biol.*, vol. 3, no. 6, e192, 2005.

[76] C. Debbaut, P. Segers, P. Cornillie, C. Casteleyn, M. Dierick, W. Laleman, and D. Monbaliu, "Analyzing the human liver vascular architecture by combining vascular corrosion casting and micro-ct scanning: A feasibility study," *J. Anat.*, vol. 224, pp. 509–517, 2014.

[77] S. T. Orcutt and D. A. Anaya, "Liver resection and surgical strategies for management of primary liver cancer," *Cancer control*, vol. 25, no. 1, p. 1 073 274 817 744 621, 2018.

[78] K. T. Nguyen, T. C. Gamblin, and D. A. Geller, "World review of laparoscopic liver resection—2,804 patients," *Ann. Surg.*, vol. 250, no. 5, pp. 831–841, 2009.

[79] G. K. Michalopoulos, "Liver regeneration," *J. Cell. Physiol.*, vol. 213, no. 2, pp. 286–300, 2007.

[80] G. K. Michalopoulos and B. Bhushan, "Liver regeneration: Biological and pathological mechanisms and implications," *Nat. Rev. Gastroenterol. Hepatol.*, vol. 18, no. 1, pp. 40–55, 2021.

[81] E. Vibert, T. Perniceni, H. Levard, C. Denet, N. K. Shahri, and B. Gayet, "Laparoscopic liver resection," *Br. J. Surg.*, vol. 93, no. 1, pp. 67–72, 2006.

[82] Y. M. Wu, R. H. Hu, H. S. Lai, and P. H. Lee, "Robotic-assisted minimally invasive liver resection," *Asian J. Surg.*, vol. 37, no. 2, pp. 53–57, 2014.

[83] N. Bhardwaj, A. D. Strickland, F. Ahmad, A. R. Dennison, and D. M. Lloyd, "Liver ablation techniques: A review," *Surg. Endosc.*, vol. 24, pp. 254–265, 2010.

[84] J. Yamanaka, S. Saito, and J. Fujimoto, "Impact of preoperative planning using virtual segmental volumetry on liver resection for hepatocellular carcinoma," *World J. Surg.*, vol. 31, pp. 1251–1257, 2007.

[85] J. Savikko, M. Ilmakunnas, H. Mäkisalo, A. Nordin, and H. Isoniemi, "Enhanced recovery protocol after liver resection," *Br. J. Surg.*, vol. 102, no. 12, pp. 1526–1532, 2015.

[86] P. B. S. Lai, K. F. Lee, J. Wong, and A. K. C. Li, "Techniques for liver resection: A review," *The Surgeon*, vol. 5, no. 3, pp. 166–174, 2007.

[87] E. Vibert, T. Perniceni, H. Levard, C. Denet, N. K. Shahri, and B. Gayet, "Laparoscopic liver resection," *Br. J. Surg.*, vol. 93, pp. 67–72, 2006.

[88] S. T. Orcutt, K. Kobayashi, M. Sultenfuss, B. S. Hailey, A. Sparks, B. Satpathy, and D. A. Anaya, "Portal vein embolization as an oncosurgical strategy prior to major hepatic resection: Anatomic, surgical, and technical considerations," *Front. Surg.*, vol. 3, p. 14, 2016.

[89] N. Hohmann, W. Weiwei, U. Dahmen, O. Dirsch, A. Deutsch, and A. Voss-Böhme, "How does a single cell know when the liver has reached its correct size?" *PLoS One*, vol. 9, no. 4, e93207, 2014.

[90] K. Abshagen, C. Eipel, and B. Vollmar, "A critical appraisal of the hemodynamic signal driving liver regeneration," *Langenbeck's Arch. Surg*, vol. 397, pp. 579–590, 2012.

[91] Y. Wu, N. Li, X. Shu, W. Li, X. Zhang, D. Lü, and M. Long, "Biomechanics in liver regeneration after partial hepatectomy," *Front. bioeng. biotechnol.*, vol. 11, p. 1 165 651, 2023.

[92] L. Lorenz, J. Axnick, T. Buschmann, C. Henning, S. Urner, S. Fang, H. Nurmi, N. Eichhorst, R. Holtmeier, K. Bodis, *et al.*, "Mechanosensing by β1 integrin induces angiocrine signals for liver growth and survival," *Nat.*, vol. 562, no. 7725, pp. 128–132, 2018.

[93] L. Große-Segerath and E. Lammert, "Role of vasodilation in liver regeneration and health," *Biol. Chem.*, vol. 402, no. 9, pp. 1009–1019, 2021.

[94] N. Fausto, J. S. Campbell, and K. J. Riehle, "Liver regeneration," *Hepatol.*, vol. 43, no. S1, S45–S53, 2006.

[95] K. Nishiyama, H. Nakashima, M. Ikarashi, M. Kinoshita, M. Nakashima, S. Aosasa, and J. Yamamoto, "Mouse cd11b+ kupffer cells recruited from bone marrow accelerate liver regeneration after partial hepatectomy," *PLoS One*, vol. 10, no. 9, e0136774, 2015.

[96] L. A. Furchtgott, C. C. Chow, and V. Periwal, "A model of liver regeneration," *Biophys. J.*, vol. 96, no. 10, pp. 3926–3935, 2009.

[97] L. G. Koniaris, I. H. McKillop, S. I. Schwartz, and T. A. Zimmers, "Liver regeneration," *J. Am. Coll. Surg.*, vol. 197, no. 4, pp. 634–659, 2003.

[98] R. T. Stravitz and W. M. Lee, "Acute liver failure," *The Lancet*, vol. 394, no. 10201, pp. 869–881, 2019.

[99] T. Schreckenbach, J. Liese, W. O. Bechstein, and C. Moench, "Posthepatectomy liver failure," *Dig. Surg.*, vol. 29, no. 1, pp. 79–85, 2012.

[100] K. Shirabe, M. Shimada, T. Gion, H. Hasegawa, K. Takenaka, T. Utsunomiya, and K. Sugimachi, "Postoperative liver failure after major hepatic resection for hepatocellular carcinoma in the modern era with special reference to remnant liver volume," *J. Am. Coll. Surg.*, vol. 188, no. 3, pp. 304–309, 1999.

[101] S. C. Kou, C. S. Poon, and M. Etxeberria, "Residue strength, water absorption and pore size distributions of recycled aggregate concrete after exposure to elevated temperatures," *Cement Concrete Compos.*, vol. 53, pp. 73–82, 2014.

[102] J. W. Veldsink, R. M. J. Van Damme, G. Versteeg, and W. P. M. Van Swaaij, "The use of the dusty-gas model for the description of mass transport with chemical reaction in porous media," *Biochem. Eng. J.*, vol. 57, no. 2, pp. 115–125, 1995.

[103] F. J. Leij, T. A. Ghezzehei, and D. Or, "Modeling the dynamics of the soil pore-size distribution," *Soil Till. Res.*, vol. 64, pp. 61–78, 2002.

[104] S. Avramidis, P. Englezos, and T. Papathanasiou, "Dynamic nonisothermal transport in hygroscopic porous media: Moisture diffusion in wood," *AIChE J.*, vol. 38, pp. 1279–1287, 1992.

[105] F. Concha and D. E. Hurtado, "Upscaling the poroelastic behavior of the lung parenchyma: A finite-deformation micromechanical model," *J. Mech. Phys. Solids*, vol. 145, p. 104 147, 2020.

[106] R. de Boer and W. Ehlers, "On the problem of fluid-and gas-filled elasto-plastic solids," *Int. J. Solids Struct.*, vol. 22, pp. 1231–1242, 1986.

[107] O. Coussy, "Thermomechanics of saturated porous solids in finite deformation," *Eur. J. Mech. A/Solids*, vol. 8, pp. 1–14, 1989.

[108] A. Gajo, "A general approach to isothermal hyperelastic modelling of saturated porous media at finite strains with compressible solid constituents," *Proc. Roy. Soc. A Math. Phys. Eng. Sci.*, vol. 466, pp. 3061–3087, 2010.

[109] M. Wang, S. Liu, Z. Xu, K. Qu, M. Li, X. Chen, Q. Xue, G. M. Genin, T. J. Lu, and F. Xu, "Characterizing poroelasticity of biological tissues by spherical indentation: An improved theory for large relaxation," *J. Mech. Phys. Solids*, vol. 138, p. 103 920, 2020.

[110] T. D. Le, C. Moyne, M. A. Murad, and S. A. Lima, "A two-scale non-local model of swelling porous media incorporating ion size correlation effects," *J. Mech. Phys. Solids*, vol. 61, no. 12, pp. 2493–2521, 2013.

[111] B. Markert, "A constitutive approach to 3-d nonlinear fluid flow through finite deformable porous continua," *Transp. Porous Media*, vol. 70, no. 3, pp. 427–450, 2007.

[112] K. Terzaghi, *Theoretical Soil Mechanics*. New York: Wiley, 1943.

[113] M. A. Biot, "Theory of propagation of elastic waves in a fluid saturated porous solid. ii higher frequency range," *J. Acoust. Soc. Am.*, vol. 28, pp. 179–191, 1956.

[114] M. A. Biot, "Theory of finite deformations of porous solids," *Indiana Univ. Math. J.*, vol. 21, no. 7, pp. 597–620, 1972.

[115] D. Chapelle, J. F. Gerbeau, J. Sainte-Marie, and I. E. Vignon-Clementel, "A poroelastic model valid in large strains with applications to perfusion in cardiac modeling," *Comput. Mech.*, vol. 46, pp. 91–101, 2010.

[116] K. May-Newman and A. D. McCulloch, "Homogenization modeling for the mechanics of perfused myocardium," *Prog. Biophys. Mol. Biol.*, vol. 69, no. 2-3, pp. 463–481, 1998.

[117] F. Concha, M. Sarabia-Vallejos, and D. E. Hurtado, "Micromechanical model of lung parenchyma hyperelasticity," *J. Mech. Phys. Solids*, vol. 112, pp. 126–144, 2018.

[118] S. C. Cowin, "Bone poroelasticity," *J. Biomech.*, vol. 32, no. 3, pp. 217–238, 1999.

[119] G. Gailani and S. Cowin, "Ramp loading in russian doll poroelasticity," *J. Mech. Phys. Solids*, vol. 59, no. 1, pp. 103–120, 2011.

[120] W. Ehlers and B. Markert, "A linear viscoelastic biphasic model for soft tissues based on the theory of porous media," *J. Biomech. Eng.*, vol. 123, no. 5, pp. 418–424, 2001.

[121] W. Ehlers, "Challenges of porous media models in geo-and biomechanical engineering including electro-chemically active polymers and gels," *Int. J. Adv. Eng. Sci. Appl. Math.*, vol. 1, pp. 1–24, 2009.

[122] J. Schröder, "A numerical two-scale homogenization scheme: The fe2-method," in *Plasticity and beyond: microstructures, crystal-plasticity and phase transitions*, Springer Vienna, 2014, pp. 1–64.

[123] R. Hill, "Elastic properties of reinforced solids: Some theoretical principles," *J. Mech. Phys. Solids*, vol. 11, no. 5, pp. 357–372, 1963.

[124] U. Hornung, *Homogenization and porous media*. Springer Science & Business Media, 2012, vol. 6.

[125] J. Fish, *Practical multiscaling*. John Wiley & Sons, 2013.

[126] C. Truesdell, *Historical Introit The origins of rational thermodynamics*. Springer, 1984.

[127] O. Coussy, *Poromechanics*. Wiley, 2004.

[128] W. Ehlers and J. Bluhm, *Porous media: theory, experiments and numerical applications*. Springer, 2002.

[129] R. De Boer, *Trends in continuum mechanics of porous media*. Springer, 2005.

[130] L. Berger, R. Bordas, K. Burrowes, V. Grau, S. Tavener, and D. Kay, "A poroelastic model coupled to a fluid network with applications in lung modelling," *Int. J. Numer. Methods Biomed. Eng.*, vol. 32, no. 1, e02731, 2016.

[131] D. Chapelle and P. Moireau, "General coupling of porous flows and hyperelastic formulations—from thermodynamics principles to energy balance and compatible time schemes," *Eur. J. Mech. B Fluids*, vol. 46, pp. 82–96, 2014.

[132] B. Markert, Y. Heider, and W. Ehlers, "Comparison of monolithic and splitting solution schemes for dynamic porous media problems," *Int. J. Numer. Methods Eng.*, vol. 82, no. 11, pp. 1341–1383, 2010.

[133] C. W. MacMinn, E. R. Dufresne, and J. S. Wettlaufer, "Large deformations of a soft porous material," *Phys. Rev. Appl.*, vol. 5, no. 4, p. 044 020, 2016.

[134] A. T. Vuong, L. Yoshihara, and W. Wall, "A general approach for modeling interacting flow through porous media under finite deformations," *Comput. Methods Appl. Mech. Eng.*, vol. 283, pp. 1240–1259, 2015.

[135] L. Dormieux, A. Molinari, and D. Kondo, "Micromechanical approach to the behavior of poroelastic materials," *J. Mech. Phys. Solids*, vol. 50, no. 10, pp. 2203–2231, 2002.

[136] E. B. Tadmor, R. E. Miller, and R. S. Elliott, *Continuum mechanics and thermodynamics: from fundamental concepts to governing equations*. Cambridge University Press, 2012.

[137] D. P. Bertsekas, "Nonlinear programming," *J. Oper. Res. Soc.*, vol. 48, no. 3, pp. 334–334, 1997.

[138] S. Boyd and L. Vandenberghe, *Convex optimization*. Cambridge university press, 2004.

[139] T. J. Hughes, *The finite element method: linear static and dynamic finite element analysis*. Courier Corporation, 2012.

[140] A. Logg, K. A. Mardal, and G. Wells, *Automated solution of differential equations by the finite element method: The FEniCS book*. Springer, 2012.

[141] I. Babuška, "Error-bounds for finite element method," *Numer. Math.*, vol. 16, pp. 322–333, 1971.

[142] F. Brezzi, "On the existence, uniqueness and approximation of saddle-point problems arising from lagrangian multipliers," *Publications mathématiques et informatique de Rennes*, no. S4, pp. 1–26, 1974.

[143] P. Bilic, P. Christ, H. B. Li, E. Vorontsov, A. Ben-Cohen, G. Kaissis, and B. Menze, "The liver tumor segmentation benchmark (lits)," *Med. Image Anal.*, vol. 84, p. 102 680, 2023.

[144] V. Rezania, D. Coombe, and J. Tuszynski, "Liver bioreactor design issues of fluid flow and zonation, fibrosis, and mechanics: A computational perspective," *J. Funct. Biomater.*, vol. 11, p. 13, 2020.

[145] K. K. Brock, M. B. Sharpe, L. A. Dawson, S. M. Kim, and D. A. Jaffray, "Accuracy of finite element model-based multi-organ deformable image registration," *Med. Phys.*, vol. 32, pp. 1647–1659, 2005.

[146] A. Formaggia L.and Quarteroni and A. Veneziani, *Cardiovascular Mathematics: Modeling and simulation of the circulatory system*. Springer Science & Business Media, 2010, vol. 1.

[147] J. M. Huyghe and D. H. Van Campen, "Finite deformation theory of hierarchically arranged porous solids—i. balance of mass and momentum," *Int. J. Eng. Sci.*, vol. 33, no. 13, pp. 1861–1871, 1995.

[148] J. M. Huyghe and D. H. Van Campen, "Finite deformation theory of hierarchically arranged porous solids—ii. constitutive behaviour," *Int. J. Eng. Sci.*, vol. 33, no. 13, pp. 1873–1886, 1995.

[149] W. J. Vankan, J. M. Huyghe, J. D. Janssen, A. Huson, W. J. G. Hacking, and W. Schreiner, "Finite element analysis of blood flow through biological tissue," *Int. J. Eng. Sci.*, vol. 35, no. 4, pp. 375–385, 1997.

[150] T. Ricken and J. Bluhm, "Remodeling and growth of living tissue: A multiphase theory," *Arch. Appl. Mech.*, vol. 80, pp. 453–465, 2010.

[151] J. Collis, D. L. Brown, M. E. Hubbard, and R. D. O'Dea, "Effective equations governing an active poroelastic medium," *Proc. R. Soc. A*, vol. 473, no. 2198, p. 20 160 755, 2017.

[152] R. Penta, D. Ambrosi, and R. Shipley, "Effective governing equations for poroelastic growing media," *QJMAM*, vol. 67, no. 1, pp. 69–91, 2014.

[153] W. Ehlers, B. Markert, and O. Röhrle, "Computational continuum biomechanics with application to swelling media and growth phenomena," *GAMM-Mitteilungen*, vol. 32, no. 2, pp. 135–156, 2009.

[154] R. Sacco, P. Causin, C. Lelli, and M. T. Raimondi, "A poroelastic mixture model of mechanobiological processes in biomass growth: Theory and application to tissue engineering," *Meccanica*, vol. 52, pp. 3273–3297, 2017.

[155] S. L. Xue, B. Li, X. Q. Feng, and H. Gao, "Biochemomechanical poroelastic theory of avascular tumor growth," *J. Mech. Phys. Solids*, vol. 94, pp. 409–432, 2016.

[156] D. Ambrosi, S. Pezzuto, D. Riccobelli, T. Stylianopoulos, and P. Ciarletta, "Solid tumors are poroelastic solids with a chemo-mechanical feedback on growth," *J. Elast.*, vol. 129, pp. 107–124, 2017.

[157] M. Fraldi and A. R. Carotenuto, "Cells competition in tumor growth poroelasticity," *J. Mech. Phys. Solids*, vol. 112, pp. 345–367, 2018.

[158] E. H. Lee, "Elastic-plastic deformation at finite strains," *J. Appl. Mech.*, vol. 36, no. 1, pp. 1–6, 1969.

[159] P. Wriggers and T. A. Laursen, *Computational contact mechanics*. Springer, 2006, vol. 2.

[160] G. Himpel, E. Kuhl, A. Menzel, and P. Steinmann, "Computational modelling of isotropic multiplicative growth," *Comp. Mod. Eng. Sci.*, vol. 8, pp. 119–134, 2005.

[161] A. Goriely, *The mathematics and mechanics of biological growth*. Springer, 2017.

[162] K. Tsomaia, L. Patarashvili, N. Karumidze, I. Bebiashvili, E. Azmaipharashvili, I. Modebadze, and D. Kordzaia, "Liver structural transformation after partial hepatectomy and repeated partial hepatectomy in rats: A renewed view on liver regeneration," *World J. Gastroenterol.*, vol. 26, no. 27, p. 3899, 2020.

[163] S. J. Forbes and P. N. Newsome, "Liver regeneration—mechanisms and models to clinical application," *Nat. Rev. Gastroenterol. Hepatol.*, vol. 13, no. 8, pp. 473–485, 2016.